Dissertation

submitted to the
Combined Faculties for the Natural Sciences and for Mathematics
of the Ruperto-Carola University of Heidelberg, Germany
for the degree of
Doctor of Natural Sciences

Put forward by

M. Sc.:   Andreas W. Rau
born in: Neustadt an der Weinstraße

Oral examination: April 22$^{\text{nd}}$, 2009

Real-time tumor localization with electromagnetic transponders for image-guided radiotherapy applications

Referees: Prof. Dr. Uwe Oelfke

Prof. Dr. Hartmut Dickhaus

Echtzeit-Tumorortung mittels elektromagnetischer Sonden für Anwendungen in der bildgeführten Strahlentherapie

— Zusammenfassung —

Die Detektion intrafraktioneller Organbewegung zur Vermeidung eventueller Fehlbestrahlungen ist ein ungelöstes Problem der Strahlentherapie. Ein neuartiges Konzept zur dynamischen Bewegungserfassung des Tumors verwendet in den Tumor implantierte elektromagnetische (EM) Sonden. In dieser Arbeit werden Konzepte und Strategien zur Anwendung dieser neuen Technologie in der bildgeführten Strahlentherapie (IGRT) entwickelt. Zunächst erfolgt die experimentelle Untersuchung der Kompatibilität der EM Technologie mit der strahlentherapeutischen Umgebung. Anschließend wird ein Verfahren zur Kombination der EM Tumorortung mit der Roentgenbildgebung in der IGRT entwickelt. Dieses Verfahren nutzt die spezifischen Vorteile der EM Tumorortung (nicht-ionisierende Strahlung, dreidimensionale Ortung) und die der Roentgenbildgebung (volumetrische Information über Organdeformation, -rotation, Position der Risikoorgane). Das Verfahren konnte erfolgreich zur Vermeidung von Bewegungsartefakten in Kegelstrahltomograhiebildern eingesetzt werden. Zusätzlich wird die Echtzeit-Steuerung eines dynamischen Lamellenkollimators auf der Grundlage der EM Sonden grundsätzlich realisiert. Zum Abschluss der Arbeit wird die klinische Einführung der EM Tumorortung im Rahmen einer Prostatastudie erreicht. Die entwickelten Konzepte verbessern die Detektion intrafraktioneller Organbewegung in der IGRT und ermöglichen dadurch die genauere Bestrahlung dynamischer Zielvolumina.

Real-time tumor localization with electromagnetic transponders for image-guided radiotherapy applications

— Abstract —

The detection of intrafraction organ motion, necessary for the minimization of treatment errors, is a remaining challenge in radiotherapy. A novel technology for the dynamic monitoring of tumor motion uses tumor-implanted electromagnetic (EM) transponders. In the present thesis, concepts and strategies for the use of the EM technology in image-guided radiotherapy (IGRT) are developed. First, the compatibility of the EM technology with the radiotherapy environment is investigated experimentally. Subsequently, a technique is developed that combines EM tumor localization with the x-ray imaging options of IGRT. This technique exploits the unique advantages of EM tumor localization (non-ionization radiation, three-dimensional target localization) and those of x-ray imaging (volumetric information about organ deformation and rotation, localization of organs at risk). The technique has been applied successfully to the elimination of motion artifacts in cone-beam computed tomography. In addition, the real-time control of a dynamic multi-leaf collimator based on the EM transponders could be demonstrated. Finally, the EM tumor tracking technology is introduced clinically with a study on prostate motion. The concepts developed in this thesis improve the detection of intrafraction organ motion in IGRT and thus enable the treatment of dynamic target volumes with increased accuracy.

Contents

Contents

Abbreviations, acronyms and definitions

AC . . . . Alternating current
AP . . . . Anterior-posterior
BB . . . . Ball bearing
CBCT . . . . Cone-beam computed tomography
CC . . . . Cranial-caudal
CRF . . . . Coordinate reference frame
DIMDI . . . . Deutsches Institut für Medizinische Dokumentation und Information
DKFZ . . . . Deutsches Krebsforschungszentrum in Heidelberg/Germany
DMLC . . . . Dynamic multi-leaf collimator
EM . . . . Electromagnetic
FPI . . . . Flat panel imager
fps . . . . Frames per second
HU . . . . Hounsfield number
IEC . . . . International Electrotechnical Commission
IGRT . . . . Image-guided radiotherapy
IMRT . . . . Intensity-modulated radiation therapy
IR . . . . Infrared
kV . . . . Kilo-voltage
Linac . . . . Linear accelerator
LR . . . . Left-right
MIF . . . . Metal-in-field
MLC . . . . Multi-leaf collimator
MRI . . . . Magnetic resonance imaging
MV . . . . Mega-voltage
QA . . . . Quality assurance
RMS . . . . Root-mean-square
ROI . . . . Region of interest
RT . . . . Radiotherapy
TPS . . . . Treatment planning system
TTA . . . . Transponder-tracking image processing algorithm
UDP . . . . User datagram protocol

USA . . . . United States of America

Voxel . . . . Volume element

3D . . . . Three-dimensional

2D . . . . Two-dimensional

Chapter 1

Introduction

1.1 Radiotherapy and target motion

The general goals of radiotherapy are (1) the delivery of high, conformal doses to cancerous tissues while at the same time (2) sparing healthy tissue from receiving radiation dose. In external photon beam radiotherapy, these two goals usually constitute a trade-off because the high energy photon beams (x rays) always strike both cancerous and healthy tissues along their path through the patient. Clearly, one prerequisite for achieving these goals is the ability to deliver highly conformal dose distributions to arbitrarily shaped cancerous tissues, i. e. to the target volumes of radiotherapy. The invention (in the 1990s) and the clinical availability of intensity modulated radiotherapy (IMRT) planning and delivery systems (in the past decade) has greatly increased our ability to deliver such conformal dose distributions to immobile target volumes. However, any motion of the patient anatomy relative to the external x-ray beams leads to a misalignment of the conformal dose distribution with the actual tumor target, which underdoses tumor areas and can thus compromise clinical outcomes. One practical solution for handling the uncertainties introduced by motion is to increase the spatial extent of possibly perfectly conformal dose distributions by some population-averaged safety margin such that high-dose coverage of the tumor can be guaranteed [1]. The downside of this strategy is that more healthy tissue will be irradiated and thus the likelihood of treatment-related toxicity will increase. Hence, we want the safety margins to be as tight as possible. To achieve the necessary treatment accuracy, patient-specific anatomical motion must be measured as it occurs and managed in a motion-adaptive treatment scheme. Ultimately, this should lead to a better realization of the goals of radiotherapy.

Two types of anatomical motion are usually distinguished mostly based on the time periods in which they occur:

Interfraction anatomical motion Interfraction motion refers to the differences in anatomy and patient position encountered from treatment fraction to treatment fraction in fractionated radiotherapy. Interfraction motion and deformation occur because of

tumor shrinkage or growth, translations and rotations of the target within the skeletal anatomy, daily bowel and bladder filling differences, and weight loss or gain because of either the radiation itself or concurrent therapies. It also includes daily setup variability (which, strictly speaking, is not a type of anatomical motion). Interfraction motion occurs on timescales of several hours to days.

Intrafraction anatomical motion Intrafraction motion refers to the changes in anatomy and patient position encountered moment-to-moment during a treatment fraction. Intrafraction anatomical motion and deformation occur because of the respiratory, gastro-intestinal and cardiac systems or because of whole-patient movements. Intrafraction motion occurs on timescales shorter than or equal to the duration of the actual dose delivery, i. e. ten minutes to half an hour.

While interfraction motion may be managed by the recently developed methods of image-guided radiotherapy (IGRT) [2–5], the individualized management of intrafraction motion is a more difficult task. This is partly because intrafraction (as well as interfraction) motion is to some extent unpredictable, thus defying the use of prediction models, but needs to be measured instead. The unpredictability of intrafraction organ motion has been shown for the prostate [6] and for lung tumors as well [7, 8]; the latter in the form of intrafraction variability and baseline shifts of lung tumor trajectories.

The management of intrafraction motion is necessary to mitigate its detrimental impact on imaging procedures and on the dose distributions [9, 10]. What is needed for the proper management of intrafraction motion? (1) An estimation of the expected (periodic component of) intrafraction motion obtained either through patient population models or through a prior measurement of the motion in the patient; (2) treatment planning methods that can incorporate intrafraction motion [11–13]; (3) technology and methods to measure motion during the treatment, i. e. truly intrafraction and (4) technology and methods to adapt the treatment to the measured intrafraction motion either on an inter- or an intrafraction basis. This thesis is concerned with the development and the evaluation of methods for the measurement of intrafraction motion. These methods should be based on the combination of target volume tracking using electromagnetic (EM) transponders with the in-room x-ray imaging options of modern radiotherapy machines (high-energy x-ray producing linear electron accelerators or *Linacs,* for short).

With the advent of Linac-mounted (so called *onboard*) diagnostic x-ray imaging over the past decade, it would in principle be possible to image the patient (fluoroscopically) at any instant of his/her treatment. However, continuous x-ray imaging does not constitute an ideal motion measurement strategy: (1) the x-ray images require more or less time-intensive post-processing to interpret their information content, (2) only two out of three dimensions of the motion can readily be resolved and (3) large-area, non-conformal

imaging dose accumulates in and stresses healthy tissues. Motion tracking technology based on electromagnetic principles overcomes these three disadvantages and thus lends itself to complement image-based methods.

Three EM motion tracking concepts have reached a level of development that allowed first tests in the radiotherapy environment. First, the TULOC (short for "tumor localization") system was developed at the Paul Scherrer Institut in Switzerland [14]. This system uses a field generator consisting of six differential coils that form the edges of a tetrahedron-shaped assembly. Miniature field sensors would be implanted into the patient with a wire attached to them that connects to an ex-vivo signal processing unit. This same concept was commercialized as the Aurora system (Northern Digital Inc., Waterloo, Ontario, Canada). However, it has now developed into a system for radiological interventions and moved away from its initial design idea as a tool for radiotherapy. A different concept is being pursued by Micropos Medical AB, Goeteborg, Sweden. Their product, called RayPilot, uses an antenna that is placed on top of the treatment tabletop, i.e. underneath the patient [15]. The system's field sensor is temporarily introduced in the prostate via the patient's urethra. The sensor is wired as well, i.e. it connects to a processing unit outside the patient. Arguably the most advanced EM target tracking is the Calypso® 4D Localization System by Calypso Medical Technologies, Seattle, WA, USA. Their system uses three wireless transponders that are permanently implanted into the patient and can be localized using an antenna temporarily positioned near the patient (details follow in Section 2.1). In principle, EM target tracking provides the three-dimensional position of the target volume objectively, continuously and without the use of ionizing radiation.

1.2 Thesis objectives

The objectives of this thesis were, first, the evaluation of the compatibility of the Calypso System with the radiotherapy workplace at the German Cancer Research Center (DKFZ), Heidelberg. This radiotherapy workplace is based on the Siemens ARTISTE platform (details in Section 2.2). If compatibility can be established, this work should lead to the clinical introduction of the Calypso System in Europe and, on the worldwide scale, in conjunction with the ARTISTE platform.

Second, the design and the implementation of novel methods for intrafraction motion measurement in IGRT should be realized. These methods should explore the synergistic combination of the onboard imaging options of the Linac with EM-based target tracking. The feasibility and applications of such methods should be demonstrated.

1.3 Thesis organization

Chapter 2 of this thesis introduces the investigations of the compatibility of the EM target tracking system with the radiotherapy equipment including reviews of the EM tracking system, the radiotherapy equipment and other experimental hardware. The continuation of Chapter 2 is, in a way, the introduction of EM tracking into the clinic, which is the subject of Chapter 5. The chapters are presented in chronological order of the performed investigations; the clinical study is ongoing work and is thus listed last. Chapter 3 presents the integration of the EM tracking system with the imaging capabilities of the radiotherapy platform. This chapter ends with the demonstration of concurrent target tracking using EM-based technology and onboard x-ray imaging. The developments of Chapter 3 could be translated into an immediate application: four-dimensional cone-beam computed tomography. The description and the realization of this application is given in Chapter 4. Chapter 6 puts the developments of this thesis in the context of other works in the field, suggests clinical use cases and future works at DKFZ. Finally, Chapter 7 summarizes the thesis.

Chapters 2 through 4 should be self-contained meaning that they can be read independently. They feature brief motivations at the beginnings and short summaries at the ends of each chapter. Chapter 2 contains many of the basic systems descriptions and experimental findings that reach into later chapters. Hence, this chapter may serve as a reference to the other chapters. An attempt was made to make the contents clear also for non-experts in radiotherapy.

The research for this dissertation was conducted in the Department of Medical Physics in Radiation Oncology at the DKFZ in Heidelberg over a period of three and a half years. Portions of this work have been presented at national and international conferences, either orally [16, 17] or as a poster [18], and published in a peer-reviewed journal [19].

Chapter 2

Systems integration

2.1 The Calypso System

This section describes the Calypso® 4D Localization System™ (Calypso Medical Technologies, Seattle, WA, USA)—the electromagnetic (EM) tracking system investigated in this work. The Calypso System was chosen for investigation because it uniquely provides objective measurements of target positions using non-ionizing radiation which promises to complement x-ray based imaging in the management of organ motion.

2.1.1 Components

The Calypso System comprises two main components: the Beacon transponders and the console with the magnetic array. The Beacon transponders are permanently implantable devices (see Figure 2.1). Essentially, they are passive miniature RLC resonant circuits
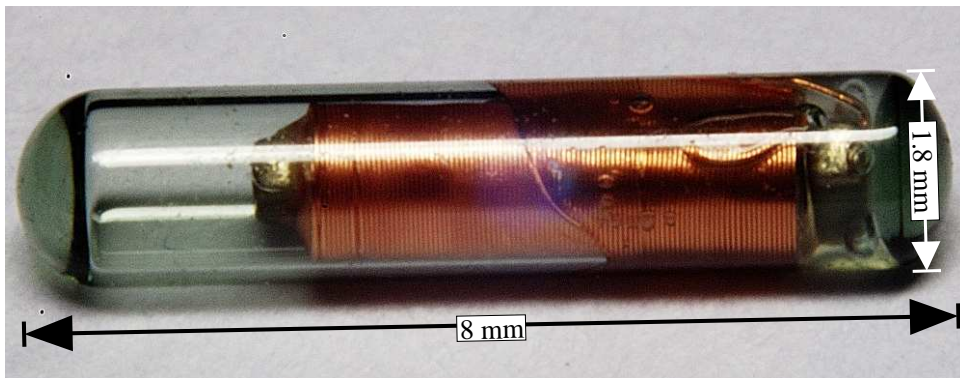

Figure 2.1: *Implantable Beacon® transponder of the Calypso System. A passive RLC resonant circuit is embedded in a bio-compatible glass capsule. The inductor (coil of copper wire wound around ferrite core) can be seen; the capacitor is at the right end of the coil. The inherent wire resistance serves as the resistor of the circuit.*

encapsulated in a bio-compatible glass capsule. Their size is comparable to that of grains

of rice (diameter 1.8 mm, length 8 mm). Typically, a physician implants three Beacon transponders into the patient's body, usually directly into the treatment target or in close proximity to the target. At the time of writing, the prostate and the prostatic bed (post-prostectomy) are implantation sites cleared by the American Food And Drug Administration. Due to their miniature dimensions, the implantation procedure is similar to standard seed placement or biopsy procedures in the prostate. The Beacon transponders operate without physical connection to the outside of the patient, i. e., the electromagnetic system operates wirelessly.

Figure 2.2: *Calypso console. (Image source: Calypso Medical)*

The console (Figure 2.2) is a mobile module that incorporates the following components: a power and control unit placed in the base of the module, a console PC with a touch-screen user interface mounted on the support pole of the module, and an arm mounted on the pole with the electromagnetic detector array (for short: magnetic array) mounted on its distal end. For clinical use, the console resides at the side of the treatment table and the magnetic array is positioned directly above the patient. The magnetic array acts as an antenna localizing the implanted Beacon transponders inside the patient. The localization volume covered by the array is a $14 \times 14 \, \text{cm}^2$ field of view in a plane parallel to the magnetic array and up to 27 cm in water-equivalent depth. When the Beacon transponders are inside the localization volume, the system locates immobile targets with submillimeter accuracy [20]. Apart from its main components, the Calypso System consists of an optical subsystem, a network hub and a tracking station.

Figure 2.3: *Overview over the arrangement of the Calypso System components in the treatment room and in the control room (Tracking Station). Three transponders are implanted in the patient. These are localized by the magnetic array. The array is localized by cameras such that the transponder coordinates are reported in the room coordinate system. (Image source: Calypso Medical Technologies)*
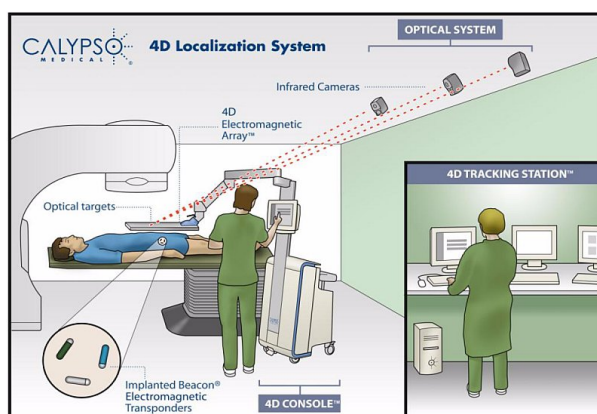

These components can be seen in Figure 2.3.

2.1.2 Technology

The optical and the electromagnetic subsystem form the technological core of the Calypso System. During calibration, the coordinate systems of the two subsystems are registered together. The optical subsystem uses three infrared (IR) sensitive cameras mounted on the ceiling of the treatment room to localize and track as many as possible of nine active IR markers located on the top surface of the magnetic array (see Figure 2.4a). This subsystem determines the position of the magnetic array in the Linac frame of reference.

The electromagnetic subsystem, i.e. the magnetic array and the Beacon transponders, determines the target position in the reference frame of the magnetic array. This system uses a sophisticated call-and-response communication relay between the Beacon transponders and the magnetic array (see Figure 2.4b). Typically, three Beacon transponders are implanted into the patient, each tuned to a distinct resonant frequency in the range from 200 kHz to 600 kHz. The magnetic array produces alternating-currents (AC) magnetic fields (*B-fields*) at the resonant frequencies of the Beacon transponders and at optimal spatial orientations. Optimal B-field orientations are determined iteratively prior to each tracking session. B-field orientations are considered optimal if they maximize the electromagnetic coupling efficiency between the magnetic array and the transponders, which, in turn, will depend on the spatial orientations of the transponders. The B-fields sequentially transfer energy to the circuitry of the transponders, which causes them to resonate.
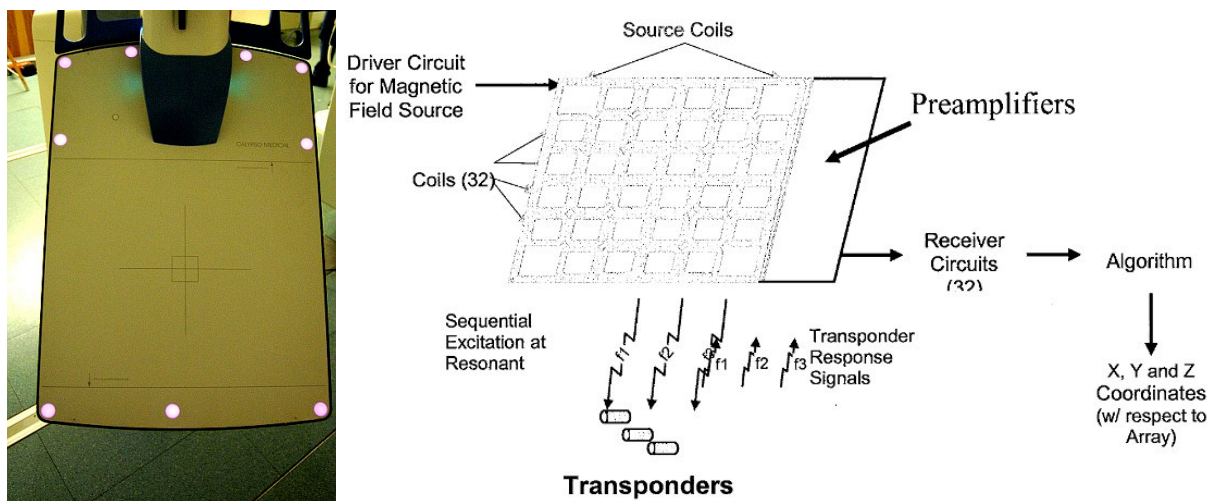
(a) Magnetic array with IR lights   **(b)** Electromagnetic subsystem (Image source: Balter et al. [20])

Figure 2.4: *(a) Top-view photograph of the magnetic array showing the shining IR lights (invisible to the human eye). (b) Process of transponder localization by the EM subsystem. Four source coils (not explicitly shown) excite the transponders and 32 receive coils pick up the response signal coming from the transponders.*

Following the excitation of a transponder, the magnetic array switches to receive mode (i. e. active B-field emission ceases) and 32 receiving coils measure the resonance signal from one Beacon transponder at a time. This measurement results in the calculation of the three-dimensional (3D) position of the Beacon transponder relative to the magnetic array. The array of receive-coils, the array-transponder communication and other components of the EM subsystem are roughly sketched in Figure 2.4b.

The process of transponder excitation, response measurement and calculation of position is accomplished in 100 ms per transponder (on average). Each update of the position of the transponders leads to an update of the target position. The tracking target is defined as the centroid of the triangle established by the locations of the three Beacon transponders in space (a set of three weighting factors applies but these are internal to the system). Based on the target update rate of 10 Hz, the Calypso System provides near real-time 4D target localization.

2.1.3 Installations at DKFZ

In the course of this work, two Calypso System installations were planned and completed. The first installation was carried out in June of 2006 at the research-dedicated Linac at the DKFZ. It was based on a research collaboration between Calypso Medical and DKFZ to investigate the compatibility of the Calypso System and the Siemens ARTISTS Linac, to investigate lung tumor tracking with phantoms and to perform preparations for a clinical prostate trial.

The second installation was carried out in September of 2008 at the clinical Linac at the DKFZ, which, in addition to the Linac, features a Primatom CT-on-Rails (Siemens Medical, Erlangen, Germany) in the treatment room. A follow-up research collaboration was agreed upon. The purpose of this second installation was the execution of the clinical trial that was planned in the first phase of the collaboration. The kick-off for the clinical trial occurred in February of 2009; the trial is currently underway. The expected duration of this trial from the first fraction of the first patient to the last fraction of the last patient is projected to be approximately one year.

2.2 The ARTISTE radiotherapy suite

The Siemens ARTISTE[TM] solution is the latest product in the line of Siemens radiotherapy suites. This description will focus on the imaging hardware components of the ARTISTE solution as these were most relevant to the present work[1]. The hardware inno-

---

[1]Please refer to the manufacturer's site (e. g. https://www.smed.com/artiste/) for a more complete system overview.

vations of the ARTISTE solution include components that enable IGRT and a multileaf collimator (MLC) with narrower and an increased number of leaves (160) that improves the tumor conformality of the radiation fields. A concise list of tradenames and the technologies involved are provided below.

160 MLC™ A multileaf collimator with 160 leaves, each with a projected width at the isocenter of 5 mm. Radiation fields of a maximum area of $40 \times 40 \,\mathrm{cm}^2$ can be shaped. The maximum leaf velocity is 4 cm/s. A detailed description and evaluation of the MLC was performed by Tacke et al. [21].
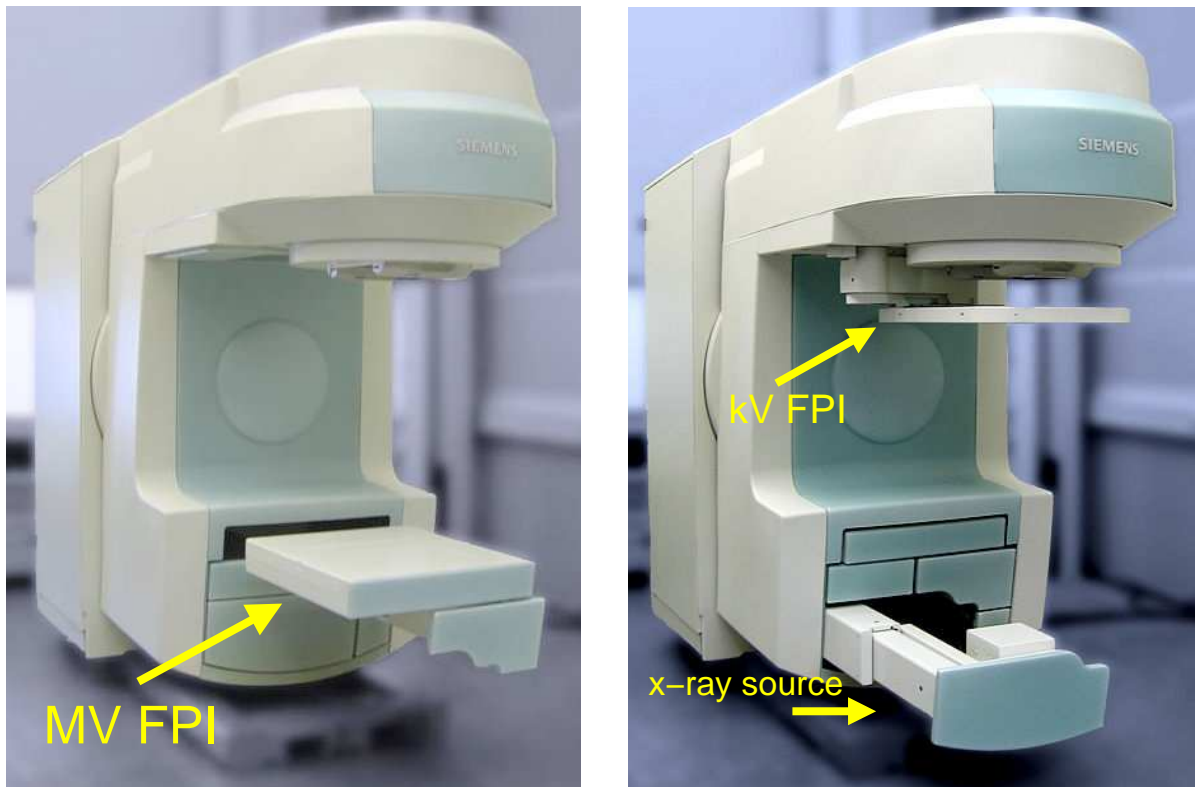
(a) FPI used for MV x-ray imaging deployed

(b) kV x-ray source and FPI deployed

Figure 2.5: *Linear accelerator of the Siemens ARTISTE solution. In (a), the components for MV x-ray imaging are shown in the deployed position; in (b), the kV components are deployed.*

MVision™ and OPTIVUE™ These represent the megavoltage imaging options of the ARTISTE Linac. In both cases, the x-ray imaging beam originates from the same source as the treatment beam, i. e. from the electron target in the Linac head. The image receptor for both imaging modes is an amorphous silicon flat-panel imager (FPI) shown in Figure 2.5a. The sensitive area of the FPI is $41 \times 41 \,\mathrm{cm}^2$ featuring an array of 1024×1024 pixels with a pitch of 0.4 mm (for details see e. g. Morin

et al. [22]). MVision provides MV cone-beam computed tomography (explained in some more detail below in Section 2.2.1), whereas OPTIVUE provides two-dimensional (2D) portal imaging. Portal imaging is 2D projection radiography using the treatment beam for imaging. Portal imaging can be performed during patient setup using open fields (i. e. illuminating the entire sensitive area of the FPI) or during the treatment using the collimated treatment field. The latter is referred to as *portals-during* and an example is shown in Figure 3.10.

kVision™ kVision denotes the kilovoltage x-ray imaging options of the ARTISTE solution. The kVision system is an implementation of the inline kV x-ray imaging concept [23, 24]. In this concept, the kV x-ray source is offset 180° from the MV x-ray source. A retractable FPI is positioned in front of the gantry head (approx. 60 cm away from the MV x-ray source along the central beam axis), and the kV x-ray source is located 200 cm away from the MV x-ray source along the central beam axis. The FPI used in the kVision system is optimized for reception of kV x rays but has otherwise the same pixel resolution and sensitive area as the FPI used in MVision. Its fastest read-out time is 66 ms, i. e. it is able to acquire ~15 frames per second. The nominal tube voltage is 150 kVp. The kVision system can be used both for fluoroscopy imaging, i. e. x-ray video imaging of patient anatomy, and for kV CBCT.

CTVision™ CTVision is a diagnostic kV CT scanner that travels on two parallel rails in the treatment room (also called CT-on-rails). At DKFZ, the system is a SOMATOM® single slice, spiral CT scanner. In order to image a patient using the CT scanner, the treatment table is rotated by 90° around the z-axis and the CT-on-rails is moved so that the patient is positioned inside the ring-structure of the CT gantry.

2.2.1 Cone-beam computed tomography (CBCT)

At this point, a brief introduction to CBCT shall be presented so that the imaging investigations in Chapters 3 and 4 may be comprehended. Chapter 4 deals with the realization of an advanced CBCT data acquisition technique.

A CBCT dataset is a stack of images that is reconstructed from a set of open-field projection images acquired at different positions around the patient. The process is similar to conventional CT acquisition, where the transmission of a narrow x-ray fan beam is measured by a row of detectors and mathematically reconstructed to yield transversal image slices. For conventional CT, the 3D dataset is formed by translating the patient and thus imaging the patient slice by slice. For CBCT, a 2D detector array (the FPI)

is used and a 3D image dataset is reconstructed directly without the need for multiple gantry rotations or table movement. For MV CBCT, projection images are acquired using the photon treatment beam of a medical Linac with beam energies primarily in the megaelectron volt range; for kV CBCT, projection images are acquired using diagnostic x-ray beams primarily in the kiloelectron volt range. Compared to diagnostic fan-beam CT, Linac-mounted CBCT has the advantages that images of the patient in treatment position can be readily acquired and that, owing to the wide-beam geometry, it makes more efficient use of the produced x-rays. Disadvantages are unfavorable scatter conditions and slower data acquisition, which makes CBCT more prone to motion artifacts.

Another aspect of (CB)CT, the Hounsfield numbers, will be explicated because these will be referred to later. For in-depth treatises on the theoretical and practical aspects of CBCT image formation, please refer to works such as Feldkamp et al. [25], Jaffray et al. [26] or Oelfke et al. [5]. Hounsfield numbers, generally abbreviated as HU for *Hounsfield unit*, are an x-ray beam-quality-independent representation of voxel intensity. The reconstructed voxel intensities in CT images represent line integrals of x-ray attenuation coefficients $\mu\left(\mathbf{r}\right)$ along the projected rays. Attenuation coefficients depend on the energy of the x rays. To allow comparison between CT datasets from different (CB)CT scanners, the Hounsfield numbers, H, are calculated from the measured attenuation coefficients as

$$H_{object} := \frac{\mu_{object} - \mu_{water}}{\mu_{water}} \cdot 1000. \tag{2.1}$$

By definition (Equation 2.1), the Hounsfield number of water is $H_{water} = 0$ and the Hounsfield number of vacuum or air is -1000. Most soft tissues in the human body have HUs ranging from -100 to $+100$. Bone can have HUs of > 1000.

2.2.2 Tabletops

The tabletops used to position the patients at the Linac become a relevant component in the modern radiotherapy environment. The chosen tabletop needs to be compatible with treatment delivery, imaging procedures and EM target tracking. Compatibility with treatment delivery refers to the dose impact resulting from irradiating the patient through the structures of the tabletop. Compatibility with imaging concerns image artifacts introduced by the tabletop and geometric clearance with imaging equipment (onboard CBCT components, Primatom CT scanner). Compatibility with EM tracking deals with electrically conductive structures of the tabletop that could interfere with EM target localization. These compatibilities were investigated (to different degrees) for the three tabletop models given in Table 2.1 that are suitable for the Siemens 550 TxT tablebase used with the ARTISTE solution. The TT-D and the TT-M tabletops are distributed through Siemens Oncology Care Systems (Erlangen, Germany); the former is specifically

Table 2.1: *Tabletops tested concerning their compatibility with treatment, imaging and EM target tracking. Thickness refers to the maximum thickness in z-direction (vertical).*

	TT-D	TT-M, Overlay	Qfix kVue
Width (cm)	50	53	min. 53
Thickness (cm)	4.5	19	12.5
Composition	Foam-filled carbon fiber shell	Carbon fiber frame, Kevlar overlay, metallic junction	Carbon fiber enforced beams, Kevlar or carbon fiber plates
Imaging	Optimized for x-ray imaging along the entire length	Not specifically optimized for x-ray imaging	Optimized for x-ray imaging through "stealth" beam design
EM compatibility	Not optimized for use with EM tracking system	Kevlar overlay to achieve compatibility	Optimized version with Kevlar cantilevers and inserts

optimized for diagnostic x-ray imaging procedures and thus was established as the routine tabletop at DKFZ in recent years. The Kevlar overlay for the TT-M tabletop is from Calypso Medical Technologies (Seattle, WA, USA). Two out of three components of the overlay are visible in the picture in Table 2.1: the headpiece towards the right of the image and the blue insert, which is where the target (the patient's prostate) would be positioned. The kVue tabletop is manufactured by WFR Aquaplast/Q-Fix Systems (Wyckoff, NJ, USA). A version optimized for EM target tracking exists that replaces the carbon fiber materials with Kevlar in as many components as possible.

2.2.3 Coordinate reference frames

This section introduces the coordinate reference frames (CRF) and the rotational axes that will be used later in this work. A typical Linac-based treatment environment has three characteristic axes of rotation. These are illustrated in Figure 2.6a. The table's
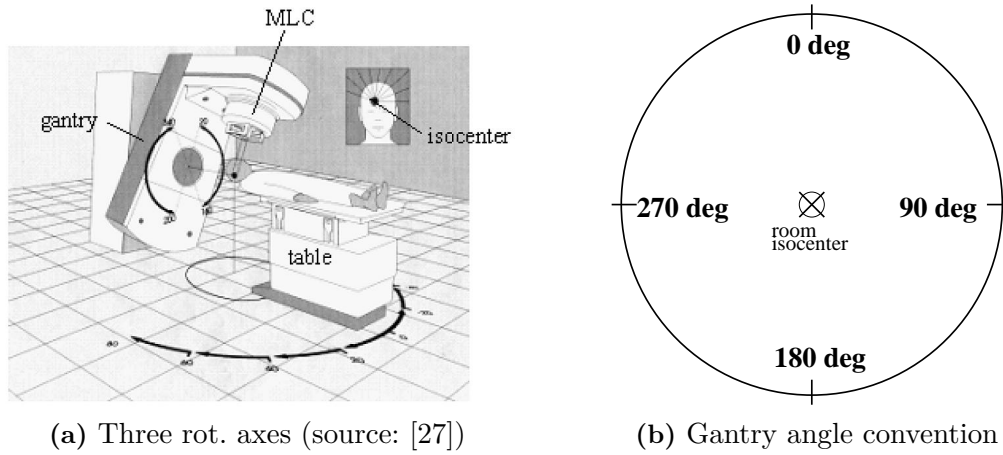
(a) Three rot. axes (source: [27])

(b) Gantry angle convention

Figure 2.6: *The three rotational axes encountered in the treatment room (a): table rotation, gantry rotation, MLC rotation. The convention for gantry angles is shown in (b).*

axis of rotation is normal to the room floor; the gantry rotates around the long axis of the treatment table; the MLC's is normal to the gantry rotation axis (and as such it rotates during gantry rotation in a transversal plane). All three axes of rotation intercept a point called the *room isocenter*. In turn, the *treatment isocenter* is an oncologist-defined point in the patient—usually somewhat centrally located in the target volume (an example of a treatment isocenter is shown in the isocenter-labeled picture insert of Figure 2.6a). For treatment delivery, the patient is usually positioned such that the treatment isocenter lines up with the room isocenter. The most relevant axis of rotation in the present work is the one of the gantry. Figure 2.6b shows the convention concerning gantry angles in a front view that applies to all Siemens Linacs. Using this convention, the gantry in Figure 2.6a would be approximately at the 20° position.

A couple of CRFs are typically encountered in the radiotherapy workflow. Figure 2.7 illustrates three of them relative to a patient in *treatment position*. The treatment position referred to throughout this work is defined as a patient lying on the back on the treatment table (*supine*, as in Figures 2.6a and 2.7) with the head pointing towards the Linac gantry (Figure 2.6a). The arrows denoting CRF axes in Figure 2.7, point in the positive coordinate direction. The patient CRF is defined with the x-axis in the patient's right-to-left direction, the y-axis in the patient's anterior-posterior direction and the z-axis in the patient's inferior-superior direction. The origin of the patient CRF can vary and naturally, the spatial orientation of the axes "move" with the patient. The stereotactic CRF is defined by the stereotactic tools used [28]. At DKFZ, the axes orientations are as indicated in Figure 2.7 and these are fixed with respect to the treatment table. The origin of the stereotactic CRF is centered relative to the table in x-direction, depends

13

Figure 2.7: *Three different CRFs encountered in radiotherapy. The picture assumes a patient in supine treatment position. The patient CRF is relative to the patient; the IEC CRF is relative to the treatment room and originates in the room isocenter; the stereotactic CRF typically has its axes parallel to the IEC's (albeit pointing in different directions).*
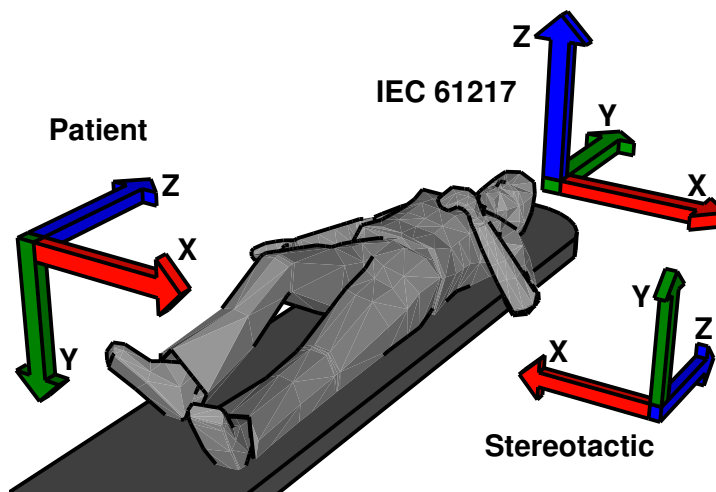
on the stereotactic tools in z-direction and is determined on a patient-to-patient basis in y-direction.

The Linac and the Calypso System adhere to the same room coordinate system defined according to the IEC 61217 standard. The origin of the IEC CRF is the room isocenter. In the present work, the IEC CRF is the most relevant and all coordinates are given in this CRF, unless otherwise noted.

2.3 Phantoms

The three most important phantoms used in this work will be described. All phantoms have transponders embedded in them, either in stable or variable configurations. The phantoms were used to simulate patients for both the EM tracking system and for the imaging systems.

2.3.1 Calypso body phantom

The Calypso body phantom shown in Figure 2.8 was manufactured by Calypso Medical Technologies. This phantom mimics the radiographic properties of a human pelvis by virtue of the phantom's oval shape and water-equivalent material composition. Three ~ 7.5 cm thick oval slabs of water-equivalent material are held together by a plastic clamp construction (as shown in Figure 2.8). The major axis of the oval transversal cross-section of the phantom is 35 cm long; the minor axis is 26 cm. The Calypso body phantom was used to evaluate transponder visibility in the MV x-ray images produced by the ARTISTE radiotherapy suite and to test the stability of the Calypso-reported target position under various influences such as gantry rotation.
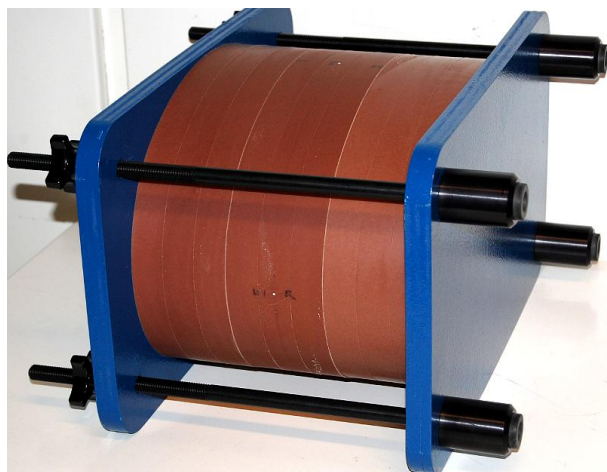
Figure 2.8: *Body-phantom consisting of three ~7.5 cm thick oval slabs of water-equivalent material. The center slab has a plexiglass insert that holds three Calypso transponders and a steel sphere at defined positions.*

2.3.2 Target phantom

The target phantom was developed in the course of this work for the fast generation of different targets for the Calypso System. A target for the Calypso System is an arrangement of three transponders in space. Hence, the target phantom provides flexible transponder positioning. The phantom consists of a Lucite block with a set of 12 drilled holes and an additional 16 holes drilled in an orthogonal direction, all of 1 cm diameter but irregularly spaced (see Figure 2.9). To hold the transponders in place, three solid-
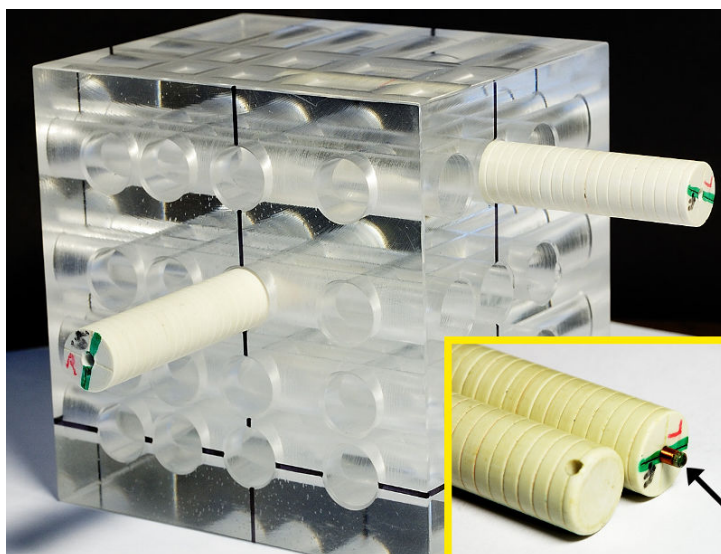

Figure 2.9: *Target phantom consisting of a Lucite block with orthogonal drillings in which transponders can be positioned using slidable rods. The inset (yellow box) shows the two ends of the rods that can hold transponders in two orientations. The arrow in the inset points to a transponder.*

water rods, approximately 10 cm in length, were manufactured that slid snugly in the holes and can hold transponders at each end. The inset of Figure 2.9 shows the ends of

the rods. At one end, the transponders are held with their long axis aligned with the rod's long axis. At the other end of the rod, the transponders are held with their long axis orthogonal to the rod's long axis. Using the target phantom, many different transponder arrangements can be realized.

2.3.3 Thorax phantom

To simulate breathing motion of lung tumors, a dynamic, anthropomorphic thorax phantom developed by Dietrich [29] was used. The thorax phantom (Figure 2.10) consisted of a stack of 12 transversal 1 cm thick slices that simulated the radiological properties of the human chest. Figure 2.10b displays one slice of the phantom, in which solid water (white) is used to simulate muscle tissue and lung tissue is simulated by a polyurethane-based foam (red). The shape of the lung tissue-equivalent area varied from slice to slice to approximate the 3D morphology of the lobes of the lung. An egg-shaped tumor consisting of solid water was embedded in one of the lobes of the lung. Three Beacon transponders were implanted into the tumor inlay of the phantom serving as reference points both for the Calypso System and for x-ray imaging (Figure 2.10c). The stack of torso slices was
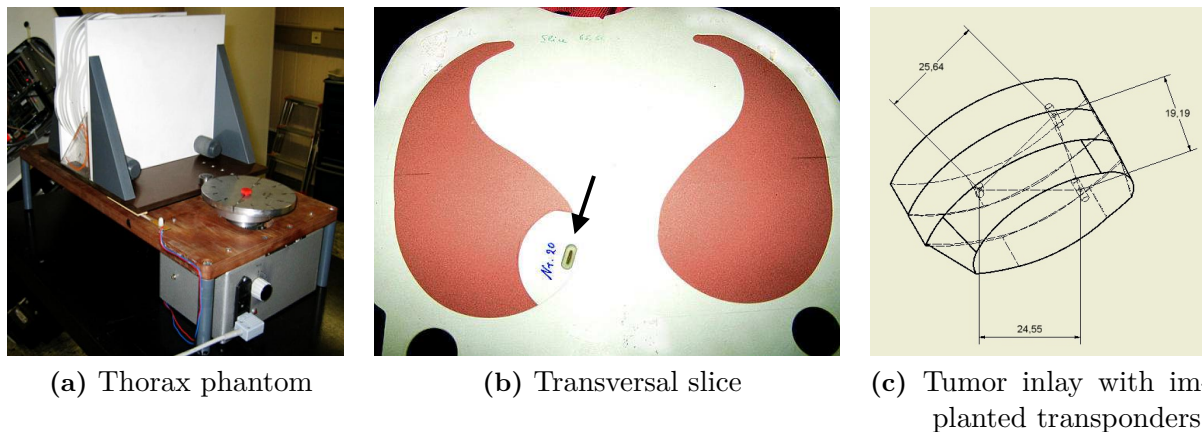

| (a) Thorax phantom | (b) Transversal slice | (c) Tumor inlay with implanted transponders |

Figure 2.10: *Thorax phantom, programmable to simulate breathing motion in cranio-caudal direction. The phantom has a tumor inlay into which three transponders were implanted. The arrow in (b) points to a slice of the tumor inlay showing one implanted transponder.*

mounted on a carriage that could be programmed to perform a wide range of periodic breathing motion in cranio-caudal (CC) direction, which was identified as the principal direction of breathing motion [30].

A reference measurement of the phantom's position is obtained from a sliding potentiometer attached to the carriage of the phantom. The readings from the potentiometer (sampling freq.: ~400 Hz, bitdepth: 12-bit) exhibit a linear voltage-to-displacement rela-

tionship in the range of experimental phantom positions. Calibration of the potentiometer before each experiment yielded conversion factors on the order of $1\,\mathrm{V/cm}$. The signal from the potentiometer was taken as the ground truth in the dynamic target tracking experiments.

2.4 Investigations of system compatibility

In this section, the investigations concerning general compatibility between the Calypso System and the ARTISTE radiotherapy suite are presented. To the best of my knowledge, these tests constitute the first time that the two systems had been used in conjunction. Compatibility was evaluated in terms of geometric clearance, effects of gantry rotation on EM target tracking, table compatibility, treating through the magnetic array and feasibility of driving the 160 MLC dynamically and in real-time using the Calypso System. Compatibility of EM tracking with onboard x-ray imaging is treated in a separate chapter (Chapter 3).

2.4.1 Geometric integration

The geometric clearance of the hardware components and the effect of the ARTISTE components on the performance of the EM target localization were evaluated because no prior experience on these issues existed.

2.4.1.1 Clearance

The components of Calypso System are designed to provide sufficient clearance for rotation of the Linac gantry. However, clearance with the new Linac-mounted imaging components of the ARTISTE Linac remains to be tested. Although the manufacturer explicitly discourages the operation of the Calypso System when any of the imaging components are deployed, geometric clearance of the components is desirable for workflow reasons and research interests. In clinical use, imaging and EM tracking can be used sequentially controlled from the control room without a therapist having to enter the treatment room. In terms of research interest, the combination of EM target tracking with concurrent imaging is an essential concept of the present work.

Geometric clearance was tested with the ARTISTE kV imaging components deployed. This situation is the most critical in terms of clearance because the radial distance of the kV FPI from the isocenter can be less than $40\,\mathrm{cm}$, i.e. less than the other Linac-mounted components. Figure 2.11 shows a cross-sectional view of the arrangement of the components drawn to scale. As the figure illustrates, clearance of the components could
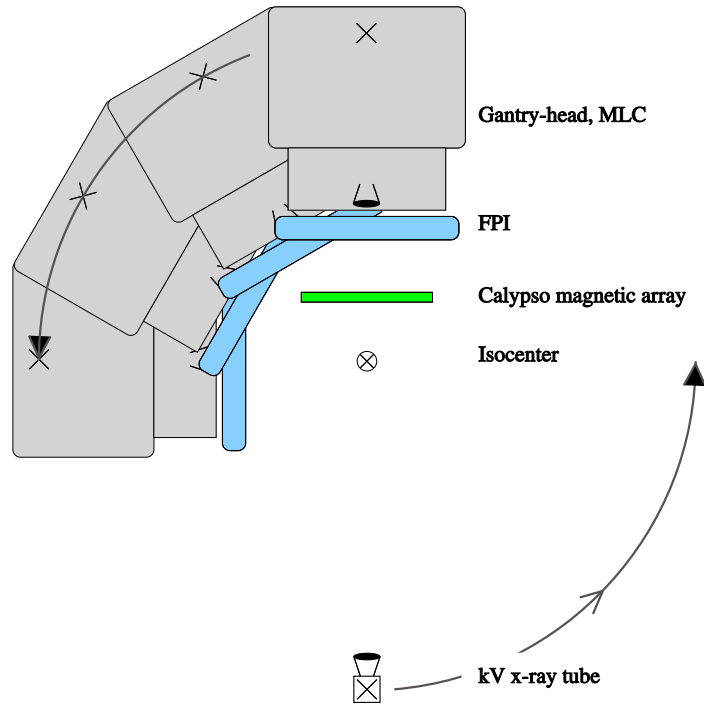
Figure 2.11: *Cross-sectional, frontal view of gantry head, kV flat-panel imager (FPI) in operational position, Calypso magnetic array and isocenter. The drawing is to scale. The rotating gantry clears the magnetic array.*

be confirmed. The minimum separation between kV FPI and magnetic array can become as low as 10 cm.

2.4.1.2 Gantry rotation effects

The effect of the gantry rotation on EM tracking was evaluated under a number of conditions. Two ARTISTE installations, each with an associated Calypso Systems, were available at the DKFZ. Gantry rotation effects were investigated in both installations.

Method   The test procedure consisted of tracking of a static target using the Calypso System while the gantry rotated through a full circle. Ideally, if the gantry rotation had no effect on EM tracking, the EM tracking system would report a constant target position. In reality, gantry rotation can have an effect on EM tracking for at least two reasons: (i) the gantry head or the protruding imaging components may block the line of sight of the Calypso cameras, thereby degrading optical localization of the magnetic array; (ii) gantry mounted, electrically conductive components can get close to the magnetic array (cf. Figure 2.11) affecting the magnetic fields of the Calypso System, thereby impacting magnetic target localization. The latter effect (ii), is referred to as metal-in-field (MIF) interference.

In these tests, the onboard imaging components, such as FPIs and kV x-ray source, were deployed in order to simulate the worst case. In order to test the dependence of gantry rotation effects on the transponder arrangement in the target, two test phantoms

with very different transponder configurations were tracked. One phantom was the body phantom presented in Section 2.3.1; the other phantom was the Calypso quality-assurance (QA) phantom[2]. The transponder coordinates in both phantoms are given in Table 2.3. In the QA phantom, the transponders all lie in a plane parallel to the table surface.

Results   The results of the investigation of the effects of gantry rotation on EM target stability are summarized in Figure 2.12. The static targets I and II corresponded to the
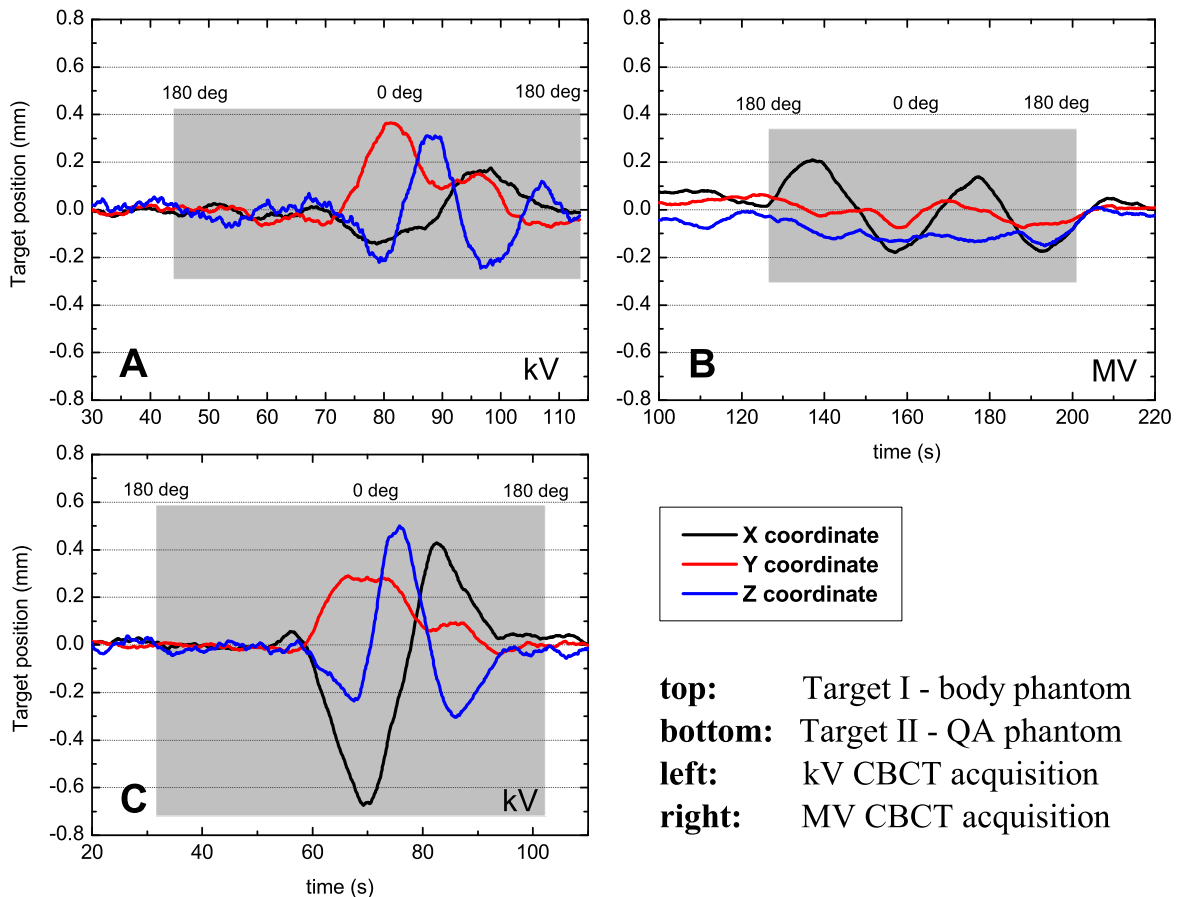

Figure 2.12: *Coordinates of static targets reported by the EM tracking system as functions of time. During the times indicated by the shaded boxes, the gantry performed a rotation around the target starting at the* 180 *degrees position acquiring an MV or a kV CBCT. Numbers above the shaded boxes indicate the gantry angles over time.*

the targets in the body phantom and in the QA phantom, respectively, whose specific transponder configurations are given in Table 2.3. The shaded areas in the diagrams indicate times during which the gantry was rotated in order to acquire a kV or an MV

---

[2]The Calypso QA phantom is a plastic cuboid (roughly $10 \times 10 \times 15\,\mathrm{cm}^3$) that holds three transponders at defined positions and has crosshairs at the surface for alignment to the lasers in the treatment room.

CBCT. In these tests, the gantry started image acquisitions at the 180 degrees position, i.e. below the table. The data was smoothed for clearer presentation, although care was taken to preserve the data peaks. Additionally, an offset was applied to the data so that all coordinates were approximately at zero prior to the rotation of the gantry (shaded boxes). In consequence, the target displacements in Figure 2.12 represent gantry-induced noise effects in the EM tracking data.

The data in Figure 2.12 shows that, based on the signal amplitudes, gantry-induced effects are less pronounced in the MV (panel B) imaging case than in the kV case (panels A and C). A possible explanation is the difference in distances of the FPIs from the isocenter. This distance was 45 cm for the MV FPI and 38 cm for the kV FPI. The smaller the radial distance of the FPI from the isocenter, the more it can contribute to both gantry-induced effects[3]: obstruction of optical markers on the Calypso magnetic array and MIF effects (cf. Section 2.4.1.2). Furthermore, it can be observed that the x-coordinate (black lines in Figure 2.12) exhibits one period of harmonic deviation from the zero level in panels A and C whereas it exhibits two periods in panel B. This is likely because the MV FPI acts as a second interference object that is offset 180 degrees from the gantry. Instead, for kV CBCT acquisition, the kV x-ray source is in the place of the MV FPI but at a greater radial distance from the isocenter (80 cm) and with a more compact spatial extent.

Another finding is that the "flat" target (Target II) seems to be affected more severely by the rotation of the gantry (panel C) than Target I (panels A and B). The maximum peak-to-peak amplitude in panel A is approximately 0.5 mm; it is twice of that in panel C. Hence, panel C represents the worst case of these tests. Gantry effects of millimeter magnitude may represent a problem for the specified accuracy of the Calypso System of 2 mm. In this case, it is conceivable that target-specific calibration data may have to be collected during one gantry rotation that can be used to retrospectively compensate the gantry effects in the EM target tracking data. For the clinical work planned at DKFZ, the ARTISTE Linac will use MV imaging exclusively. Therefore, only panels A and B of Figure 2.12 apply. For the clinical work, these tests suggest that EM target tracking may be subject to gantry-induced noise effects on the order of 0.5 mm maximum.

2.4.2 Treatment table compatibility

Treatment table compatibility with the Calypso System is relevant if the table, or more specifically the tabletop, is composed of electrically conductive materials. In this case, the oscillating magnetic fields produced by the Calypso magnetic array will not only couple energy into the transponders but will also induce eddy currents in the conductive table components. The magnetic fields associated with the eddy currents will, according

---

[3]In principle, with access to the service modes of the Calypso System, the relative contribution of each effect could be investigated separately; this was pursued in this work.

to Lenz's law, counteract the original magnetic fields used to energize the transponders. While a complete analytical description of such magnetic interactions is complex, it is intuitive to believe that eddy current-related magnetic fields will reduce the amount of energy transferred to the transponders per excitation cycle. The extent of the effect will depend strongly on the geometric configuration of the conductive tabletop structures, the transponders and the Calypso magnetic array. Since their geometric configuration in space will vary somewhat between tracking sessions, a universally valid correction of the effect seems infeasible. Therefore, any effects caused by the tabletop's conductive structures need to be avoided altogether.
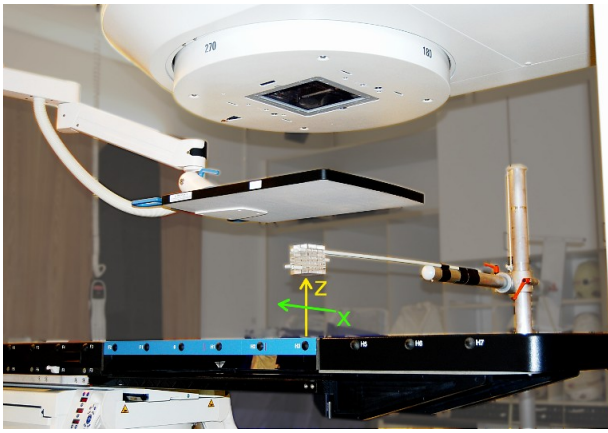
2.4.2.1 Method

Figure 2.13: *Experimental arrangement for the evaluation of table influence on EM target tracking. The table was moved along the z- and x-axes.*
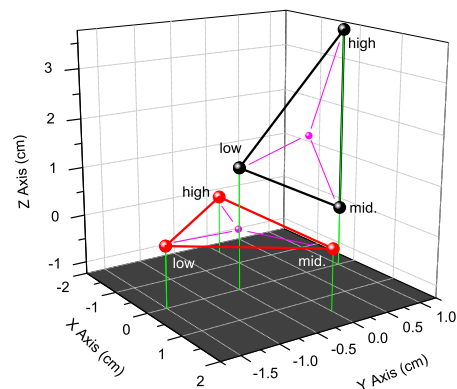
Figure 2.14: *Two test targets (magenta spheres) created by two sets of transponder arrangements (black and red spheres).*

A testing procedure was devised to evaluate the influence of a specific tabletop on the target localization reported by the Calypso System. The principle of the procedure was to maintain a constant geometric configuration of the Calypso magnetic array and the transponders, while the position of the tabletop could be varied. Thus any change in the reported target position could be attributed solely to an effect of the tabletop on the EM target localization. The experimental setup used to realize a constant geometric configuration between Calypso magnetic array and transponders is shown in Figure 2.13. Test targets were set up using the target phantom (see Figure 2.9). The target phantom (the object below the Calypso magnetic array in Figure 2.13) was suspended in space using two fiber glass rods attached to a solid stand. The target phantom was aligned to the room isocenter and the Calypso System was operated in tracking mode. The Calypso magnetic array was always positioned at the greatest permissible distance from the target, which

in all test cases turned out to be between 18 cm and 19 cm. At the beginning of each experimental run, the tabletop was at maximum distance away from the room isocenter in order to obtain a baseline measurement that would not be influenced by table effects. The maximum distance between the upper table surface and the isocenter depended on the tabletop used but was always larger than 60 cm. The table was moved along the z- and the x-axes such that an imaginary point on the table surface, centrally located in x-direction, was displaced along the trajectory points given in Table 2.2. In order to

Table 2.2: *Trajectory points of an imaginary, centrally located point on the table surface relative to the isocenter in cm. The shaded table entries represent the baseline measurements. At each trajectory point, 30 s worth of data were collected, i. e. a complete experimental run lasted ~7 minutes.*

column #	1	2	3	4	5	6	8	9	10	11	12	13	14
x-coord. (cm)	0	0	0	0	0	0	0	0	0	5	10	15	0
z-coord. (cm)	−61.2	−21.2	−16.2	−11.2	−6.2	−5.2	−3.2	−2.2	−1.2	−1.2	−1.2	−1.2	−61.2

test the assumption that the geometric configuration between Calypso magnetic array and transponders was constant, each experimental run was concluded with a baseline measurement, which ideally would provide the same result (within the limits of measurement noise) as the initial baseline measurement. This assumption may be flawed if, for example, the Calypso array position drifted during the measurement or if the phantom suspension sagged.

Two test targets were created as shown in Figure 2.14. In the graph, the red and the black spheres represent the location of the transponders, while the smaller magenta spheres indicate the approximate locations of the centroids of the transponder triangles, i. e. the actual target points of the EM tracking system. The exact location of these target points is unknown to the user as it depends on internally calculated weights assigned to each transponder. The possible geometric configurations of the three transponders are vast. From this vast experimental space, the two test targets were chosen such that they represent two extremes of the possible geometric configurations. In one case (red triangle), the transponders were arranged in a plane parallel to the table surface; in the other case (black triangle), the transponder plane was parallel to the y–z plane. The denominations *low*, *mid.* and *high* characterize the transponders by their resonant frequencies relative to each other. In all cases, the transponders were aligned with their long axis parallel to the y-axis (in Figure 2.14 the transponders are shown in a simplified manner as spheres). The black bottom plane of the graph in Figure 2.14 represents the location of the surface of the tabletop. The planned locations of the transponders are given in Table 2.3 in coordinates relative to the room isocenter. The precision with which the transponders could be positioned was estimated to be within ±2 mm. This relatively

imprecise positioning estimate is due to at least three uncertainties: (i) positioning of the transponders inside the phantom, (ii) alignment of the phantom to the lasers and (iii) uncertainty about the effective EM center of the cylindrical transponders. However, although the initial positioning of the transponders may be imprecise, their position remained constant throughout the experiment allowing so the comparison of the individual target localizations.

Table 2.3: *Room coordinates (relative to isocenter) of the transponders used in the test targets shown in Figure 2.14, in the body phantom (Figure 2.8) and in the Calypso QA phantom.*

[units are cm]	red target			black target			Body phantom			QA phantom		
	X	Y	Z	X	Y	Z	X	Y	Z	X	Y	Z
low freq.	0	−1.5	0	0	−0.5	1.2	−0.71	−1.06	−0.14	−0.56	−1.39	0
center freq. (mid.)	1.5	0	0	0	1	0	1.01	1.25	−0.09	1.49	0.21	0
high freq.	−1.6	0	0	0	1	3.7	−1.4	2.23	1.35	−0.92	1.18	0

Any tabletop that is to be used clinically is required to be compatible not only with the Calypso System but with treatment planning and imaging procedures as well. The tabletops under investigation were also tested concerning these compatibilities (in Section 5.3). In this work, two tabletops were or became available and were thus investigated in more depth: the Siemens TT-D model and the TT-M model (see Table 2.1).

2.4.2.2 Results

Based on these results, a decision was made as to which tabletop model would be used in the clinical trial. Other table compatibility issues such as patient setup, dosimetry or imaging, will be presented specific to the "clinical" tabletop model in Chapter 5.

Tracking impact of TT-D tabletop Figure 2.15 shows the results of EM tracking the red and the black target as functions of the distance between the surface of the TT-D tabletop and the nearest (or lowest) transponder. In Figure 2.15a, the x-axis denotes the distance of the table surface to any of the transponders; in Figure 2.15b, it denotes the distance to the mid frequency transponder. Distances to transponders were chosen as the reference rather than the distances to the target points (magenta spheres in Figure 2.14) because the exact locations of the target points are unknown to the user. The data points at 60 cm distance represent the baseline measurements. One baseline measurement was performed at the beginning and one at the end of each experimental run. Both baseline measurements are shown in the diagrams but they are indistinguishable, which means that the experimental conditions were stable for the duration of an experimental run
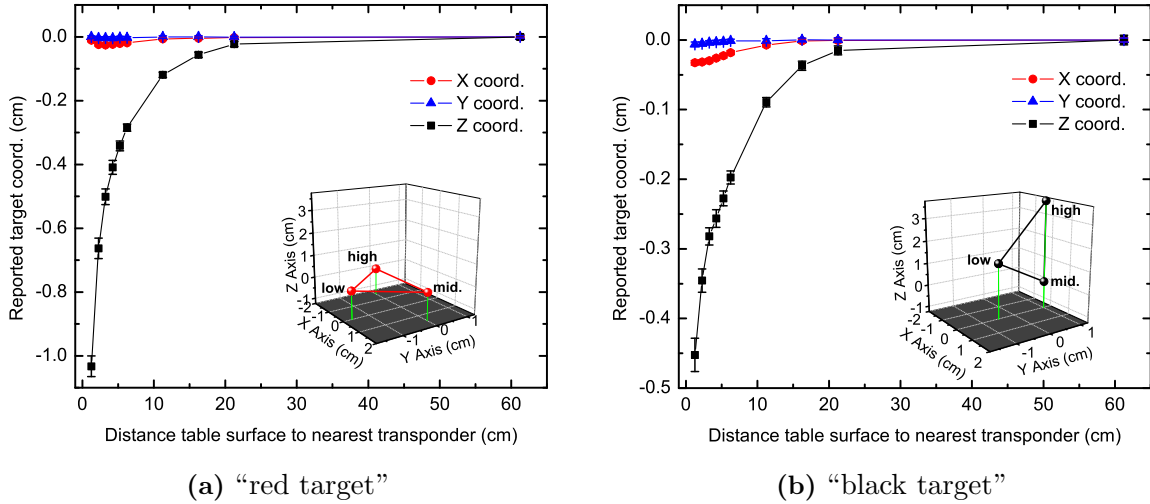
(a) "red target"

(b) "black target"

Figure 2.15: *Target positions as reported by the EM tracking system as functions of the distance to the surface of the TT-D tabletop. The target coordinates are given as deviations from the baseline measurements (outer right datapoints). The transponder arrangements of the red and the black target are shown as figure inserts (originally graphed in Figure 2.14).*

(approx. 7 minutes). The data in Figure 2.15 was collected at the table positions indicated by columns 1–10 and 14 in Table 2.2 on page 22, i.e. the distance of the table to the transponders was varied in z-direction. At each table position approximately 30 s worth of EM tracking data was collected, which amounts to ~300 data points at each table position. The data points at each table position were averaged to obtain the means—displayed as the symbols in Figure 2.15—and the standard deviations were calculated—displayed as the error bars. Any deviation of the data from zero can be interpreted as the localization error of the EM tracking system induced by the tabletop.

One distinct result of the data in Figure 2.15 is that the impact of the tabletop on the EM target localization is almost exclusively on the z-coordinate of the target. The reported z-coordinate (solid black square) of both test targets starts to deviate from its baseline position if the table surface is less than 20 cm away from the nearest transponder. The deviation, or localization error for that matter, is < 1 mm for both test targets as long as the table surface is further away than 10 cm. However, if the table surface gets still closer to the nearest transponder, the localization error becomes target-dependent. The localization error for the red target at 5 cm table distance is approximately 3 mm while it is 2 mm for the black target. The maximum localization error for the red target at 1.2 cm table distance is > 1 cm while it is 4.5 mm for the black target. As the localization error increases (from right to left in Figures 2.15a and 2.15b), the localization precision decreases as indicated by the larger error bars. The target coordinates in x- and y-

direction remain largely unaffected by nearby conductive table structures (save a minor effect on the target's x-coordinate in Figure 2.15b).

The fact that the z-coordinate of the target localization is most strongly affected by conductive table structures may be explained by the effect that eddy currents in conductive structures have on transponder excitation. Eddy currents are expected to weaken the magnetic fields used to couple energy into the transponder circuits (Lenz's law). Subsequently, the transponder will respond to the excitation with reduced signal strength, which the tracking system mistakenly interprets as a greater separation between the transponder and the magnetic array. Localization of the transponders in the plane parallel to the magnetic array (x–y plane) should not depend on signal strength; hence, the target's x- and y-coordinates remain unaffected by nearby conductive structures.

The observation that the maximum localization error is larger in the red target (Figure 2.15a) than in the black target (Figure 2.15b) is intuitively explained by the "vertical arrangement" of the transponders in the black target. In this arrangement, only one of the three transponders gets very close to the table surface while the other two transponders are still further away and will partially compensate the localization error of the lowest transponder (mid. transponder in Figure 2.15b).

It is instructive to analyze the significant target localization errors in z-direction by reviewing the localization of each individual transponder in z-direction. Figure 2.16 shows
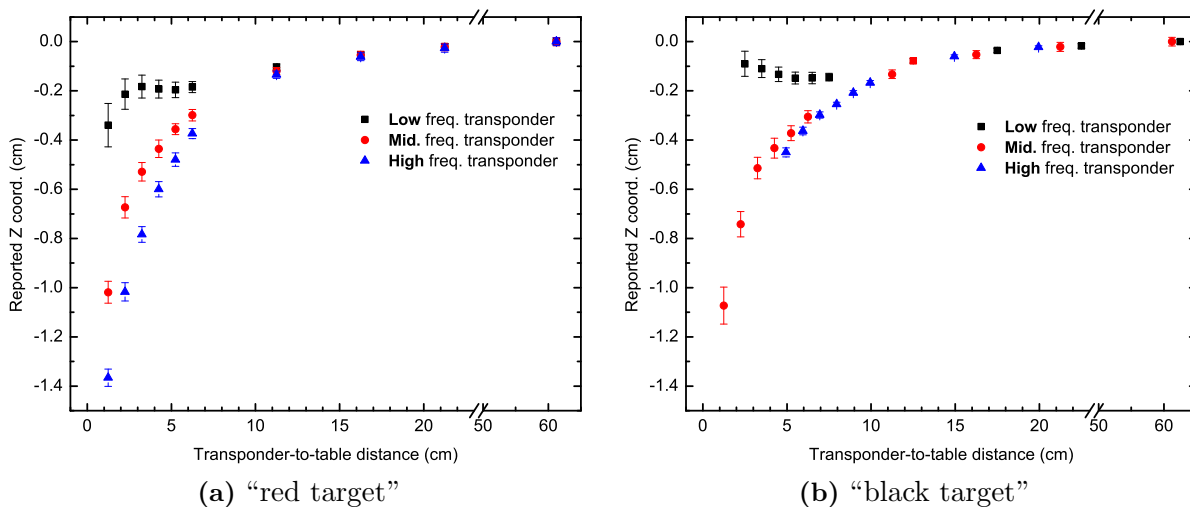

(a) "red target" **(b)** "black target"

Figure 2.16: *The z-coordinate of each individual transponder of the red (a) and the black (b) target as functions of the distance to the surface of the TT-D tabletop. The data sets of each transponder were offset-corrected such that the baseline measurements (outer right data-points) were all at zero.*

the z-coordinates of each transponder as functions of the distance to the surface of the TT-D tabletop. The data was processed and displayed in an analogous manner to the

data in Figure 2.15 with two exceptions. First, only a third of the number of localization measurements (~ 100) went into the calculation of the means and the standard deviations displayed as datapoints and errorbars in Figure 2.16. The reason is that while the Calypso System updates the target position (displayed in Figure 2.15) at $10\,\mathrm{Hz}$, the location of each transponder is only updated at $3.3\,\mathrm{Hz}$. The second exception is that the x-axes in Figure 2.16 show the distance of each transponder to the surface of the table, unlike the distance of only the lowest transponder as in Figure 2.15.

The most instructive data is the result from the red target in Figure 2.16a because, in this transponder arrangement, all transponders are at the same separation from the table surface. The data shows that the localization error increases with increasing resonant frequency of the transponder while the error bars behave inversely. This means that in the presence of eddy current-related disturbances, the transponder with the lowest resonant frequency can still be localized with the highest accuracy but lowest precision while the situation is reversed for the high frequency transponder. Hence, the localization of the transponders by the EM tracking system exhibits at least this one frequency-dependent effect—and possibly others as well. In consequence, the three transponders used to form one EM target can complement each other to provide a robust target (centroid of the transponder triangle) for the Calypso System. It has to be understood that transponders at different resonant frequencies are tracking targets with different physical characteristics. The clinician may sometimes want to obtain the coordinates of the individual transponders from the Calypso System (which is not currently available in the system's standard clinical data output) to estimate target rotation or deformation. However, the data in Figure 2.16 suggests that the use of the coordinates of the individual transponders requires a good understanding of any error sources.

Finally, the effect of the tabletop on the two test targets can be analyzed if the table moves laterally underneath targets. Figure 2.17 shows the results of EM tracking the two static test targets displayed in Figure 2.14 while moving the tabletops laterally underneath the test targets. Displayed is the data collected at the trajectory points of the tabletop given in columns 10–13 of Table 2.2. The datapoints in Figure 2.17 have been produced by the same method as used before for Figure 2.15. In Figure 2.17a, the localization error (absolute values of the datapoints in the graph) of the targets' z-coordinate is largest if the target is centrally located above the tabletop and decreases as the table shifts laterally. This observation indicates a reduced eddy current-related disturbance when the table surface is only partially underneath the Calypso magnetic array. As the table is shifted laterally, the x-coordinate of the target begins to show localization errors of up to almost $2\,\mathrm{mm}$ at $15\,\mathrm{cm}$ lateral table shift, potentially an effect of the asymmetry that is introduced when the lateral edge of the table approaches the target. The targets' y-coordinate remained perfectly stable throughout the experiment.
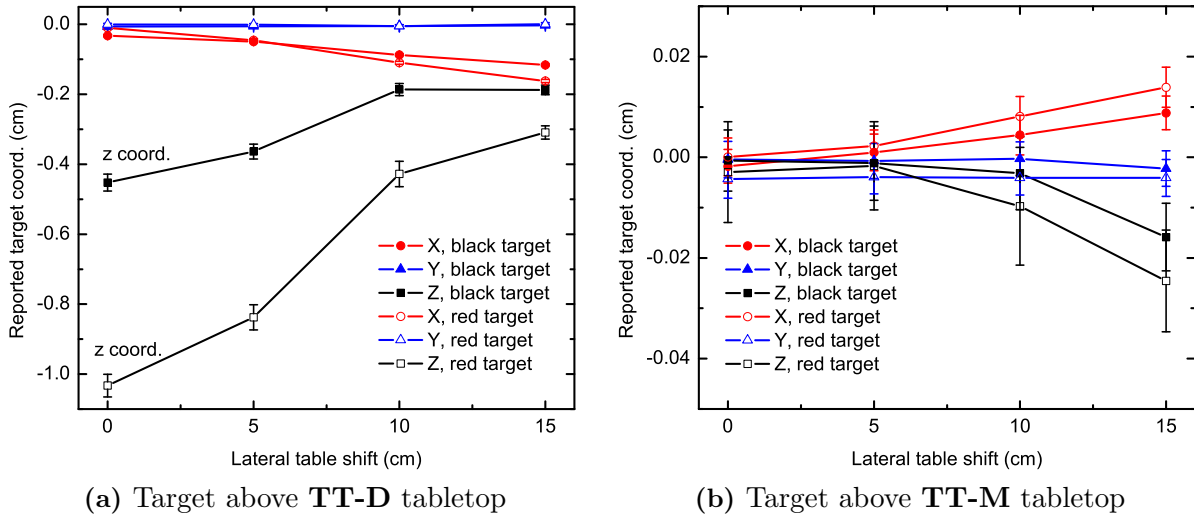
(a) Target above **TT-D** tabletop **(b)** Target above **TT-M** tabletop

Figure 2.17: *Target positions as reported by the EM tracking system as functions of the lateral shift of the tabletop. The target coordinates are given as deviations from the baseline measurements (outer right datapoints in Figures 2.15 and 2.18). The surface of the tabletop was positioned as close as possible (1.2 cm) to the nearest transponder in both the red and the black target (cf. Figure 2.14).*

Tracking impact of TT-M tabletop The second tabletop option that was tested was the Siemens TT-M tabletop in combination with the Calypso overlay (as described in Table 2.1). The overlay has been designed as an accessory to the TT-M tabletop to make it compatible with the Calypso System. The TT-M tabletop provides the basis for EM compatibility by leaving a large open area underneath a potential target in the prostate region that is only framed by a carbon fiber structure. The Calypso overlay then provides a non-conductive Kevlar bridge (blue component in the photograph of the TT-M tabletop in Table 2.1) above this void and with 7 cm separation in z-direction from the TT-M structure. The reward of such efforts can be seen in Figure 2.18. The experimental method and the data processing were identical to those underlying Figure 2.15. This time, no localization error is measured; the datapoints in Figure 2.18 remain, within a low amount of noise, at the level of the baseline measurement even down to the smallest separation from the surface of table. The precision of localization, i.e. the errorbars, is stable over the range of distances from the table. The precision is slightly better for the black target then for the black target and it is better by factors of roughly 2–5 compared to Figure 2.15 as the target gets closer to the table surface (note the different scales of the y-axes in the Figures 2.15 and 2.18).

The test of the table impact at lateral table shifts resulted in very small localization errors. Figure 2.17b shows that these localization errors were well below 0.2 mm. In contrast to the data measured from the TT-D tabletop (Figure 2.17a), the localization
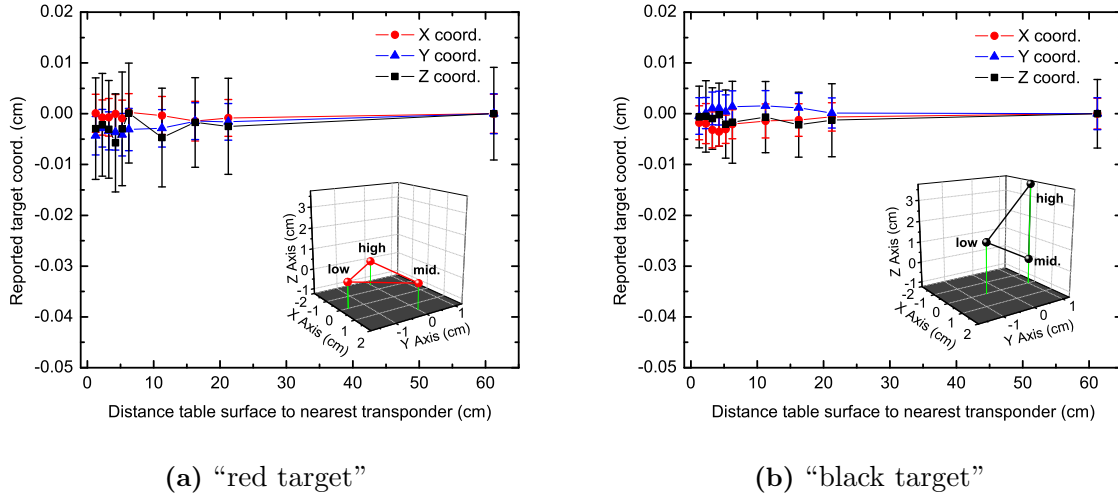
(a) "red target" (b) "black target"

Figure 2.18: *Target positions as reported by the EM tracking system as functions of the distance to the surface of the TT-M tabletop. The target coordinates are given as deviations from the baseline measurements (outer right datapoints). The transponder arrangements of the red and the black target are shown as figure inserts (originally graphed in Figure 2.14).*

errors measured here have the tendency to increase as the targets are located closer to the edge of the table. This can be explained by the carbon fiber beams of the TT-M frame that move in underneath the test targets. As the carbon fiber beams get closer to the targets, disturbances begin to appear. However, with localization errors $< 0.2\,\text{mm}$, these disturbances are of no clinical significance.

Summary The above results provided valuable insight into the interaction of two Siemens tabletop models with Calypso EM target tracking. Nevertheless, the experiments covered merely a small fraction of the experimental degrees of freedom. Numerous additional experimental parameters could be investigated such as other transponder configurations (and permutations of the resonant transponder frequencies in each configuration), variable transponder orientation, variable geometries between the Calypso magnetic array and the transponders or experiments with only two transponders per target to simulate the effect of one implanted transponder failing[4]. Such extensive testing has been performed by the engineering department of the system manufacturer Calypso Medical. The purpose of the testing at DKFZ was to decide on a tabletop that would be used in a subsequent clinical trial.

The TT-D tabletop clearly has the advantages that established and optimized proce-

---

[4]Willoughby *et al.* [31] reported that 2 out 60 implanted transponders were not available for localization: one transponder was voided through the urethra; the other one was technically unresponsive.
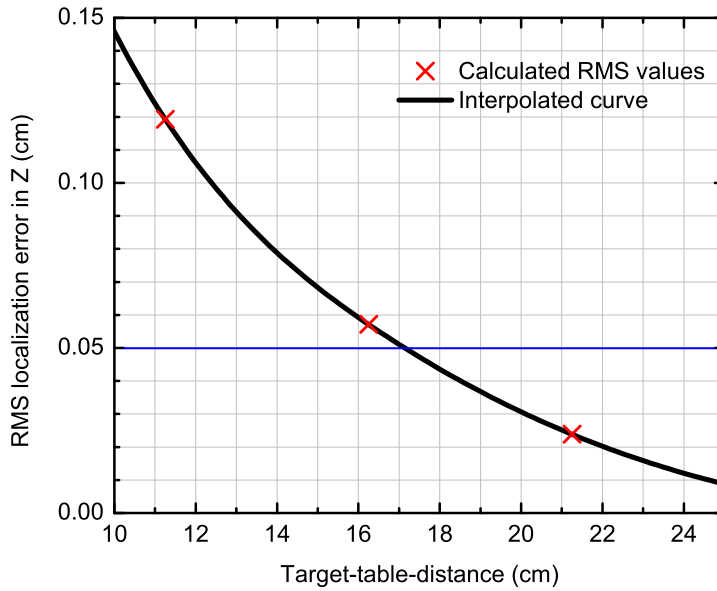
Figure 2.19: *RMS localization error of a simulated prostate target (red target of Figure 2.14) as a function of the separation from the TT-D tabletop. Shown are RMS values calculated from measurements (red crosses) and interpolated RMS errors (black line).*

dures (and accessories) are in place for patient setup, imaging and dosimetry, while these would have to be determined for the TT-M tabletop. The disadvantage of the TT-D tabletop is its detrimental impact on EM tracking presented above in Section 2.4.2.2. In contrast, the TT-M tabletop together with the Calypso overlay was perfectly compatible with EM tracking, but it is expected to present greater problems for imaging and dosimetry. For the radiotherapy department at DKFZ, it would have been desirable to make the established TT-D tabletop compatible with EM tracking. For that matter, the results above suggest that implanting the high frequency transponder at the greatest distance from the tabletop and maintaining a large enough separation of all transponders from the tabletop may keep the table-induced target localization error below 0.5 mm root-mean-square (RMS), which is the manufacturer's limit. Implanting the high frequency transponder at the greatest distance from the tabletop seems impractical for prostate patients because the recommended implant locations (apex, left and right base) lie on a plane that is rather horizontal to the table surface (comparable to the "red target" in Figure 2.14). The distance necessary to keep the RMS localization error within acceptable bounds can be estimated from Figure 2.19. The data in Figure 2.19 was obtained by expressing the average localization error of the z-coordinate shown in Figure 2.15a as RMS values (red crosses) and performing a B-spline-based interpolation (black line) to estimate the RMS errors in between the measured values. Only the portion of the data is shown when the target is between 10 cm and 25 cm away from the table surface, which is the separation expected for a clinical prostate target. At DKFZ, the standard patient positioning equipment provides a separation of 8 cm between the patient's skin surface and the table. A typical prostate target will be—and by Calypso standards, is expected to be—at least 6 cm away from the dorsal skin surface (patient in supine position). This

amounts to a total target-table-distance of at least 14 cm in a patient. According to Figure 2.19, a separation of 17 cm or larger would be needed to achieve localization errors smaller than the 0.5 mm limit. The results in Figure 2.19 represent one set of experimental conditions. Any variation in the parameters will affect the localization error. For example, it can be deduced from Figure 2.16a, that a failing of the low frequency transponder would result in a two-transponder target with worse localization accuracy, i. e. the curve in Figure 2.19 would be shifted towards the right. Overall, it was decided that even if some centimeters of additional spacer material were added to the standard DKFZ patient positioning technique, it will be difficult to guarantee an acceptable localization error using the TT-D tabletop. Therefore, the TT-M tabletop was chosen as the candidate tabletop for the clinical study—with the implications presented in Section 5.3.

2.4.3 Irradiating through the magnetic array

The dosimetric effect of irradiating through the Calypso magnetic array was quantified in order to determine whether the magnetic array needed to be included in the treatment planning.

2.4.3.1 Method

A typical nine-star intensity-modulated radiation therapy (IMRT) plan was verified using the PTW 729 2D array inside a cylindrical water equivalent verification phantom (PTW Freiburg GmbH). The maximum beam energy was 6 MeV photons. The plan verification was performed once with the Calypso magnetic array in operating position, i. e. suspended above the phantom, and once with the magnetic array removed (see Figure 2.20a). The magnetic array was not included in the treatment planning of the test case. Figure 2.20b shows a color-washed representation of the planned dose distribution as calculated by the treatment planning system (TPS). The figure shows the circular shape of the phantom with a horizontal 2D array of air filled ionization chambers.

With the magnetic array in operating position (Figure 2.20a), three out of the nine beams traversed the magnetic array before entering the phantom. These three beams—at gantry angles of 320, 0 and 40 degrees (as indicated in Figure 2.20b)—were measured separately to quantify the dosimetric effect individually. The remaining six beams were delivered en bloc.

2.4.3.2 Results

Figures 2.21 to 2.24 show the results of comparing an IMRT plan verification performed with the Calypso magnetic array in place to a verification of the same plan delivered without the Calypso magnetic array present. The pixels in the left-sided images each
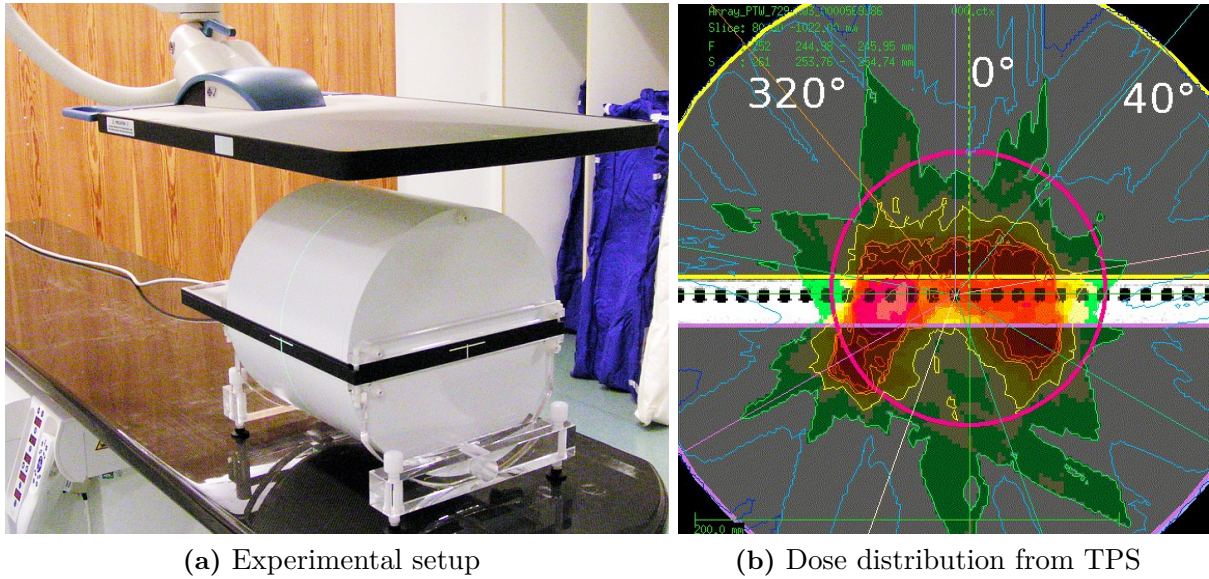
(a) Experimental setup   (b) Dose distribution from TPS

Figure 2.20: *(a) The PTW 729 2D array embedded in a cylindrical, water-equivalent phantom. The Calypso magnetic array is deployed in the operating position above the phantom. (b) Transversal CT slice through the phantom with the color-washed dose distribution of the treatment plan.*

represent one of the 27×27 ionization chambers of the 2D array detector (see Figure 2.20). The color-coded intensities of these pixels represent the differences in per cent between the chamber readings obtained from delivering the IMRT plan with the magnetic array in position and the readings obtained with the magnetic array removed. Readings smaller than 5% of the maximum value in the array were ignored in order to prevent the comparison of noise-dominated readings. This explains the green pixels in the periphery of the radiation fields[5]. For orientation, the right-sided images in Figures 2.21 to 2.24 show isodose lines of dose distribution measured in the plane of the chamber array when the magnetic array was in place. While Figures 2.21 to 2.23 show the results obtained from separately analyzing the individual beams traversing the Calypso magnetic array, Figure 2.24 shows the result from comparing the complete IMRT plan including all nine beams.

In general it was observed that the Calypso magnetic array attenuated a small fraction of the entrance fluence causing a loss of dose in the target volume (or "target plane" as measured by the 2D detector array). Analyzing the array-traversing beams separately (Figures 2.21 to 2.23) shows that the Calypso magnetic array accounts for a decrease of dose in the target of up to 3%. The dose loss is more pronounced in the beams that

---

[5]Note that the legends in Figures 2.21 through 2.24 by default cover large range of values. The actual readings do not explore the full range of the legends. For example, the highest readings in Figure 2.21 are three pixels of a "saturated yellow" color representing deviations in the range 3%–5%.
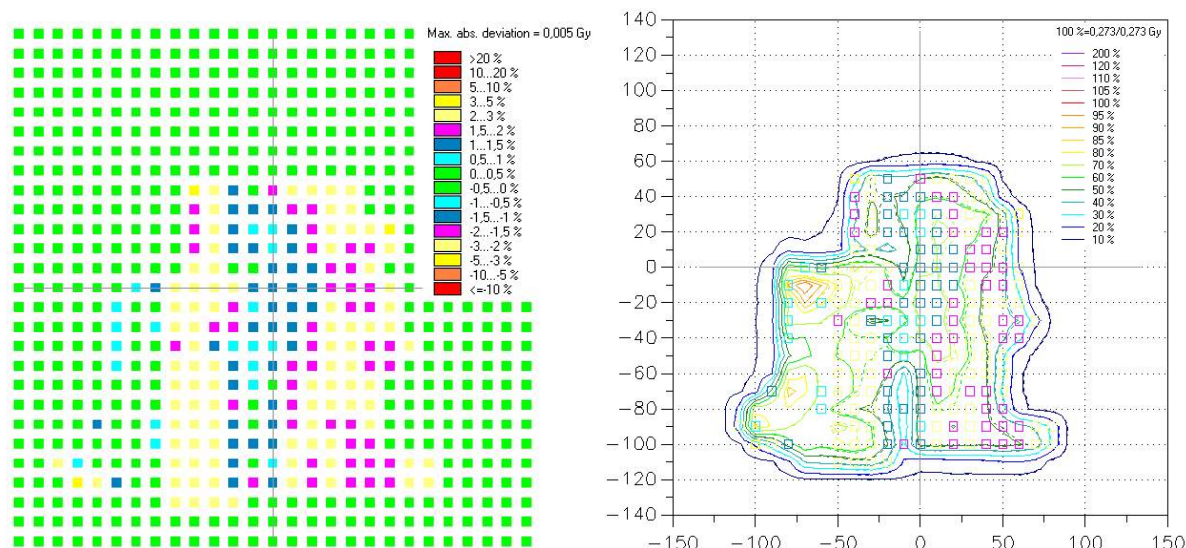
Figure 2.21: *Difference map of an IMRT beam verification.* **The gantry was at 320 degrees**. *The same IMRT field was delivered once with and once without the Calypso magnetic array in place. The percentage difference in dose is shown.*

obliquely traverse the magnetic array (Figures 2.21 and 2.23) than in the case when the beam traverses the magnetic array orthogonally (Figure 2.22). When the beam passes orthogonally, the dose loss does not exceed 2% in the radiation field. The difference in dose loss between orthogonally and obliquely traversing beams may be explained by the pathlengths of rays through the magnetic array. This pathlength is at a minimum for orthogonal rays and increases as the angle of incidence is becoming increasingly oblique.

Analysis of the dose differences in the verification of the complete IMRT plan (Figure 2.24) shows that the differences within the target are within ±1%. The right-sided image in Figure 2.24 shows the difference values as hollow squares on top of an isodose-line representation of the dose distribution. The same color code applies to both the hollow squares and the solid squares. However, in the right-sided images, only difference values greater than ±0.5% ("non-green values") are shown. Within the 20% isodose line, approximately two thirds of the differences are smaller than ±0.5% (i. e. values are ignored in the right-sided image of Figure 2.24) and another third of the differences is in the range from 0.5% to 1% (cyan squares). Outside of the 20% isodose line, larger differences become apparent. These can sporadically be as large 3% to 5%.

From these results it can be concluded that despite the presence of the Calypso magnetic array, planned dose distributions can be delivered accurately, i. e. discrepancies caused by the magnetic array are expected to stay within tolerance. The tolerance for discrepancies between planned and measured dose distributions at DKFZ is 3%. The magnetic array will not have to included in treatment planning. In any case, each treat-
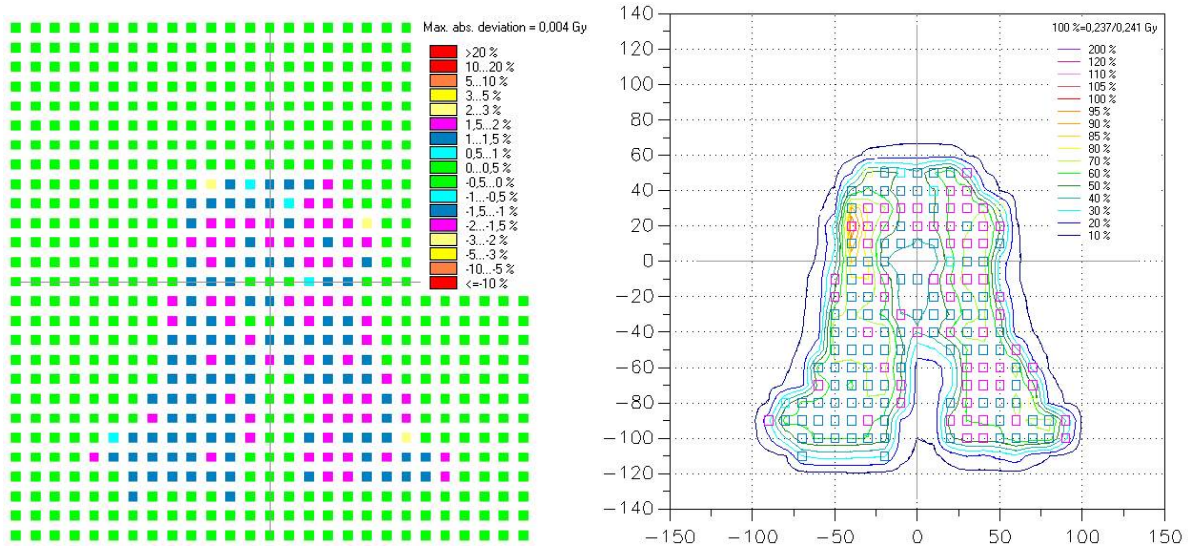
Figure 2.22: *Difference map of an IMRT beam verification.* **The gantry was at 0 degrees**. *The same IMRT field was delivered once with and once without the Calypso magnetic array in place. The percentage difference in dose is shown.*

ment plan will be verified prior to treatment in a way similar to the method described here (Section 2.4.3.1). If intolerable discrepancies arise, they will be detected in this process.

2.4.4 Integration of EM tracking with a dynamic multileaf collimator

The dynamic control of an MLC (DMLC) promises to provide the ultimate remedy against treatment uncertainties introduced by intrafraction target motion, in the case of a technically ideal implementation. The concept of DMLC is that information about the current target position is fed in real-time to the MLC. *Real-time* refers to time scales that are short compared with the period over which the tumor moves. The MLC controller must then be able to calculate the optimal shape and location of the MLC aperture based on the real-time target position. Subsequently, the MLC leaves would realize the optimal aperture thus ensuring that the treatment beam always hits the tumor and only the tumor (in its projection along the beam axis). This concept has the potential to achieve geometrically accurate dose delivery at almost 100% beam duty cycle, in contrast to gated dose delivery schemes procedures that typically operate at duty cycles below 50% [32, 33]. In clinical implementations, uncertainties in the target motion measurements, in the MLC leaf motion and due to latencies inherent to the flow and processing of information will limit the level of precision of the target tracking. Nevertheless, a few groups have begun to publish promising results using MLCs of different vendors [34–36]. At DKFZ, the work of Tacke [37] resulted in a workable DMLC system using the 160 MLC of the Siemens
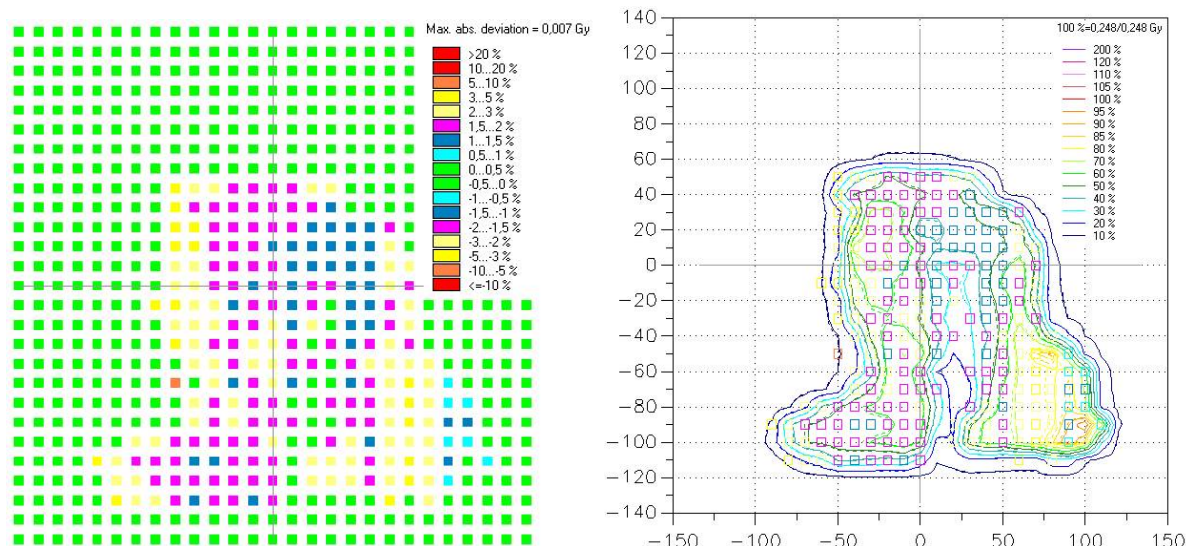
Figure 2.23: *Difference map of an IMRT beam verification.* **The gantry was at 40 degrees**. *The same IMRT field was delivered once with and once without the Calypso magnetic array in place. The percentage difference in dose is shown.*

ARTISTE solution.

Clearly, the target motion measurement provided by the Calypso System is well suited to control a DMLC: it is a direct (as opposed to a surrogate) measure of target position, it can monitor target motion continuously and at a high enough update rate (10 Hz). However, real-time data output from the Calypso System is in a prototypical stage. The real-time data interface will be a data stream based on the User Datagram Protocol (UDP). Modifications to the Calypso System are necessary to implement the real-time interface. These modifications are scheduled to occur whenever the manufacturer has fully developed them. For the time being, DKFZ was provided with a simulator software that provides the UDP stream as it would come out of the Calypso System. That way, the workflow depicted in Figure 2.25 could be realized. The Calypso System was used to track a moving phantom. The tracking data was exported offline in Excel spreadsheet format. This format was converted to the input data format of the Calypso Simulator, which, in turn, provided the tracking data in the form of a UDP stream to the DMLC. The DMLC system was able to process the real-time data provided by the Calypso Simulator and to drive the MLC leaves appropriately as illustrated in Figure 2.26. This proof-of-concept promises that in the future the 160 MLC can be controlled dynamically using the real-time target information provided by the Calypso System.
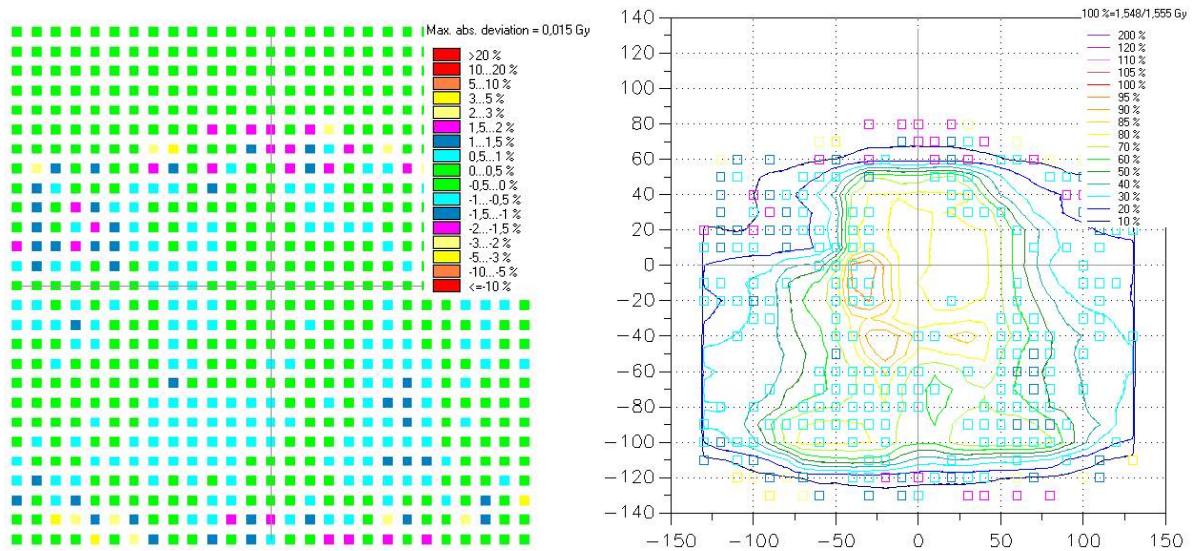
Figure 2.24: *Difference map of a **complete IMRT plan** verification. The same IMRT plan was delivered once with and once without the Calypso magnetic array in place. The percentage difference in dose is shown.*
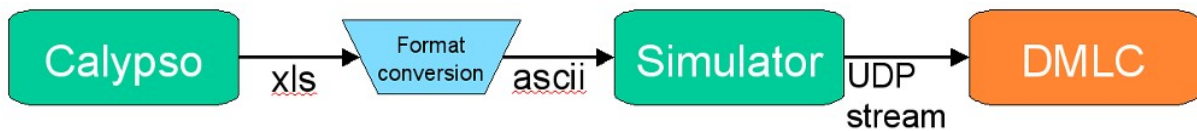

Figure 2.25: *Simulator-based workflow to demonstrate the integration of EM tracking with the DMLC control.*

Summary

This chapter introduced the Calypso System for EM tumor tracking, the Siemens ARTISTE radiotherapy solution and the main experimental phantoms used in this work. Subsequently, investigations concerning the compatibility of the EM tracking system with the radiotherapy environment were presented. These investigations demonstrated that the EM tracking system and the Linac can be operated without collision hazards (geometric clearance), that the TT-M tabletop should be used for the clinical trial, that the magnetic array can be ignored in treatment planning and that the EM tracking system can provide the motion information necessary for controlling a DMLC in real-time.
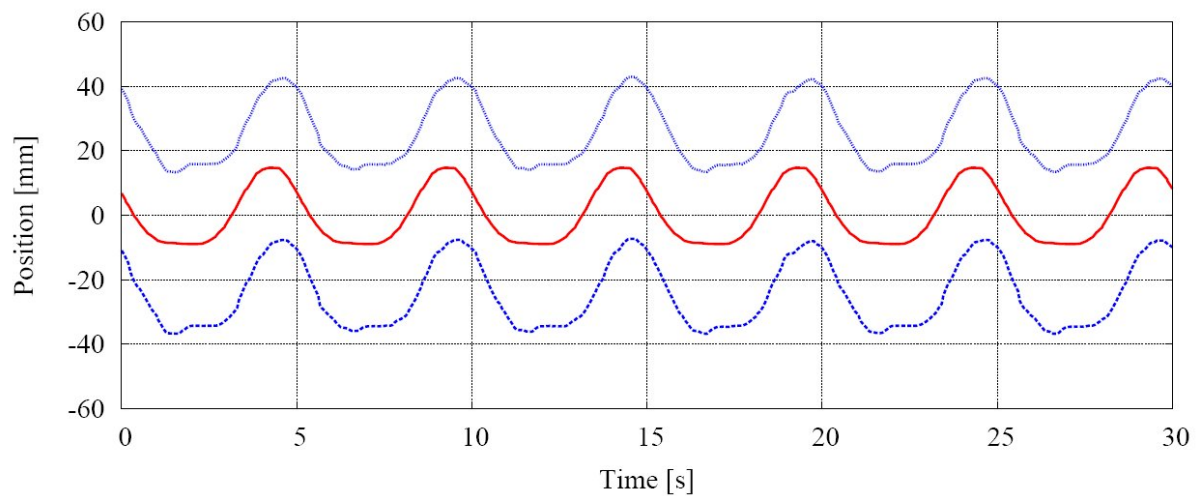
Figure 2.26: *Motion of a sample leaf pair (blue lines) of the DMLC in response to breathing motion measured by the Calypso System (red line). The upper blue line denotes the leading leaf; the lower line the trailing leaf. The leaves follow the breathing motion in near-realtime. A slight time delay is observed caused by the inertia of a linear prediction filter used to compensate system latencies. (Graph reproduced with permission from Tacke [37].)*

Chapter 3

Electromagnetic tracking and x-ray imaging

This chapter presents the integration of EM target tracking with x-ray imaging. Parts of the chapter have been published in a peer-reviewed article [19] and presented at an international conference [17]. The advent of IGRT has made *online* (i. e. at treatment time and with the patient in treatment position) x-ray imaging available with modern Linacs. Other imaging modalities such as magnetic resonance imaging (MRI) are beginning to find their way towards the patient on the treatment couch[38], but at the time of writing (early 2009), it is x-ray imaging in a number of flavors that builds the basis of IGRT. For the present work at DKFZ, three x-ray imaging options were available in the context of different installations of the Siemens ARTISTE Solution (as introduced in Section 2.2):

MV imaging: Portal imaging, portals-during, cone-beam computed tomography

kV imaging: Radiographs, fluoroscopy, cone-beam computed tomography

CT-on-Rails: kV fan-beam computed tomography.

Integration of EM tracking with x-ray imaging requires as a minimum that both technologies can be used concurrently and/or that information is transferred or exchanged between both technologies. To date, an integration in that sense has not been implemented commercially: the Calypso System is declared incompatible for concurrent use with x-ray imaging and consequently no real-time information exchange between both technologies is available. At the same time, there would be many benefits of such an integration.

One potential benefit is the dual-purpose of the transponders as markers both for EM tracking and for imaging. This would enable a cross-verification of the localizations reported by the two localization methods. Furthermore, detectability of the Calypso transponders in the x-ray images can enable advanced image processing techniques such

as fiducial-based patient setup [39] or automated organ segmentation [40]. Some automated organ segmentation techniques such as active contour models [41] require an algorithmic starting point inside the organ to be segmented. If the Calypso transponders can be detected reliably by image processing, their locations provide a suitable starting point to active contour algorithms. Another interesting application that is conceivable if the transponders are detectable in portals-during is an online verification and safe-guard mechanism for dynamic treatments such as arc-modulated radiotherapy or DMLC [35, 42]. The positions of the transponders relative to the radiation field edges could be compared to the planned positions. Any discrepancy would indicate an erroneous correlation between MLC motion and target motion and a user warning could be generated. Retrospective analysis of the transponder motion within the radiation fields would be an important step for the reconstruction of the dose delivered to the patient in the presence of organ and MLC motion.

Another potential use of integrated EM tracking and x-ray imaging is the management of organ motion in imaging applications. Imaging techniques such as CBCT can suffer from image artifacts caused by organ or patient motion [43]. Use of the 3D target position as measured by the Calypso System during the imaging procedure offers a unique possibility for the correction of motion artifacts or even for the reconstruction of motion-correlated datasets.

Lastly, close integration of EM tracking with x-ray imaging would allow to make better use of imaging time, imaging dose and imaging cost. The current strategy in IGRT is to image with some pre-defined frequency—for example, before each treatment fraction. After analysis of the images, the result may be that organ motion has not occurred and thus the imaging session could have been spared. Currently imaging is driven by suspicion or statistics on patient populations. Instead, using a tightly integrated EM tracking system, the target can be localized without investing radiation dose and time. Subsequently, an imaging session could be triggered any time before or during treatment if a demand is derived from the EM data. This leads to *demand-driven* imaging. Conceivable implementations of this concept will be discussed in Section 6.1.1.1.

3.1 Methods

It was an objective of the present work to integrate EM tracking with the online imaging options available at DKFZ. To this end, investigations concerning transponder detectability will be presented, a fast transponder-tracking algorithm will be introduced and concurrent usage of EM tracking and x-ray imaging will be enabled through the development of a synchronization interface. An application of the integrated system—4D CBCT—will be demonstrated in Chapter 4.

3.1.1 Transponder detectability in x-ray images

Detectability of the Calypso transponders in the x-ray images is the basis of correlating the Calypso target localization with the image-based target localization. The central question in terms of detectability was whether the transponders could be detected in MV x-ray images (as opposed to kV). Others had reported that the transponders could not be reliably identified in MV portal images [31]. Their finding was based on Siemens MV imaging equipment but not on the latest system components as they were available with the ARTISTE at DKFZ. An investigation of transponder detectability in MV images was also relevant for practical reasons: the patients to be enrolled in a clinical study using the Calypso System at DKFZ, will be treated using an ARTISTE Linac that, in terms of onboard imaging options, features MV imaging exclusively. Transponder detectability in kV images was not investigated explicitly as it was reported by others [31, 44] and it will be confirmed and demonstrated implicitly in the work on automatic transponder detection presented in Section 3.1.2.

3.1.1.1 MV x-ray projection images

Transponder visibility in MV x-ray images was tested using two different MV imaging modes available on the ARTISTE (consult Section 2.2 for details): full-field portal images and portals-during. The Calypso System was not in operation during the imaging performed in this section. The body-phantom (Figure 2.8) was used for the imaging experiments as it features an amount, shape and composition of scattering and absorbing media that resembles the human pelvis.

3.1.1.2 MV cone-beam computed tomography

To test for transponder visibility in MV CBCT data, the body-phantom shown in Figure 2.8 was scanned. A full scan of the phantom was performed, which means that the gantry rotated a full 360° acquiring images at a rate of one frame per degree [23]. The standard reconstruction procedure of the clinical ARTISTE Linac was used to generate the 3D dataset.

3.1.2 Transponder-tracking image processing

To compare the 3D transponder positions reported by Calypso System to their projected position on the plane of the FPI, a transponder-tracking image processing algorithm (TTA) was developed. Previously, a number of seed-localizing algorithms have been reported that mostly served the purpose of localizing internal fiducial markers or brachytherapy seeds in the prostate both in kV and MV projection x-ray images [45–47].

In this work, a new algorithm was developed guided by the requirements of the problem at hand: (1) the TTA should be fast (processing time per frame $\approx 100\,\text{ms}$ = Calypso cycle time) in order to be suitable as an additional real-time target tracking method beside the Calypso System; (2) the number and the approximate positions of the Beacon transponders in the images will be known *a priori*, which should be exploited by the TTA; (3) the contrast of the Beacon transponders in the x-ray images is expected to be lower than the contrast of gold seeds[1] typically processed by previous seed-localizing algorithms, which requires the TTA to handle low-contrast conditions and false-positive detections appropriately.

Figure 3.1 sketches the flow of processing steps of the TTA. In the following text, the rationale and the function of the processing steps will be explained.
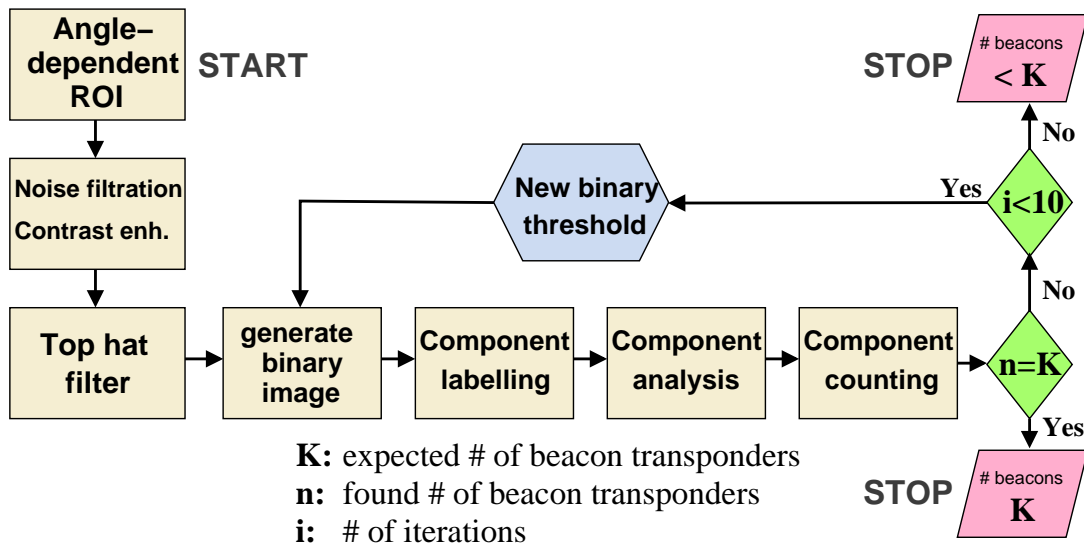

Figure 3.1: *Flow diagram of the transponder-tracking image processing algorithm (TTA). Ultimately, transponder localization is performed on binary representations of the x-ray images. An appropriate binary threshold is determined iteratively. Details of individual processing steps are given in the text.*

3.1.2.1 Region of interest determination

First, the TTA calculates a per-frame region of interest (ROI) in the x-ray images based on both the angle of projection of the current image (gantry angle) and the position of the Beacon transponders at planning time. The ROI has to be as small as possible to minimize computation time, but large enough to ensure the transponders are inside the ROI. The ROI then is the bounding box defined by the transponder positions at planning time in the FPI's plane plus an additional margin that accounts for transponder motion.

---

[1]The average electron density of Calypso transponders is approximately a third of that of gold markers.

The procedure to determine the ROI is based on the DKFZ procedure to account for non-ideal geometries in the reconstruction of CBCT. This procedure consists of the experimental estimation of a set of projection matrices $\boldsymbol{P}$ for each gantry angle that map the 3D room coordinates, (x, y, z), to 2D detector coordinates (u, v). In order to obtain estimates of the projection matrix, a hollow perspex cylinder is imaged from all relevant gantry angles. A set of 37 steel spheres is embedded in helical arrangement in the cylinder wall. The center of the cylinder is positioned precisely at isocenter using the room lasers and thus the room coordinates of the steel spheres are known [48]. From the projected positions of the steel spheres on the detector, projection matrices $\boldsymbol{P}$ can be calculated for each gantry angle [49].

An appropriate ROI is determined by projecting the 3D transponder positions previously determined from the planning CT onto the detector plane using

$$\lambda \left(u, v, 1\right)^{\mathrm{T}} = \boldsymbol{P} \left(x, y, z, 1\right)^{\mathrm{T}}, \tag{3.1}$$

where λ is a scaling factor, u and v are the 2D x-ray image coordinates of the transponders, x, y and z are the 3D room coordinates of the transponders and $\boldsymbol{P}$ is the projection matrix as described above. Based on this estimation of the 2D image coordinates of all three transponders, a bounding box enclosing the transponders can be constructed. Finally, the bounding box is enlarged by some margins to reflect the amount of expected transponder motion. Appropriate margins can be determined in a "back-of-the-envelope" calculation. Using the prostate as an example, we may estimate that each transponder would deviate from its position at planning time by a maximum of $\pm 1.5 \, \mathrm{cm}$. Applying intercept theorems, this motion estimate translates to a motion of $\pm 2.1 \, \mathrm{cm}$ amplitude in the detector plane, which in turn translates to roughly 55 detector pixels (given a pixel pitch of the detector of $400 \, \mu\mathrm{m}$). Hence, a margin of 55 detector pixels could be a reasonable starting point for the prostate application. If necessary, the margin value can be fine-tuned later or more sophisticated methods of margin determination can be employed, e. g. anisotropic margins, if a preferred direction of motion is known *a priori*.

3.1.2.2 Preparatory processing

In the second step of the TTA, a single walk-through the ROI is performed to filter noise and to enhance the contrast. Throughout this work an attempt is made to consistently use the following notation: f, h and g denote 2D image matrices or filter kernels; u and v denote image coordinates (indices) with ranges of $[1 \ldots M]$ and $[1 \ldots N]$, respectively and i and j denote kernel indices.

Median filter for noise reduction A fast median filter was implemented based on an algorithm proposed by Kopp and Purgathofer [50] that exploits spatial correlation in pixel neighborhoods thereby reducing the number of pixel comparisons by a factor of > 3 compared to the standard implementation. In contrast to the standard implementation that uses 3×3 pixels kernels, the algorithm used in this work operated on a 4×3 kernel. Using Figure 3.2 for illustration, the steps of the algorithm are:
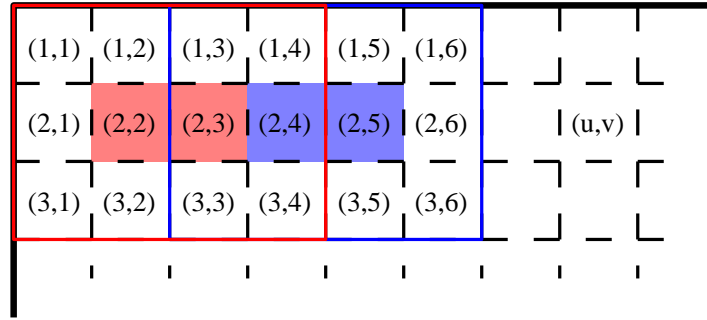
Figure 3.2: *Illustration of the implementation of an efficient median image filter. Shown is the upper left corner of an image. The pixel intensities, h, are arbitrary (and not shown); the numbers inside the pixels are pixel coordinates (u, v).*

1. initialize a filter kernel, i.e. fill a 12-element array with pixels values from a 4×3 pixels neighborhood (red box in Figure 3.2),

2. in the kernel, sort all four columns of the 4×3 pixels neighborhood in ascending order,

3. merge sort the middle two columns of the kernel (red box) into a temporary six-element array in ascending order.

4. The *first* median value (for pixel $h_{2,2}$ in the red box) is obtained by initiating a merge sorting operation using the *first* column of the 4×3 filter kernel (red box) and the temporary six-element array. Merge sorting stops early once the fifth element of the resulting array (which would have nine elements if merge sorting was completed) is determined. This fifth element is the median value assigned to the pixel $f_{2,2}$ of the output image.

5. The *second* median value (for pixel $h_{2,3}$ in the red box) is obtained by initiating a merge sorting operation using the *last* column of of the 4×3 filter kernel and the temporary six-element array. Merge sorting stops early once the fifth element of the resulting array is determined. This fifth element is the median value assigned to the pixel $f_{2,3}$ of the output image.

6. The next filter kernel is initialized using the latter two columns of the previous kernel, $(h_{1-3,3-4})$, as the first two columns of the new kernel and importing two new columns from the image, $(h_{1-3,5-6})$. In other words, in Figure 3.2 move the red box two pixels to the right so it becomes the blue box.

7. Only the last two columns of the blue kernel need to be sorted in ascending order. The first two columns are still sorted because they formed part of the previous kernel.

8. Continue with step 3.

Applying the algorithm to the blue box will yield median values for the pixels with indices $(2, 4)$ and $(2, 5)$. The algorithm processes the image row-wise. Appropriate measures need to be taken at the end of a row if the width of the image in pixels is uneven.

Linearization   It is often desirable to perform a log transformation on x-ray projections, in order to linearize the relationship between the distribution of electron densities in the objects imaged and the projections. This is a standard processing step in CT reconstruction. Thus in theory, a log transformation of the form

$$f(u, v) = \log[h(u, v) + 1] \tag{3.2}$$

compensates the exponential x-ray absorption. The benefit in the present application is that the transponder gray-values in the image would differ by an image-wide constant from their local backgrounds. If subsequently the transponder backgrounds are subtracted from the image, the transponders would exhibit constant contrast, which should ease their detection. (Such a background subtraction is, for example, part of the top-hat filtration described below in Section 3.1.2.3.) In reality, the exact transfer characteristics of the log transformation depend on the range of input pixel values. A power law transformation with adaptive exponent could achieve similar results that are independent of the range of input pixel values. However, the power law transformation can only approximately compensate exponential x-ray absorption. In this work, the log transformation was mostly applied but it was found unnecessary for the successful execution of the algorithm, which is why it was not mentioned explicitly in Figure 3.1.

Contrast enhancement   The contrast of the image was enhanced by linearly mapping the pixel values to the maximum range using the formula

$$f(u, v) = \frac{h(u, v) - h_{min}}{h_{max} - h_{min}} \times \left(2^d - 1\right), \tag{3.3}$$

43

where $h(x, y)$ is the original image, $f(x, y)$ is the output image, h_{min} and h_{max} are the minimum and maximum pixel values, respectively, encountered in the original image and d is the bitdepth. For sake of efficiency, h_{min} and h_{max} where determined already during the previous median filter processing step. The raw image data coming from the FPI is typically encoded using $d = 12$ or 14 bits per pixel. However, it proved sufficient to process the images at 8-bit depth. Therefore, the bitdepth was typically reduced to 8 bits as this provides an efficient method of data reduction.

3.1.2.3 Top-hat filtering

In the next step, a morphological top-hat filtering procedure was performed in order to remove image background while preserving image signal at the transponder locations [46]. In morphological image processing, a structuring element g is applied to an image h in a way defined by the respective operation (for details see for example Gonzalez and Woods [51]). To understand the top-hat filtering procedure implemented in the present work, a comprehension of the morphological operations of erosion and dilation on grayscale images is required. In order to erode a grayscale image, at every position in the image the *minimum* value of the values inside a pixel neighborhood (defined by the structuring element) is placed at the position of the origin of the neighborhood in the eroded image. The structuring element g can have an arbitrary shape depending on the desired filter effect. In this work, squared shapes of g were used because they are separable in a way that enables a highly efficient implementation described below. (The name top-hat filter alludes to circular shapes of g that were used traditionally.) Dilation is the operation in which the *maximum* value found in g is transferred to the destination pixel.
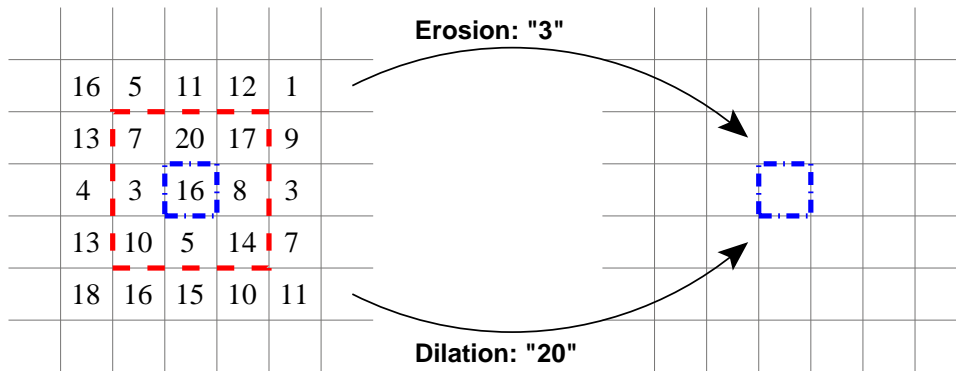

Figure 3.3: *Morphological operations* Erosion *and* Dilation *illustrated on a section of a grayscale input image (left) and an output image (right). A squared* 3×3 *structuring element g (red dashed box) is used whose origin is its center pixel (blue dash-dotted box.) Erosion assigns the minimum value found within the structuring element to the target pixel; dilation the maximum.*

An illustration of these basic operations of grayscale morphology is given in Figure 3.3.

From the illustration, it can readily be understood that different shapes of g, or even just different positions of the origin within g, can be used to achieve different filter results. Erosion and dilation on grayscale images belong to the same group of rank-order (and hence nonlinear) filter operations as the median filter: erosion selects the pixel with rank 0; median the one with rank 0.5; dilation the one with rank 1. The notation and the combination of operations leading up to the top-hat filtered image D are as follows

$$\text{Erosion:} \quad h \ominus g \tag{3.4}$$

$$\text{Dilation:} \quad h \oplus g \tag{3.5}$$

$$\text{Opening:} \quad h \circ g \quad = (h \ominus g) \oplus g \tag{3.6}$$

$$\text{Closing:} \quad h \bullet g \quad = (h \oplus g) \ominus g \tag{3.7}$$

$$\text{Top-hat filter:} \quad f \quad = h - (h \circ g). \tag{3.8}$$

A simple test case has been devised to visualize the function of the top-hat filter. Figure 3.4a shows the original test image that features objects of different sizes and shapes on some structured image background. A number of assumptions about the transponder tracking application underlies the test image. First, the transponders can have elliptical or spherical projections depending on the projection angle. Secondly, the
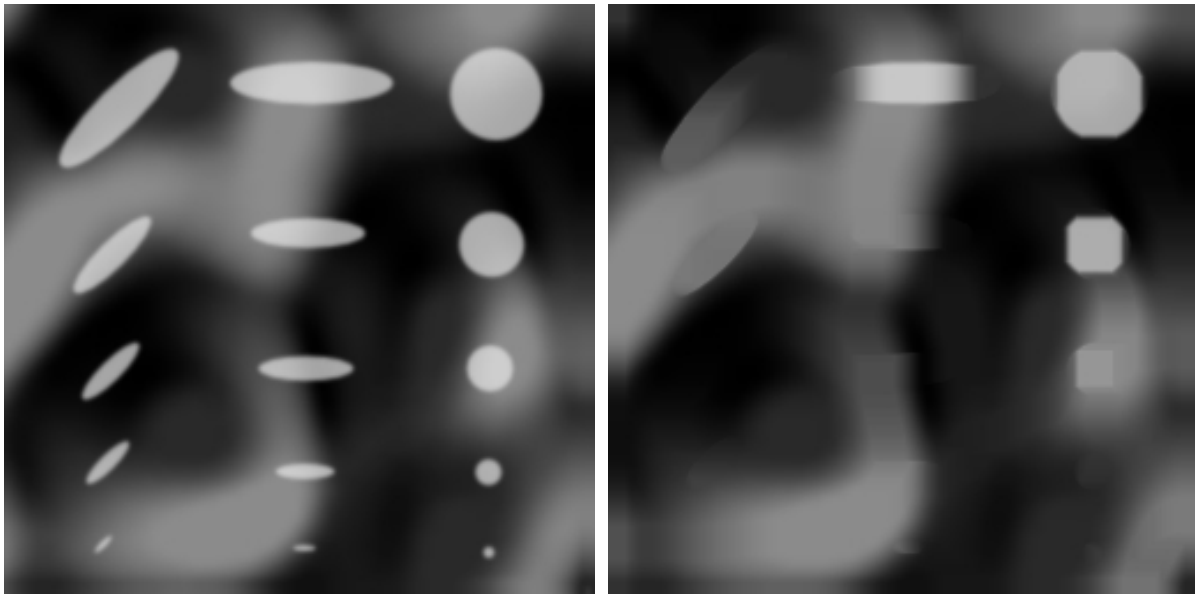
(a) Original test image   (b) Morphologically opened test image

Figure 3.4: *Test image to evaluate the function of the top-hat filter in (a). The result of the intermediate opening step is shown in (b).*

transponders should be the smallest high-contrast objects in the images. Features of the image background (bones, patient positioning equipment, table structures) should cause

slow gray-value variations compared to the small transponders. Thirdly, the gray-level intensity of the transponders can vary depending on image background. Finally, the elliptical projections of the transponders can have different orientations. The dimension of the test image was 256×256 pixels and a 15×15 pixels structuring element g was used whose origin was the central pixel. An intermediate result after opening the original image according to Equation 3.6 is shown in Figure 3.4b. It can be observed that the opening operation removes objects smaller than a certain size (dependent on the size of g) which makes it suitable for noise removal in some circumstances.

The final step of the top-hat filter operation (Equation 3.8) is the subtraction of the opened image from the original image. The result is shown in Figure 3.5. The subtraction
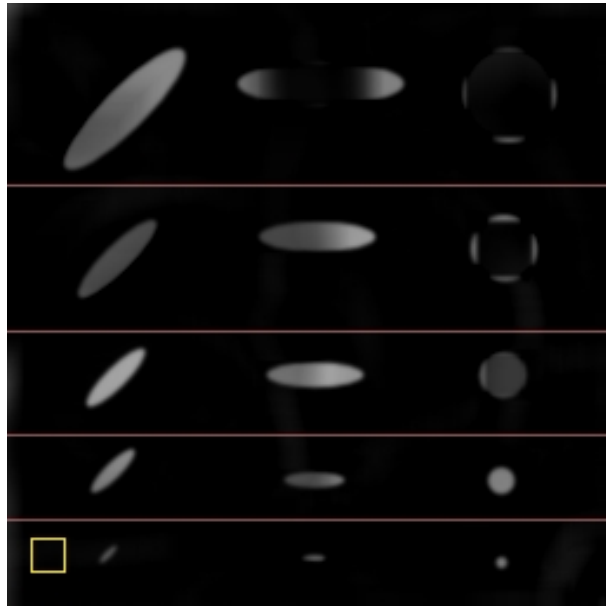

Figure 3.5: *Result of the top-hat filter operation obtained by subtracting the opened image from the original image. Horizontal lines are drawn for orientation. The square at the bottom left shows the 15×15 pixels structuring element used.*

successfully removed the image background thus displaying the remaining objects on a uniform black background, which would permit the threshold-based segmentation of the remaining objects. Which objects are preserved by the filter operation depends on the shape and the size of the structuring element. Figure 3.5 shows that the squared structuring element g favors elliptical objects whose long axis aligns with the diagonal of g: the objects in the left columns are preserved up to the largest size. Horizontal elliptical objects are well preserved as well. Circular objects appear to be removed from the image at smaller sizes (area-wise) than the elliptical test objects. However, if the objects were projections of real transponders, corresponding projections would be, e. g., the elliptical projections of row #3 (counted from the bottom of Figure 3.5) and the circular projection of row #2. Hence, this test indicated that an appropriately sized squared structuring element can be used to remove image background while preserving the transponder projections.

The morphological filtering can easily become the bottleneck in terms of speed of the entire TTA. A "back-of-the-envelope" calculation using intercept theorems reveals that under the given geometric conditions, projections of the transponders' long axes would span between 20 and 30 pixels. Based on Figure 3.5, the optimal squared structuring element would roughly be half the size of the transponders' long axes, i.e. 15 pixels for example. A brute force implementation of the top-hat filter would thus require $15 \times 15 = 225$ comparisons per output pixel, which is not efficient. The strategies for efficient morphological filtering revolve around clever decomposition of the structuring element. One strategy is to decompose arbitrarily shaped structuring elements into sets of small structuring elements of the same dimension (e.g. 2D→2D) that, applied in combination, give the same result as the original structuring element but require less comparisons. This approach is implemented for example in the Matlab image processing toolbox; its advantage is that it is applicable to many different shapes of structuring elements. However, if restriction to squared structuring elements is possible, the "van Herk-algorithm" is much more efficient [52]. His strategy was to separate a squared structuring element into two linear 1D structuring elements and to use recursive sorting to construct two temporary vectors. The linear structuring elements are applied to the rows and to the columns of the image separately. For the line-wise processing, one comparison per pixel is required for the construction of each temporary vector plus one comparison to pick the output pixel from the temporary vectors: three pixel comparisons per output pixel *independent of the size of the original squared structuring element.* Combination of the line-wise and column-wise filtering doubles the number of comparisons per output pixel to six. Even if there is some overhead resulting from the management of the temporary arrays, the "van Herk-algorithm" achieves speed improvements of the top-hat filtering by large factors compared to a brute force implementation. Hence, this algorithm was used in the present work.

3.1.2.4 Binary image processing

The last step of the TTA consits of a binary image processing loop as depicted in Figure 3.1. Here, the top-hat filtered image is converted to a binary image in which connected groups of pixels with value 1, so called *components*, exist at the locations of the transponders (and possibly at spurious locations as well). The binary threshold is determined iteratively and applied always to the original top-hat filtered image. The iteration loop performs the following steps: (1) The pixel gray-values in the image are cast to floating point numbers and scaled to range from 0 to 1. (2) For the first iteration, the threshold is initialized to $T_1 = 0.5$. (3) The components in the resulting binary image are first labeled, then analyzed and finally the components that passed analysis are considered to correspond to transponders and are counted (n). (4) If more or less than the

expected number of Beacon transponders (K) remain in the image, the new threshold T_i in iteration i will be the previous threshold T_{i-1} plus or minus 2^{-i}, respectively. It was found empirically that it suffices to refine T at most ten times. If then n still differs from K, the TTA terminates and outputs the locations of a number of transponders that is smaller than K. Hence the two possible outcomes of the TTA depicted in Figure 3.1.

Moments-based binary component analysis Component analysis can be understood as a cleanup procedure after the application of a global threshold to the ROI. Thresholding may produce a whole set of components of which a maximum of K (usually $K = 3$) will correspond to transponders; other components may correspond to image noise or image features that escaped top-hat filtration. The idea was to efficiently apply a set of criteria to each component in order to distinguish real transponder components from spurious components. Therefore, a shape analysis based on geometric moments was implemented because moments can be computed efficiently and a number of shape descriptors can be calculated based on the low-order moments [53, chpt 18.3]. In analogy to mechanical moments, moments in image processing are a set of metrics describing a mass (i. e. *components* in the present case) at some distance from a reference point or axis. The general formulation to compute the $(p + q)$ th-order moments of a discrete 2D image function is

$$m_{pq} = \sum_{u=1}^{N} \sum_{v=1}^{M} u^p v^q g\left(u, v\right), \tag{3.9}$$

where g is a $N \times M$-sized binary image containing one single component[2], p and q are integer values equal to or greater than zero and m denotes the geometric moment. Immediately, the first shape feature can be derived: the zeroth-order moment m_{00} is the *area* of the component in g. Next, from the first-order moments, the *center of mass* of the component (u_0, v_0) can be calculated as follows

$$u_0 = \frac{m_{10}}{m_{00}}, \quad v_0 = \frac{m_{01}}{m_{00}}. \tag{3.10}$$

If the component was accepted as a transponder, its center of mass coordinates can readily be converted into the position of the transponder in the entire x-ray image. It is convenient to express the higher order moments in a translation invariant manner by using (u_0, v_0) as the reference point. These moments are called the central moments μ

---

[2]To process the individual components, the Matlab image processing toolbox provides a set of convenient functions. In the C code implementation, functions of the Leptonica image processing library [54, leptonica.com] were used for efficient component management.

and are calculated as

$$\mu_{pq} = \sum_{u=1}^{N} \sum_{v=1}^{M} (u - u_0)^p (v - v_0)^q g(u, v).$$ (3.11)

Based on the second-order moments, the component ellipse can be expressed in terms of the lengths of its semi-major and semi-minor axes a and b, respectively, as [55]

$$a = \left(\frac{2 \left[\mu_{20} + \mu_{02} + \sqrt{(\mu_{20} - \mu_{02})^2 + 4\mu_{11}^2} \right]}{\mu_{00}} \right)^{1/2}$$ (3.12)

$$b = \left(\frac{2 \left[\mu_{20} + \mu_{02} - \sqrt{(\mu_{20} - \mu_{02})^2 + 4\mu_{11}^2} \right]}{\mu_{00}} \right)^{1/2}.$$ (3.13)

The component ellipse has the same area and second moments as the component itself and its angle with respect to the image axes can also be calculated from the moments [55]; the angle was not exploited here. Due to the transponder projections being good approximations of ellipses, the component ellipse proved to be a powerful descriptor for the shape analysis. As such, a and b can be interpreted as *the length and the width* of a transponder projection. Furthermore, the *eccentricity e* of the ellipse is a good descriptor of a transponder projection and it can be calculated as follows

$$e = \sqrt{1 - \left(\frac{b}{a} \right)^2}.$$ (3.14)

For an efficient calculation of the geometric moments, the algorithm proposed by Yang and Albregtsen [56] was used. In their approach, only the contour of the component needs to be determined. The moments of binary components can then be calculated entirely from the contour. A clever contour delineation method is the basis of their approach, which as by-products provides the components *perimeter* and *bounding box*; two more descriptors for shape analysis. A summary of the shape descriptors used in the component analysis is given in Table 3.1 together with the means of determination. It is important that the shape analysis is able to faithfully detect both extremes of the range of shapes that the transponder projections can adopt. The two extremes are, depending on the projection angle, elliptical disk and circular disk. Due to the elliptical shape still being "fairly round" (theoretically the lowest eccentricity is still ~0.97), a small range of parameters for the descriptors of Table 3.1 can be found that allow detection of transponder projections independent of the angle of projection. Other conceivable features that would strengthen the component analysis include component

Table 3.1: *Shape descriptors used in the component analysis in order to detect transponders in binary images and to discard spurious objects. The means to determine the values of the descriptors are given in the second column and one set of parameter ranges typically used in the present work in the third column.*

Shape descriptors	Determination	Typical values in pixels
Area	m_{00}, Eqn. 3.9	20–150
Perimeter	contour follower from Yang and Albregtsen [56]	12–60
Bounding box (side length)	contour follower from Yang and Albregtsen [56]	7–50
Ellipse: long axis	Eqns. 3.12 and 3.13	10–40
Ellipse: eccentricity	Eqn. 3.14	>0.97

solidity or, more generally, the configuration of the transponders in space. The former cannot be calculated trivially based on geometric moments and the latter in fact should be implemented if reliability of the TTA needs to be improved. Component analysis was found to be a crucial step of the TTA as it effectively discards spurious components thereby providing robustness of the TTA in noisy or low-contrast image situations.

3.1.3 Systems synchronization

The methods to synchronize x-ray imaging with EM tracking developed in this work will be presented. First, the problems with asynchronous operations will be introduced in order to motivate the synchronization. Secondly, the development of an electronic synchronization interface will be reviewed and, lastly, the methods used to validate the synchronization will be introduced.

3.1.3.1 Asynchronous operation

In the course of the present work it was discovered that asynchronous, simultaneous operation of the Calypso System and the FPI caused streaking artifacts in the x-ray images. Two examples are shown in Figure 3.6. Figure 3.6a is a projection image acquired using the kV x-ray imaging option of the prototype ARTISTE Linac. The image is one frame out of a set of raw CBCT data. The vertical grid lines are image artifacts. Any 3D CBCT dataset reconstructed from such projections is rendered unusable and contains only noise. Figure 3.6b is from a completely different dataset. It shows a transversal slice of a 3D MV CBCT dataset of the body phantom (Section 2.3.1) acquired using the MVision imaging option of a clinical ARTISTE Linac. The streaking artifacts in the
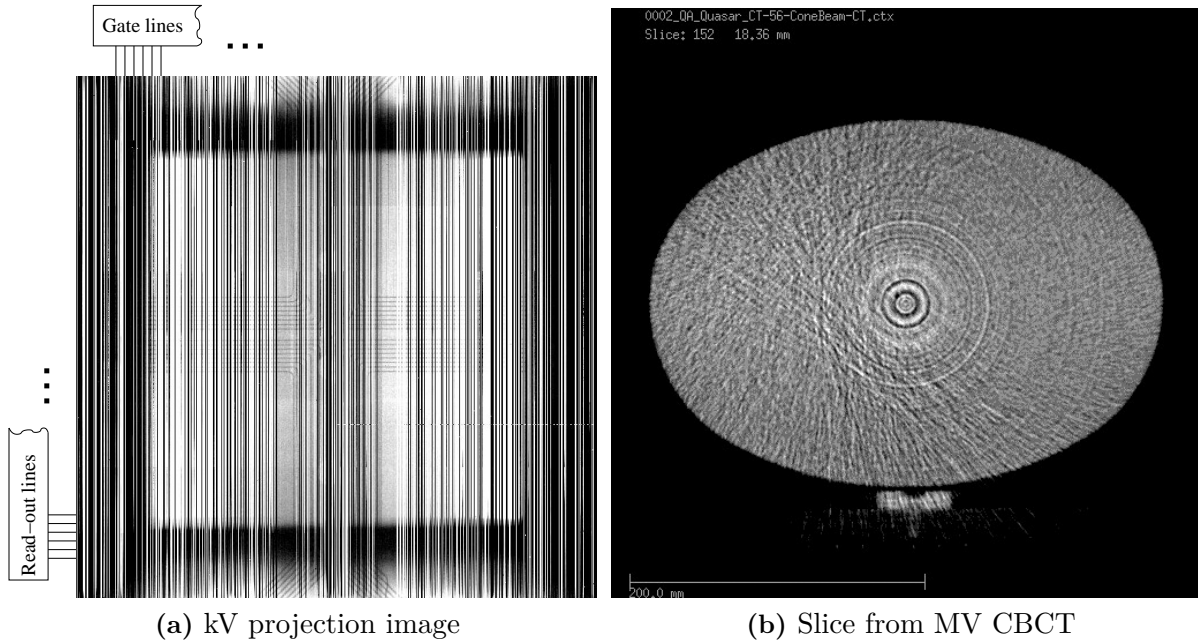
(a) kV projection image

(b) Slice from MV CBCT

Figure 3.6: *Examples of artifacts encountered in x-ray images acquired during asynchronous, concurrent EM tracking.*

raw projection data were less severe such that the reconstructed CBCT dataset shows at least the general shape of the imaged object. Nonetheless, the transversal slice in Figure 3.6b is affected by highly visible ring artifacts and oblique streaks. Assessment of anatomy, particularly around the centrally located isocenter, seems impossible. It was verified that the artifacts were in fact due to simultaneous, asynchronous operation of the EM tracking system rather than a malfunction of the imaging equipment or of the CBCT reconstruction.

In general, the artifacts manifested themselves as one-dimensional noise or line artifacts. Digital FPIs consist of a grid of conductive lines that form an *active matrix* for signal collection and read-out (for details see Rowlands and Yorkston [57]). The line artifacts in Figure 3.6a coincide with the arrangement of so called gate lines and read-out lines that form the active matrix. The noise effect of the artifacts occurred along the direction of the detector read-out lines, which indicated that the effect of EM emission from the Calypso magnetic array on the electric potential of the gate lines is responsible for the artifacts.

The following was observed: (i) The severity of the artifacts showed an inverse correlation with the separation of the FPI from the Calypso magnetic array. The separation (normal to the FPI) can get as small as $\sim 10\,\mathrm{cm}$ in the imaging geometry illustrated in Figure 2.11. (ii) The severity of the artifacts was greater in kV x-ray images than in MV x-ray images. This may be due to both the higher gain of the kV detector com-

pared to the MV detector and the larger radial distance of the MV detector from the isocenter (45 cm) compared to the kV detector (38 cm). (iii) Occasionally, the artifacts affected only parts of the image. The patterns of the partial effects reflected the image read-out scheme of the detector circuitry. It was hypothesized that the spatial extent of the artifacts correlated with the time overlap between image acquisition and pulsed EM emission from the EM tracking system. To test the plausibility of this hypothesis,
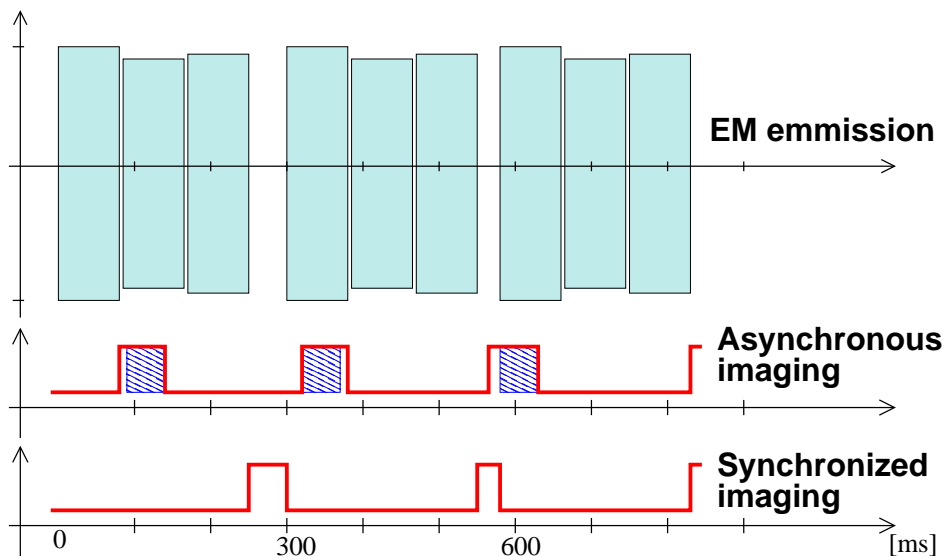
Figure 3.7: *Schematic drawing of the measured EM duty cycle of the EM tracking system (top diagram). Below, both the standard asynchronous and the proposed synchronized imaging schemes are illustrated. Blue shaded areas under the imaging pulses indicate overlap of image acquisition and EM emission.*

the duty cycle of EM emission from the Calypso System was measured. The result is illustrated in the top diagram of Figure 3.7. EM emission occurs in triplets with short periods of EM silence between emissions within a triplet and longer periods of EM silence between triplets. It is then plausible that different degrees of overlap (blue shaded areas in the figure) between image acquisitions could lead to the variable extent of the artifacts in the images. In the following, the realization of a synchronization scheme is presented that, as illustrated in the bottom diagram of Figure 3.7, would acquire x-ray images only in the periods of longer EM silence thus providing artifact-free x-ray images.

3.1.3.2 Synchronization circuit

A uni-directional synchronization circuit was developed that monitors the EM duty cycle of the Calypso System and triggers x-ray image acquisition with the FPI whenever the Calypso System is in a cycle of EM silence. A solenoidal pickup coil ($\sim 12\,\mu$H) served as the sensor for the oscillating EM emissions. It was positioned 11 cm above the sur-

face of the Calypso magnetic array. The pickup coil consisted of loops of copper wire wound around plastic tubing. The signal from the pickup coil was processed by the synchronization circuit.

The synchronization circuit was first simulated using Spice[3] (OrCAD PSpice 9.1 Student Version) and subsequently realized as a prototype. The circuit worked by feeding the signal coming from the pickup coil into a noise-discriminating voltage comparator (`lm111` in Figure 3.8). Noise discrimination was achieved through hysteresis at the comparator
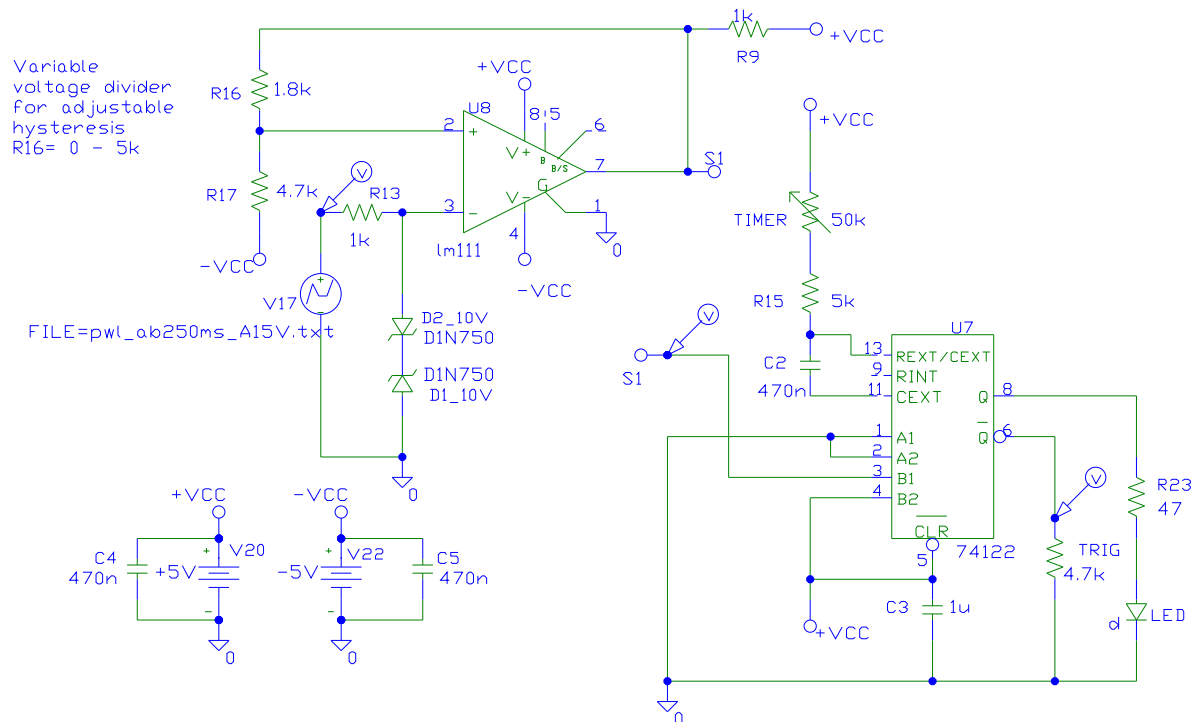
Figure 3.8: *Design of the synchronization circuit developed to process incoming signals (`V17`) from the EM pickup coil and to generate TTL pulses that trigger x-ray image acquisition (`TRIG`).*

input (`lm111, pin 2`), i. e. the reference voltage is at some level for rising slopes of the test voltage and at the inverse level for falling slopes. In practice, the signal strength measured by the pickup coil varies between EM targets because the orientation of the AC magnetic fields emitted by the Calypso magnetic array will adapt to the orientation of the transponders so as to maximize energy transfer to the transponders. However, the pickup coil consistently provided signals $> 5\,\mathrm{V}$ and the signal noise was below $1\,\mathrm{V}$ such that reference voltages of $\pm 2\,\mathrm{V}$ could be used at the comparator. Two Zener diodes (`D1N750`) were used to clip incoming signals greater than $\pm 10\,\mathrm{V}$. Voltage peaks that occur transiently at the pickup coil could otherwise damage the synchronization circuit.

---

[3]<u>S</u>imulation <u>P</u>rogram with <u>I</u>ntegrated <u>C</u>ircuit <u>E</u>mphasis

The comparator then sends out a train of transistor-transistor-logic (TTL) pulses while the pickup coil is in the oscillating magnetic field of the Calypso magnetic array. The pulses from the comparator feed into a re-triggerable, mono-stable, low-active flip-flop circuit (`74122` in Figure 3.8). As long as pulses arrive at the flip-flop circuit, it is held down (i. e. in its OFF state; the `LED` will light up during the OFF state). When no more pulses arrive (i. e. Calypso cycle of EM silence) within a time window longer than a configurable time t_{void}, the flip-flop circuit will go into an active ON state by sending out a TTL pulse (`TRIG` in Figure 3.8). The time window t_{void} is used to discriminate between short and long EM silences in the Calypso System's duty cycle; t_{void} is adjusted using the potentiometer labeled `TIMER` in the circuit design. The TTL pulses generated at the TRIG output of the circuit could be used to control x-ray image acquisition using the system developed by Tücking [23].

3.1.4 Imaging with concurrent EM tracking

Applying the synchronization scheme developed above, image-based target tracking with concurrent EM target tracking should become feasible. In order to test the feasibility of concurrency, the tumor inside the thorax phantom (Section 2.3.3) was imaged and simultaneously tracked using the Calypso System. Three aspects of the combination of imaging with EM tracking could be evaluated using this experimental setup:

1. feasibility of artifact-free x-ray imaging with concurrent EM tracking,

2. performance of the target-tracking image processing algorithm and

3. comparison of image-based with EM-tracking-based transponder localization.

The thorax phantom was aligned with the room isocenter and imaged using a kV fluoroscopy acquisition scheme. A range of breathing motion patterns was used for evaluation. The parameters of the simulated breathing motion are listed in Table 3.2. The ampli-

Table 3.2: *Parameters of the simulated breathing motion.*

Amplitude of breathing motion	$1\,cm$, $2.5\,cm$, $5\,cm$
Cycle time of breathing motion	3–6 s
Quality of motion	$\cos^4$-type, "coughing"

tudes of breathing motion were chosen to represent average and maximum amplitudes of expected lung tumor motion. In addition to idealized $\cos^4$-type breathing curves, the phantom was programmed to perform asymmetric motion with high values of acceleration and deceleration on the exhale slope. This feature mimicked more irregular breathing patterns as they may be encountered during coughing, for example.

3.2 Results

3.2.1 Transponder detectability in x-ray images

3.2.1.1 MV x-ray projection images

Figure 3.9 show an anterior-posterior (AP) and a lateral x-ray projection image of the body-phantom. Both images were acquired using the un-collimated MV therapy beam and the MV FPI (shown in Figure 2.5a), i.e. the images are *portal images*. The FPI produces grayscale intensity images of 16 bit bitdepth, which means that each pixel can adopt values between 0 (black) and 65535 (white). Both images in Figure 3.9 only show a 5500 digits wide window of the full range of pixel values centered around the values 62000 (Figure 3.9a) and 47000 (Figure 3.9b) and stretched linearly into an 8-bit range. In other words, the dynamic range was manually adjusted to optimize the visibility of the transponders. With these adjustments, the transponders become faintly visible at the locations pointed at by the arrows in the figure. The objects in the center of the image represent the steel spheres embedded in the phantom or stuck to the phantom's surface.

(a) AP projection
(b) lateral projection
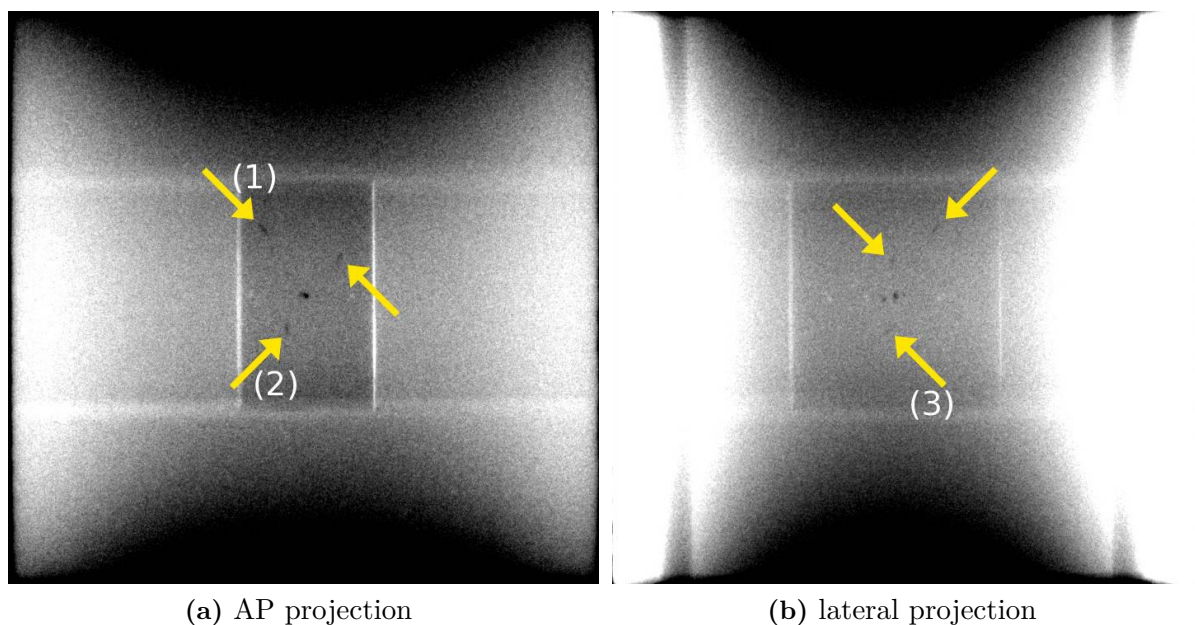
Figure 3.9: *Portal images of the body-phantom (see Figure 2.8). A 6 MV photon beam was used for imaging. The images are contrast-enhanced in order to visualize the implanted electromagnetic transponders at the locations pointed at by the arrows. The rectangular shape in the image center represents the Plexiglas insert that holds the transponders inside the phantom.*

Transponder visibility is qualitatively better in the AP projection image compared to the lateral projection. This results from an increased scatter fraction in the lateral

projection due to the increased absorber thickness in the lateral direction. One common metric for quantifying visibility is provided by the Rose model[58, 59]. The Rose model[4] states that object visibility, ν, chiefly depends on object contrast, image noise and object size. The model can be formulated as

$$\nu = \frac{S_o - S_{bg}}{\sigma} \cdot \sqrt{n_o}, \tag{3.15}$$

where ν characterizes object visibility, S_o is the mean signal intensities in the object, S_{bg} in the background, σ is the standard deviation of the noise, assumed equal in object and background, and n_o is the number of pixels belonging to the object. Applying Eqn. 3.15 to three of the transponder projections (marked by (1) to (3) in Figure 3.9), yields visibility values of $\nu_{(1)} = 19.8$, $\nu_{(2)} = 14.4$ and $\nu_{(3)} = 4.4$. Given that the Rose model empirically declares an object to be detectable for values of $\nu > 5$, the calculated values $\nu_{(1)-(3)}$ agree well with the visual observation. It can be stated that in this phantom experiment, some of the transponder projections are invisible, i. e. automatic transponder detection algorithms based on MV portal images of patients will be hard to realize. This holds particularly true since the situation in real patients is expected to worsen due to inhomogeneous object background (bones, soft tissue).

Figure 3.10a shows nine portal-during images that, if superimposed on top of each other, form the modulated fluence map shown in the center of the figure. It is important to note that the individual segments are scaled down in size and loosely positioned in Figure 3.10a for illustration purposes. The reader may imagine that the properly aligned superposition of the field segments #1 to #9 results in the fluence map shown in the center. The resulting fluence map can then be used for treatment verification. Figure 3.10b then shows a high contrast version of segment #5. In order to visualize the transponders, approximately the highest 7% of the 16 bit bitdepth range (values $[61000 \ldots 65535]$) were stretched to 100% of the range. With this contrast enhancement, the two transponders that are located inside the segment become barely visible ($\nu < 10$). However, the reliable automatic detection of the transponders in portals-during acquired during treatment of a real patient is expected to be challenging.

3.2.1.2 MV cone-beam computed tomography

Figure 3.11 shows an example of the level of visibility of the transponders in MV CBCT image data. The data in Figure 3.11 was acquired with the cone beam collimated to ± 5 cm in the y-direction (see IEC CRF in Figure 2.7), i. e. along the patient's long axis. This collimation corresponds to scanning only the central slab of phantom material (cf.

---

[4]Strictly speaking, the Rose model applies only within certain constraints, e. g. un-correlated image noise. As used above, it assumes the detector pixel values to be the result of perfect photon counting, which somewhat over-simplifies the situation.
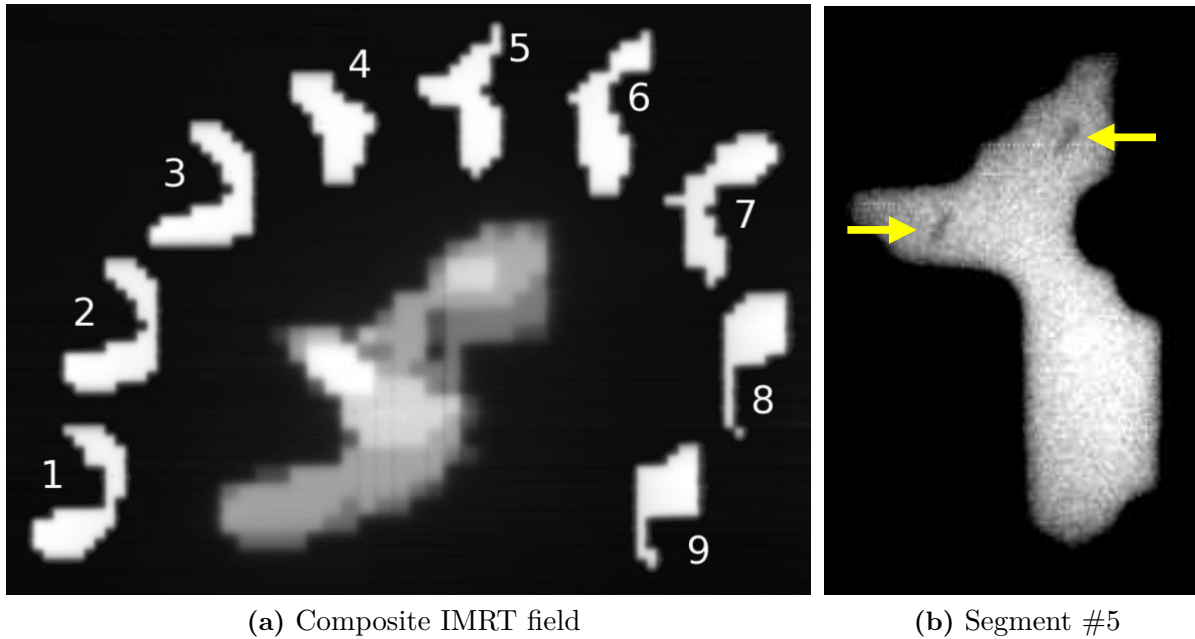
(a) Composite IMRT field   (b) Segment #5

Figure 3.10: Portal-during *images produced by the ARTISTE MV imaging equipment which—by superposition—result in the nine-segments IMRT field (center image in (a)) delivered to the body-phantom (Figure 2.8). Transponders are barely visible (indicated by arrows) in a high contrast version of the image of segment #5 in (b).*

body-phantom in Figure 2.8) in which the transponders were located. In practice, collimating the cone in z-direction as much as possible is desirable to keep the fraction of scattered radiation in the image at a minimum and, hence, to maximize image quality. The permissible amount of pre-collimation is determined by FOV requirements. Collimation in y-direction means restricting the number of transversal slices available in the reconstructed data set while collimation in x- or z-direction would result in a reduced transversal FOV, which is usually undesirable.

The images in Figure 3.11 display a range of Hounsfield units from 0 to 800, which was chosen to show water equivalent phantom material at the lower end of the range and the metallic transponders at the upper end. The transponders inside the body-phantom are visible as white spots on top of the noise background (Rose's model values of $\nu > 25$). Owing to the high energy beam quality, no metal imaging artifacts arise from the transponders. The phantom experiment indicates that MV CBCT imaging of a patient with implanted transponders just prior to a treatment fraction may be useful for the standard position verification (based on bony structure alignment) and also for the verification of the transponder locations. However, it is expected that transponder visibility may be worse in a real patient due to a more inhomogeneous image background and due to organ motion occurring during imaging (intra-imaging). Finally, these re-
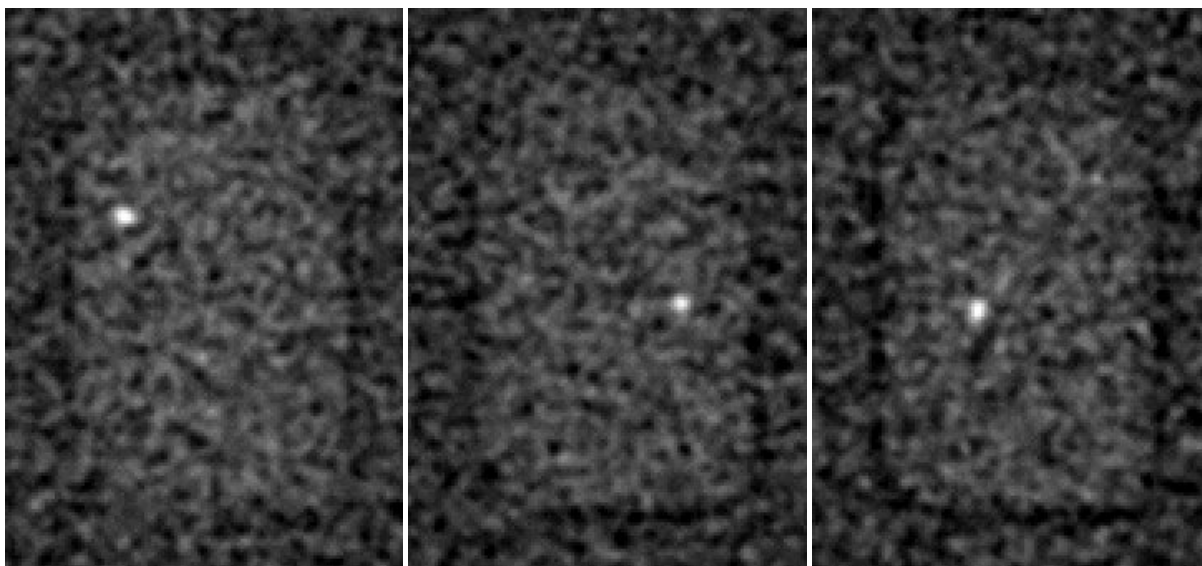
Figure 3.11: *Appearance of the three transponders in MV CBCT image data. The images are sections of different transversal slices from the same data set. Image data was acquired using* 10 *monitor units of radiation corresponding to a dose of* $\sim 0.1\ Gy$ *to the isocenter.*

sults apply to the specific imaging components. Future technology updates may lead to different results.

3.2.2 Transponder-tracking image processing

The transponder-tracking image processing algorithm was tested using the thorax phantom as a mobile target and the kV imaging equipment of the ARTISTE Linac. The clinical scenario simulated in this test environment is that of monitoring lung tumor motion using kV x-ray fluoroscopy and implanted fiducials. Using gold seeds as fiducials, this strategy has provided valuable insight into the mechanics of breathing and lung tumor motion at the expense of considerable imaging dose [30, 60]. Using the EM beacon transponders as fiducials is a superior approach because most of the time they could be tracked using the Calypso System. X-ray fluoroscopy only needs to be switched on if specific anatomical information is sought. Using this approach, lung tumor tracking could be performed routinely. Currently, the Calypso beacon transponders are not cleared for lung implantation, but research is underway and promising results have been published from a canine animal study [61].

3.2.2.1 Preparatory processing

The performance in terms of execution time of different median filter implementations was tested on x-ray images of four different sizes: 256×256, 512×512, 1024×1024 and 2048×2048 pixels. Additional noise was added to each image to challenge the median filters. Two median filters implemented in C code were compared to the medfilt2( ) function of the Matlab image processing toolbox. Both, in the C code and in the Matlab script only the execution of the median filters was timed in order to exclude the times needed by each program to handle (open, load, etc.) the images. The filter implementations were based on 3×3 and 3×4 (efficient implementation) filter kernels. The two filters implemented in C code were (a) a straight forward implementation of the median filter operation and (b) the implementation of an efficient median filter as described in Section 3.1.2.2. It was verified that each filter implementation produced the correct result. All three implementations were tested on the same computer hardware (Pentium 4, 3.4 GHz, 2 GB of RAM).
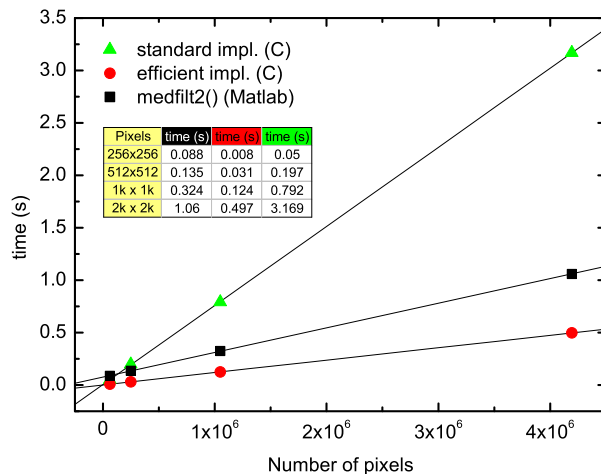
Figure 3.12: *Performance evaluation of different median filter implementations. Two filters were implemented as C code (triangles, circles) and one was the Matlab function medfilt2( ) (squares). Each filter implementation was tested on identical test images of four different sizes: 256×256, 512×512, 1024×1024 and 2048×2048 pixels. Linear fits of the data are shown for orientation. The datapoints are provided in table format for clarity purposes.*

Pixels	time (s)	time (s)	time (s)
256x256	0.088	0.008	0.05
512x512	0.135	0.031	0.197
1k x 1k	0.324	0.124	0.792
2k x 2k	1.06	0.497	3.169

Figure 3.12 shows the times required by each filter implementation. The x-axis shows the total number of pixels resulting from the squared images of the sizes mentioned in the figure caption. It can be seen that the increase in execution time as a function of the number of pixels is almost perfectly linear. The fact that the data obtained from the Matlab filter implementation has a certain time offset, i.e. would not go through the origin if extrapolated, hints towards an overhead of the Matlab scripting framework to call and execute a function such as medfilt2( ). It can further be seen that the standard implementation of the median filter becomes increasingly inefficient with large images. This performance test may serve as an indication that Matlab's functions are convenient to use and in general based on well optimized algorithms and code (medfilt2( ) seems to be based on Huang *et al.*[62]). However, if more effort is put into implementing highly

optimized algorithms using efficient C code, it will be faster than Matlab.

For the application in this work, filter performance in fairly small ROIs was most relevant, i. e. corresponding to image sizes between 256×256 and 512×512 pixels. For example, to median filter the test image of 256×256 pixels, it took the medfilt2( ) function 88 ms, the standard implementation 50 ms and the efficient implementation 8 ms.

The remaining steps of ROI preprocessing, namely linearization and contrast enhancement as outlined in Section 3.1.2.2, each require a simple gray-value transformation; simple in the sense that the transformation involves only the pixel of interest, i. e. a 1×1 neighborhood. Efficiency of the contrast enhancement step was achieved by recording the min–max values during the preceding processing steps, i. e. either in the course of median filtering or of linearization. An example of the result of preparatory processing can be viewed in Figure 3.13a. The grayscale convention in Figure 3.13a is such the image appears lighter in areas where fewer x rays impinged on the detector and darker in areas of higher x-ray signal. Two out of the three transponders in the example of Figure 3.13 are viewed in a projection orthogonal to their long axis; the transponder towards the bottom of the ROI is projected obliquely.

3.2.2.2 Top-hat filtering

Figure 3.13 illustrates the sequential outcome of processing steps of the TTA. The result of top-hat filtering the pre-processed ROI shown in Figure 3.13a can be viewed in Figure 3.13b. In this example a 15×15 pixels squared structuring element was used. The top-hat filtered ROI shows the three transponders clearly standing out on a dark background. Coarse background features present in Figure 3.13a were successfully removed by the top-hat filter. However, some finer background structure is still preserved. This occurs when background variations have a spatial extent that is comparable to or smaller than the structuring element. The level of preserved background structure shown in the example can be handled well by subsequent processing. In general, the successful operation of the top-hat filter mainly relies on two factors: (i) the transponders projections have a reasonable contrast in the input image and (ii) objects that resemble transponder projections are nonexistent in the ROI. The former was found to hold true in kV x-ray images of the phantoms used in this work and of patients as reported by others [31]. The latter can be ensured by keeping any small metallic objects such as steel BBs or screws out of the FOV of the x-ray image.

3.2.2.3 Binary image processing

Following top-hat filtering, the ROI is converted to a binary image by applying a global threshold to the top-hat filtered grayscale image. Depending on the threshold value,
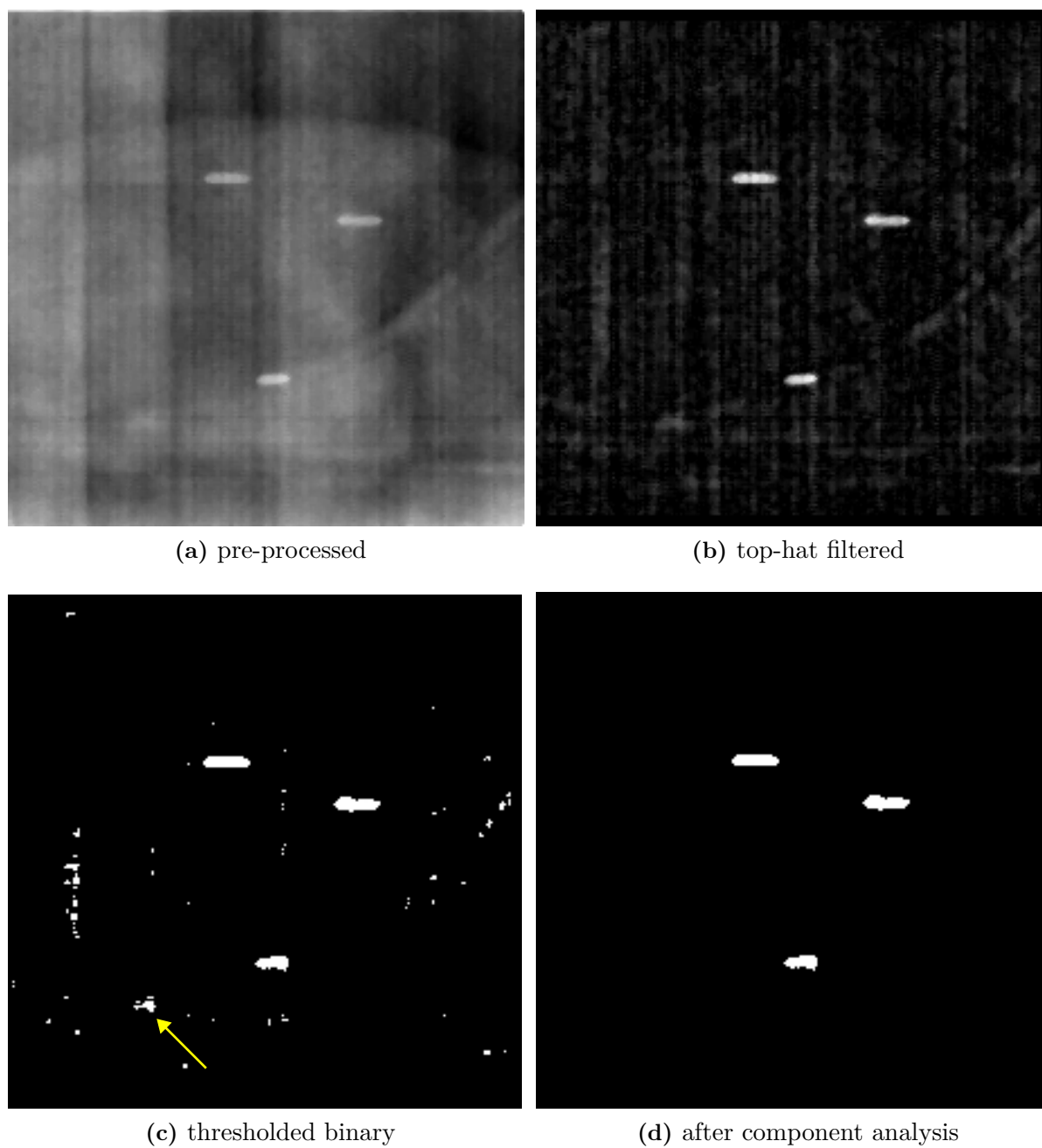
(a) pre-processed

(b) top-hat filtered

(c) thresholded binary

(d) after component analysis

Figure 3.13: *Results of intermediate processing steps of the transponder-tracking image processing algorithm (TTA). Shown is a 230×230 pixels region of interest (ROI) of one frame of a kV fluoroscopy sequence of the thorax phantom.*

61

the raw binary image can have the appearance of the image shown in Figure 3.13c. In this case, the binary image—apart from containing components at the transponder locations—contains spurious binary components; some of which consist of only one or very few pixels. Component analysis will start out by segregating each component into a separate sub-image. During this process, some components can readily be rejected based on their unrealistic spatial extent. The remaining components would undergo moments-based shape analysis as described in the Methods section 3.1.2.4 *(et seqq.)*. The typical ranges of parameter values given in Table 3.1 were applied. Shape analysis will reject most of the spurious components. However, one of the larger component indicated by the arrow in Figure 3.13c has the potential to escape shape analysis. If this was the case, a transponder count of four would result and a new threshold value, larger than the current one, would be tried. A larger threshold value would lead to less or thinner spurious components in the next iteration of the threshold adaptation loop (cf. Figure 3.1). Eventually, either a transponder-count of three is reached (Figure 3.13d) or ten iterations have been completed. Whichever happens first terminates transponder-tracking in the current ROI. If the TTA exits after completing ten iterations without reaching a transponder-count of three, the TTA outputs the locations of the $n < 3$ transponders that it managed to localize. The actual 2D image coordinates of the transponders reported by the TTA are the component centroids computed during binary shape analysis.

3.2.3 Systems synchronization

Figure 3.14 shows the realization of the prototype synchronization interface that was built according to the schematic of Figure 3.8. This prototype circuit could be strapped on to the handle of the Calypso array and wired up to three connections: (i) the green cable in the figure foreground connected to the pickup coil positioned above the Calypso magnetic array, (ii) the black-red-white cables in the background supplied power ($\pm 5\,\mathrm{V}$ and ground potential) and (iii) the trigger pulses for image acquisition were obtained from the resistor at the bottom of the magenta ellipse. It was found to be important that the supply voltages were precisely adjusted to within $0.1\,\mathrm{V}$ and that unintentional wire loops were avoided. The latter situation was avoided by twisting any loose cables (green and black-red-white cables in Figure 3.14).

The measured result of systems synchronization is shown in Figure 3.15. The top trace in the figure is the voltage signal coming from the pickup coil and feeding into the synchronization circuit. The bottom trace displays the TTL pulses that the synchronization circuit provided to the imaging control unit in response the the top trace. The top trace represents the Calypso System's EM duty cycle consisting of three blocks of sequential transponder localization followed by an intermediate cycle of EM silence. The Calypso duty cycle was artificially stretched during these experiments in order to extend the du-
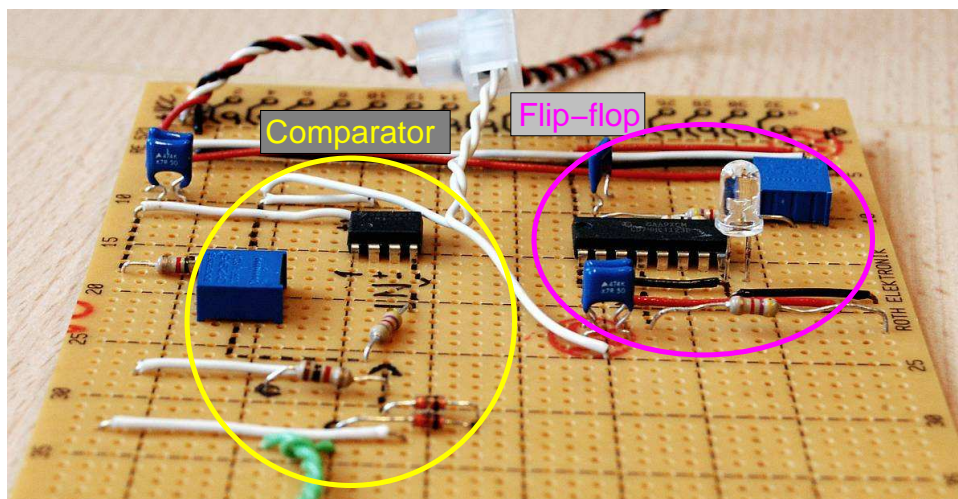
Figure 3.14: *Circuit to synchronize x-ray imaging with EM tracking. The circuit connects to a pickup coil that monitors pulsed EM emissions from the Calypso System. On the output side, the circuit triggers acquisition of x-ray images in cycles of EM silence.*

ration of the EM silence. This was necessary because the minimum image read-out time of the kV FPI was 66 ms and it was found that approximately 80 ms of EM silence were required to acquire an artifact-free x-ray image. One complete cycle of this synchronization scheme lasted ~450 ms (it is ~330 ms during normal operation of the Calypso System) during which three Calypso target updates occurred and one x-ray image was acquired. The reduced Calypso update rate was ~6 Hz. The x-ray image frame rate was ~2.2 fps. The time-limiting factor of this synchronization scheme was the kV image readout time. Newer generation FPIs come with minimum read-out times of ~30 ms, which would allow a Calypso update rate of 10 Hz and a kV frame rate of 3 fps.

3.2.4 Imaging with concurrent EM tracking

3.2.4.1 Artifact-free x-ray images: performance of TTA

Figure 3.16 shows results from tracking the radiation target inside the thorax phantom using the EM tracking system and kV x-ray fluoroscopy concurrently. The gantry was stationary during fluoroscopy. The fluoroscopy sequence was acquired using $7\,\mu$Gy of imaging dose per frame at the isocenter. The upper left panel of Figure 3.16 shows the projection of the lesion inside the thorax phantom with the three transponders implanted in the lesion. The three crosses denote the projected locations of the transponders at the time of planning. At the time of tracking, these previous locations were used by the TTA to compute an appropriately located and sized ROI in the x-ray images (cf. Section 3.1.2.1). The ROI in this case was the rectangle of high contrast in the x-ray
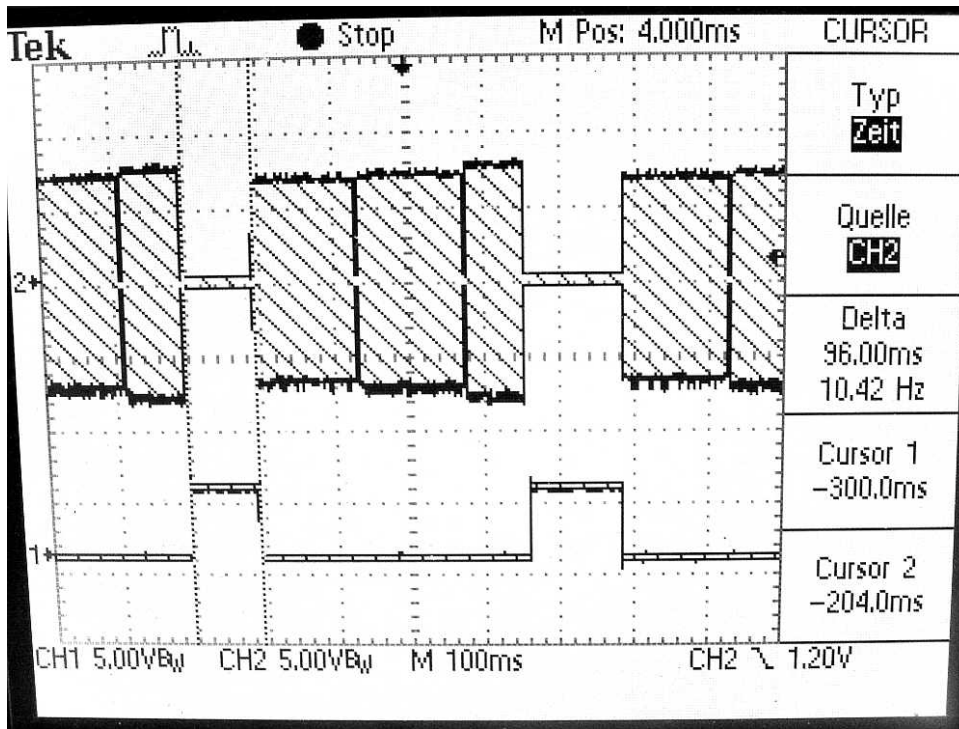
Figure 3.15: *Screenshot photographed off of an oscilloscope. The top trace shows the EM duty cycle of the Calypso System as sensed by the pickup coil. The bottom trace shows imaging pulses produced by the synchronization circuit (see Figure 3.14).*

image of Figure 3.16. The light squares in the image contain the current locations of the transponders at tracking time as determined by the TTA. The resulting x-ray target is shown as a dot within the transponder triangle. The x-ray target was defined as the two dimensional center of mass of the image coordinates of the three transponders projected to the isocenter plane.

The success rate of the TTA depends largely on the contrast-to-noise ratio (CNR) of the transponders in the x-ray images. The CNR is determined by the imaging dose and by the ratio of target velocity and x-ray pulse length. At the lowest imaging dose of 7μGy per frame at the isocenter, the detection rate was 100% in lateral projections but only ~15% in AP projections. This was due to the radiological pathlength for the imaging beam being longer in AP (table, phantom base plate) than in lateral direction. For the TTA to achieve a success rate of 90% in AP projections, an imaging dose of at least 30μGy was needed. The success rate was independent of target velocity in the range of velocities tested because, at worst, a transponder would move by 1 mm during the 10 ms long x-ray pulses, i.e. not enough to degrade CNR substantially. Processing time of the TTA was less than 100 ms for ROIs of less than 10^5 pixels which translates to a 9 cm$\times 9$ cm plane through the isocenter. Larger ROIs should not be necessary for image-based localization of the transponders.
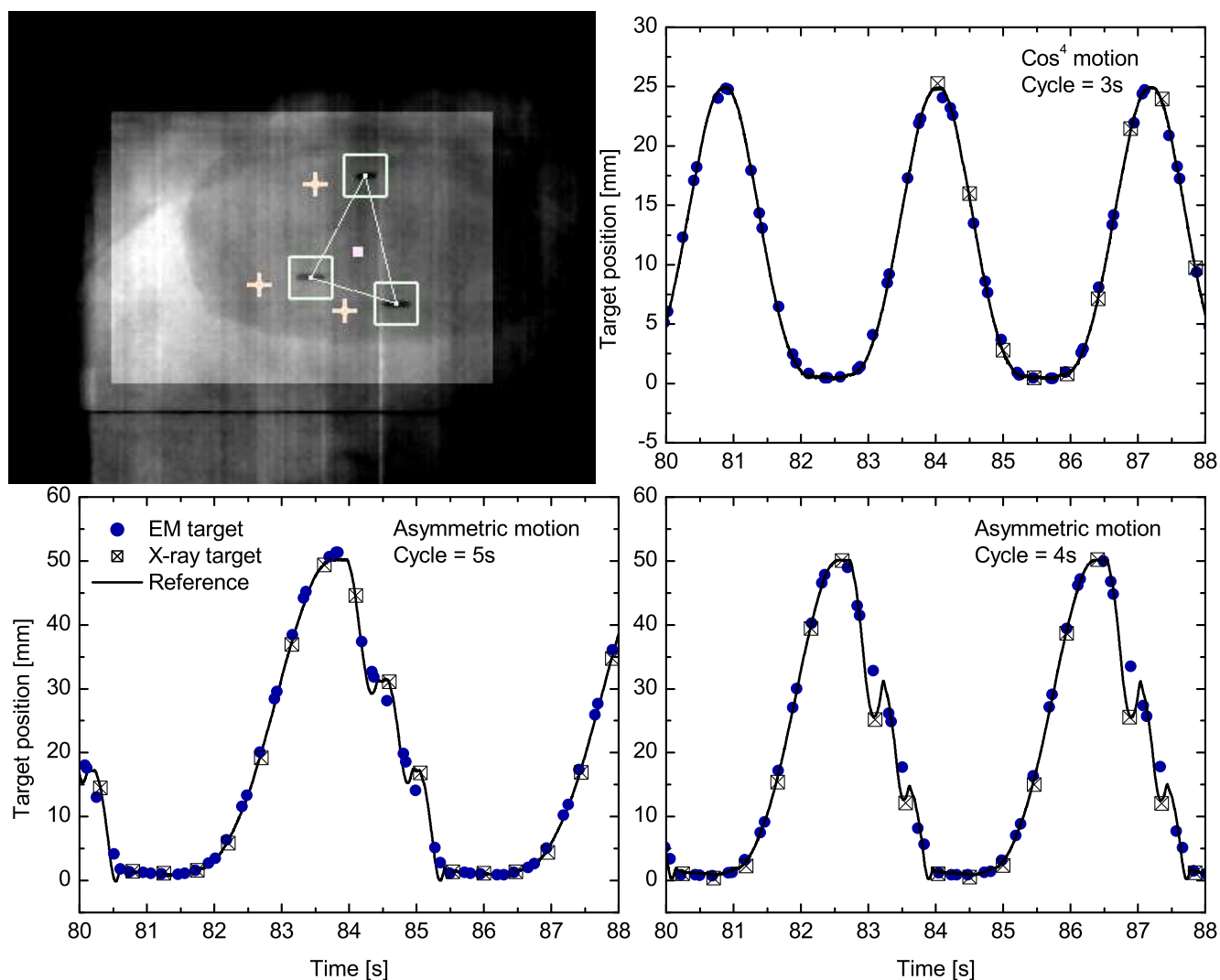
Figure 3.16: *Tracking of the target inside the thorax phantom using the EM system and kV imaging concurrently. Upper left panel: lateral x-ray projection through the thorax phantom with the rectangular ROI highlighted and showing the projection of the lesion. Other panes: three target motion patterns measured concurrently by the reference measurement (potentiometer), by transponder-tracking image processing (TTA) and by the EM tracking system.*

3.2.4.2 Comparison image-based with EM-based target tracking

The three diagrams in Figure 3.16 show motion curves obtained by programming the phantom to perform $\cos^4$-type and asymmetric motion with cycle times as indicated in the diagrams. Since the reference measurement was a differential signal, it was shifted along the ordinate of the graph to match the EM target signal—referred to as *signal shift* below. The data was not scaled to match. The two separate time axes—one of the EM tracking system and one of imaging and reference measurement—were uniquely registered using a method that will be presented in the context of 4D CBCT acquisition in Section 4.2.2. Thereby, the visual shift-to-match approach along the time axis, as necessary in the work of others [44], could be avoided.

The idealized $\cos^4$-type motion is reproduced very well both by x-ray image-based and EM target tracking even up to drastic breathing motion of 2.5 cm amplitude and a cycle time of 3 s. The lower panes of Figure 3.16 show the results of tracking asymmetric types of target motion with an amplitude of ~5 cm, a maximum target velocity of 11 cm/s, a maximum acceleration of the target of ~3 m/s² and abrupt changes in the direction of the motion. These were the most extreme types of breathing patterns tracked by both tracking modalities. In those cases, we observed that on the descending exhale slopes, the x-ray image-based tracking (i. e. the TTA) reproduced the true target position more accurately than the EM target tracking. Maximum deviations on the order of a few millimeters can be observed. This observation is explained by the fact that the TTA works exclusively in the current image's spatial domain whereas the EM tracking system effectively applies temporal averaging (by polling the three transponders sequentially) to obtain noise-reduced target localizations. Temporal averaging, while at the same time reproducing high frequency components of motion, constitutes a trade-off that becomes apparent in these measurements, firstly, because extreme motion curves were tested and secondly, because the Calypso System was operated at a reduced update rate. With a Calypso System optimized for tracking lung tumors, as opposed to the prostate, the system's dynamic performance can be expected to further improve substantially. These experiments were devised to determine the dynamic limits of the tracking modalities. In the clinic, it is unlikely that tracking a tumor with the treatment beam during coughing will be relevant (unless an intervention scheme is applied that interrupts the beam delivery).

3.2.4.3 Impact of target velocity on target tracking

In order to investigate the dependencies of image-based and EM target tracking on target velocity, the densely sampled reference measurements of $\cos^4$-type target motion were numerically differentiated in order to obtain the target velocities as functions of time. The

"coughing" motion curves (lower panels in Figure 3.16) were excluded from this analysis because the high target accelerations encountered here were unsuitable for obtaining robust velocity estimates. The extraction of target velocities from the motion curves is shown in Figure 3.17a. The velocity curve (lower diagram in Figure 3.17a) shows some degree of asymmetry indicating a mechanical imperfection of the phantom. Subsequently, the velocity curves were discretized into bins of a width of 0.5 cm/s as indicated by the horizontal grid lines in Figure 3.17a. The differences between all target localizations— both x-ray-based and EM-based—and the reference measurement were calculated and assigned to their corresponding velocity bin. In each velocity bin, the mean of these differences and the standard error of the mean were calculated. These are plotted as datapoints and errorbars, respectively, in Figure 3.17b.

(a) target velocity derivation   **(b)** dynamic comparability
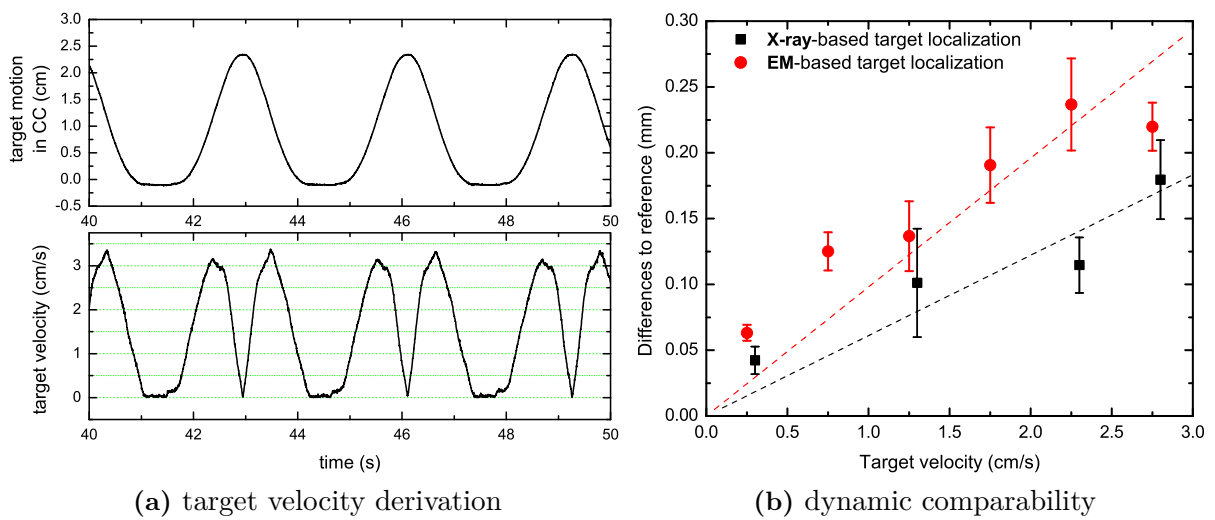
Figure 3.17: *(a) Derivation of target velocities (bottom diagram) from* $\cos^4$*-type target motion (top diagram). (b) Comparability between EM-based target position and reference measurement (red) and between x-ray-based target position and reference measurement; both presented as functions of target velocity.*

Figure 3.17b then shows the comparability of the target localizations with the reference measurement as functions of target velocity—the dynamic comparability. Only datapoints calculated from at least ten samples were included in the figure. Trend-lines through the origin are shown for orientation. The comparability shows a slight but steady degradation (increase of the difference) as the velocity increases. In the case of EM target tracking, the degradation of comparability is more pronounced and may be explained by the inherent mechanism of temporal averaging over transponder positions. In the case of x-ray image-based target localization, the degradation may be explained by smearing-out of transponder signal with increasing velocities and a resulting uncertainty in the localization of the transponders in the x-ray images. Overall however, a very good agreement

was observed: both target target tracking modalities were comparable to the reference measurement to within 0.25 mm up to target velocities of 3 cm/s. Hence, both tracking modalities are capable of accurately reproducing the clinically relevant features of breathing motion.

These values for the comparability between Calypso target localizations and some reference measurement agree well with published data. Santanam et al. [44] reported a RMS localization error of ≤ 0.33 mm for phantom motion up to 1 cm/s. Recently, Murphy et al. [63] presented a very elaborate investigation of the dynamic accuracy of the Calypso System and reported uncertainties of < 0.3 mm measured up to target velocities of 3 cm/s.

Summary

In this chapter, the detectability of EM transponders in MV x-ray images was investigated and it was found that they cannot be detected in reliably in 2D projection images but they are visible in 3D image datasets. Methods to synchronize image acquisition with EM target tracking and to localize transponders in kV x-ray projections images were presented. At the end of the chapter, lung tumor motion was tracked using EM- and image-based approaches concurrently thus demonstrating an advanced method for the clinical detection of intrafraction organ motion.

Chapter 4

Application to 4D cone-beam computed tomography (CBCT)

The Siemens ARTISTE Solution is designed to have both MV and kV imaging *onboard*, i. e. mounted to the Linac gantry. As explained previously (Section 2.2), these onboard imaging options can be used to acquire CBCT datasets. Taking this concept to the next level, a CBCT-capable imaging system in synchrony with a measurement of organ motion naturally leads to the acquisition of *4D CBCT* data; sometimes referred to as *motion-correlated*, *respiration-correlated* or *time-dependent* CBCT (potential differences between these alternative terminologies will be discussed in Section 6.2). Motion-correlation is necessary because the rotation time on CBCT systems mounted to Linac gantries is usually so long that substantial organ motion can occur during data acquisition. This makes images from these systems more prone to motion artifacts than those produced by dedicated helical CT scanners. The most prominent example is breathing motion, which completes a few cycles during a complete rotation of the gantry of a Linac ($\sim 1\,\mathrm{min}/360\,\mathrm{degrees}$) but only a small fraction of a cycle during the rotation of a dedicated CT scanner ($\sim 0.3\,\mathrm{s}/360\,\mathrm{degrees}$). Examples of artifacts caused by motion-uncorrelated reconstruction of CBCT data sets were illustrated by Sonke et al. [43]. In the following, a novel method of motion-correlation for 4D CBCT is presented. The method bases motion-correlation on the direct and real-time measurement of target position provided by the EM tracking system.

4.1 Concept of 4D CBCT

The concept of 4D CBCT imaging revolves around actively accounting for organ motion in the generation of the tomographic data. In contrast to standard 3D CBCT imaging where each imaging session results in one tomographic dataset, 4D imaging generates a set of tomographic datasets with each dataset corresponding to an individual anatomical configuration encountered during the imaging session. The benefit of this concept is

twofold: (1) the tomographic data is free of motion-artifacts and (2) a 4D patient model is obtained, which facilitates 4D treatment planning [12].

Figure 4.1: *Technical concept of the proposed 4D CBCT data acquisition. Here, the electromagnetically measured target position replaces standard respiratory surrogate signals. Red text indicates differences between 4D data acquisition for CBCT versus that for CT as illustrated in the original figure by Vedam et al. [64]. In 4D CBCT, reconstruction is performed after projection sorting; in 4D CT, it is performed prior to (slice) sorting.*

The technical concept of the generation of 4D CBCT datasets developed in the present work is shown in Figure 4.1. The figure is adapted from Vedam et al. [64] who used it to explain their pivotal concept of 4D CT imaging. Relevant differences between the original and the current concept are highlighted with red text in the figure. First, raw x-ray projection data is generated by the onboard kV x-ray imaging option of the ARTISTE prototype Linac—the CBCT scanner. Then, a CT controller provides both the x-ray projections and the projection angles to the projection sorting step. This is in contrast to 4D CT acquisition where CT reconstruction is performed by the CT controller, i. e. prior to sorting. In general, sorting is performed on the basis of a measurement or indicator of organ motion. In the present case, the 4D target position, as reported by the Calypso EM tracking system, is used for projection sorting. Finally, projection sorting requires an x-ray ON signal for time-tagging the projections. The projections are binned according to specific anatomical situations, which can then be reconstructed to obtain tomographic datasets. In Figure 4.1, the bins correspond to phases of the respiratory cycle but other bin assignments are conceivable. For example a binary bin allocation: one bin for the prostate in its typical position and another "trash bin" to sort out projections acquired

during an excursion of the prostate.

The challenges of 4D CBCT imaging in general are manifold. First, the attainable image quality of the tomographic dataset increases with the number of projections that are used for reconstruction [43, 65, 66]. This does not support the aim of using only projections of "equal anatomical configuration". Arguably, each anatomical configuration is unique, which leads to the practical tradeoff of a tight definition of "equal anatomical configuration" versus the attainable overall image quality. The next challenge is the actual measurement of the motion of the patient's anatomy. Various types of motion measurements have been demonstrated such as spirometry, breathing-belt or image processing [43, 65, 67]. These are surrogate measurements, and as as such imply some degree of imperfection, of the motion of the most relevant anatomy including the target volume (and some of the organs at risk). In that respect, the method developed in the present work advances the state-of-the-art in that it is based on a direct measurement of target motion. Another challenging aspect is the uneven angular spacing of the projections after sorting them into bins [68]. This could be overcome by acquiring a large number of projections, which, on the downside, constitutes a tradeoff with the total acquisition time, the total imaging dose given to the patient and with the amount of data that needs to be managed. The work presented here focused on the demonstration of the novel concept of using EM target tracking data as the basis of projection sorting.

4.2 Methods

4.2.1 Data acquisition

The kV CBCT scanner was the ARTISTE prototype described above (Section 2.2). The signal acquisition strategy differed from previously proposed 4D CBCT acquisition methods in that instead of acquiring x-ray projections at defined gantry angles (or angular increments), x-ray image acquisition was essentially triggered by the Calypso System regardless of gantry angle. This was a result of the synchronization scheme described in Section 3.1.3 in which x-ray images are acquired only during cycles of EM silence exclusively. A desired angular sampling frequency was thus achieved by choosing the appropriate gantry rotation speed. In order to obtain projection data with an angular sampling frequency of approximately 2 frames per degree and given the imaging frame rate of the synchronized imaging system of 2.2 fps, the speed of gantry rotation was set to 1 degree/s. Projection data over a 240 degrees rotation of the gantry was recorded. Limitations of the prototype image acquisition hardware prevented collection of more data. The projections were acquired at a resolution of 1024×1024 pixels, representing a field of view of $\sim 25\,\text{cm} \times 25\,\text{cm}$ in the isocenter plane.

Table 4.1: *Summary of CBCT imaging and reconstruction parameters. Data acquisition of the breathing phantom was optimized for reconstruction of 4D CBCT data.*

	Static phantom—3D recon.	Breathing phantom—4D recon.
Gantry rot. speed	300°/min	60°/min
Tube voltage	120 kV	120 kV
Tube current	90 mA	180 mA
SDD[a]	142 cm	142 cm
X-ray pulselength	20 ms	10 ms
Frame-rate	~10 fps	~2.2 fps[b]
Angular frame-rate	2 deg^{-1}	~2.2 deg^{-1}
Total acq. time	45 s	4 min
No. of projections	440	540
Res. of projections	1024×1024 pixels	1024×1024 pixels
Dose at isocenter	1.14 cGy	1.4 cGy
Smooth. filter kernel	13×13 pixels	3×3 pixels
Voxel dimensions	0.5×0.5×0.5 mm^3	0.5×0.5×0.5 mm^3
Cube dimensions	512×512×512 voxels	512×512×512 voxels
Scatter correction	none	none

[a] Source-to-detector distance

[b] Calypso-triggered image acquisitions limited to cycles of EM silence.

The thorax phantom served as the "breathing" test object. It was programmed to perform $\cos^4$-type breathing motion with an amplitude of 2.5 cm and a cycle time of ~4.5 s, which simulated idealized respiratory-induced lung tumor motion of rather large amplitude [69]. In addition, the static thorax phantom was scanned in order to obtain a reference of the image quality attainable using the current CBCT system. The imaging dose at the isocenter inside the thorax phantom accumulated over all projections was estimated by phantom measurements to be 1.14 cGy and 1.4 cGy for imaging the static and the breathing phantom, respectively. A summary of data acquisition and reconstruction parameters is given in Table 4.1. A notable difference in the columns of Table 4.1 is the slower gantry rotation used for imaging the breathing phantom. The rotation speed had to be lowered in order to keep the angular frame rate at an acceptable level, bearing in mind that 4D CBCT reconstruction will further reduce the effective angular sampling (due to projection sorting). Another difference is the shorter x-ray pulselength used for

imaging the breathing phantom, which was chosen in order to reduce motion-related smearing of image signal.

4.2.2 Signal synchronization

The synchronized 4D CBCT hardware generated two groups of signals: (i) the Calypso System's target position recorded on the system's time axis and (ii) up to four additional experimental signals. Figure 4.2 illustrates the sources of and the information encoded by the signals. The EM target position was provided by the Calypso System. The x-ray ON signal was obtained from the controller of the kV x-ray tube. The cycles of EM silence were monitored by the synchronization circuit (Section 3.1.3.2). The potentiometer attached to the carriage of the thorax phantom provided a reference measurement of phantom position in CC direction. An inclinometer (part of the Linac control) provided TTL pulses each half degree of gantry rotation.
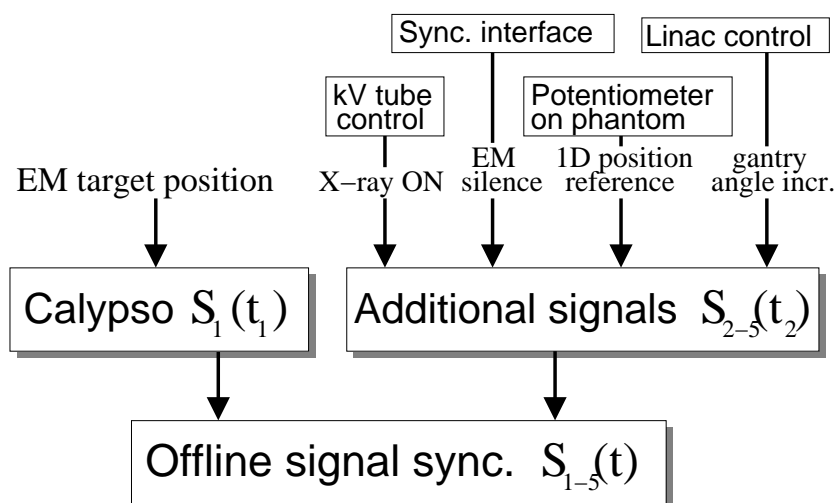
Figure 4.2: *Illustration of the signal synchronization scheme. $S_i(t)$ denotes the time series of a signal i. The indices of t distinguish the time axes of the two recording environments. Synchronization pulses stemming from both time axes (t_1 and t_2) were used for offline signal sync. (See text for details.)*

The two groups of signals were synchronized onto a unique time axis in an offline procedure. This procedure used the cycles of EM silence as a sequence of synchronization pulses. This sequence was obtained twice; once on each time axes t_1 and t_2 (see Figure 4.2). On axis t_1, the sequence of cycles of EM silence was derived from the Calypso tracking data; on axis t_2, it was measured directly by the synchronization circuit. Finally, the pattern of synchronization pulses from t_1 and t_2 could be matched with millisecond precision yielding one unified time axis t.

4.2.3 Image reconstruction

The process of image reconstruction involves some extra aspects if 4D CBCT generation is the goal compared to 3D CBCT reconstruction. First, the common methods will be presented, followed by a description of the additional aspects of 4D CBCT generation. Common to both methods were the steps of pre-processing of the raw projection data. The spatial variations of detector gain and dead pixels were compensated in the projection data by appropriate application of gain and dead-pixel maps. Non-eccentric gantry motion was corrected by a geometrical calibration procedure that involved imaging of a phantom holding steel spheres in a helical arrangement [49]. This process generates one transformation matrix $\boldsymbol{P}$ for each viewing angle under which the calibration phantom was imaged. In this work, 360 projections of the calibration phantom were acquired at $1°$ angular spacing. In order to obtain transformation matrices at $0.5°$ angular spacing, the original full degree matrices were interpolated using higher order polynomial fitting functions (typically the order was in the range 6–10; the quality of the fit was assessed visually and by analysis of the residuals). In general, obtaining a functional representation of the $\boldsymbol{P}$'s through curve fitting may be beneficial even if enough projections of the helix calibration cylinder could be acquired because it effectively removes noise from the measurements. Also prior to reconstruction, a noise-smoothing filter (as indicated in Table 4.1) was applied to the projections and their pixel resolution was down-sampled by a factor of four. A Feldkamp algorithm [25] was used for the reconstruction of CBCT data sets with $512\,(\mathrm{LR})\times512\,(\mathrm{AP})\times512\,(\mathrm{CC})$ voxels. A Shepp-Logan filter was used in the filtered backprojection step. The voxel size was $0.5\,\mathrm{mm}$ in all directions. A scatter correction was not employed.

The extra aspects of 4D CBCT generation included the assignment of projection angles to each projection at half-degree precision. As indicated in Table 4.1, the angular frame rate of the Calypso-synchronized CBCT scanner was approximately 2.2 frames per degree. This frame rate varied to some extent depending on the timing variability in the Calypso duty cycle (approximately $\pm5\%$ standard deviation). However, the current reconstruction code at DKFZ requires even angular sampling at angles for which transformation matrices exist, e. g. half-degree angles. Therefore, half-degree angles were assigned to the projections based on the signal that encoded the gantry angle (see Figure 4.2). This meant that at every ninth half-degree or so, two frames would be assigned to the same angle. When that happened, one of the two frames was picked at random. The error introduced by the artificial angle assignment was estimated to be minor because the adjustments were small (< 0.25 degrees).

The next step was to assign certain phases of the breathing cycle to the projections— for example the three phases inhale, exhale and mid-ventilation indicated in Figure 4.3. An amplitude-based projection sorting strategy was applied [70]. The positions of the

phantom were scaled between 0% and 100%, denoting the maximum exhale and inhale positions of the simulated breathing motion, respectively. From this range, projections acquired within an arbitrary band of tolerated positions could be selected for reconstruction. Projections that did not fall within this range of positions were excluded from the reconstruction.

4.3 Results

First, the alignment of the different time axes (signal synchronization) will be discussed and subsequently, examples of CBCT image reconstruction will be presented.

4.3.1 Signal synchronization

Figure 4.3 shows the result of synchronizing the time axis of the kV CBCT system of the ARTISTE Linac with the time axis of the Calypso System and the signals used to synchronize. The upper panel of the figure shows the target position in the direction of phantom motion (CC) as computed by the Calypso System and as measured by the reference measurement (cf. potentiometer signal in Figure 4.2) as functions of time. It is important to note that no scaling (i. e. multiplication by a factor) was applied to the measurements of target position, neither to the amplitude nor to the time axis.

The lower panel of Figure 4.3 summarizes the synchronization signals and the signals necessary for 4D CBCT generation. At the top (*Synchronization*), the sequences of EM silences are shown—one derived from the Calypso data and one measured by the synchronization circuit (cf. Figure 4.2). These two pulse trains were used in a key-lock fashion to generate the unified time axis t from the separate time axes t_1 and t_2. The next signal in the lower panel of Figure 4.3 shows the pulse sequence from the Linac indicating half-degree angle increments of the gantry (*Angle Incr.*). The speed of gantry rotation of 1 degree/s can be reproduced from this pulse sequence. Below that, pulses marking the acquisitions of kV x-ray images are shown (*X-ray ON*). It can be observed that images were acquired slightly more frequently than twice per second, namely at a rate of 2.2 fps. Image acquisition was triggered by the onset of periods of EM silence, i. e. at the onset of the synchronization pulses shown at the top of the figure. The signal at the bottom of the figure (*4D recon*) gives an example of the x-ray images included in the 4D image reconstruction of the exhale phase. It is an amplitude-gated (according to the CC EM signal) version of the X-ray ON signal; it was not recorded physically.

A first observation is that a good agreement between the reported EM target position (black diamonds in Figure 4.3) and the reference measurement when tracking this regular phantom motion. Another observation is that the EM measurement of target position
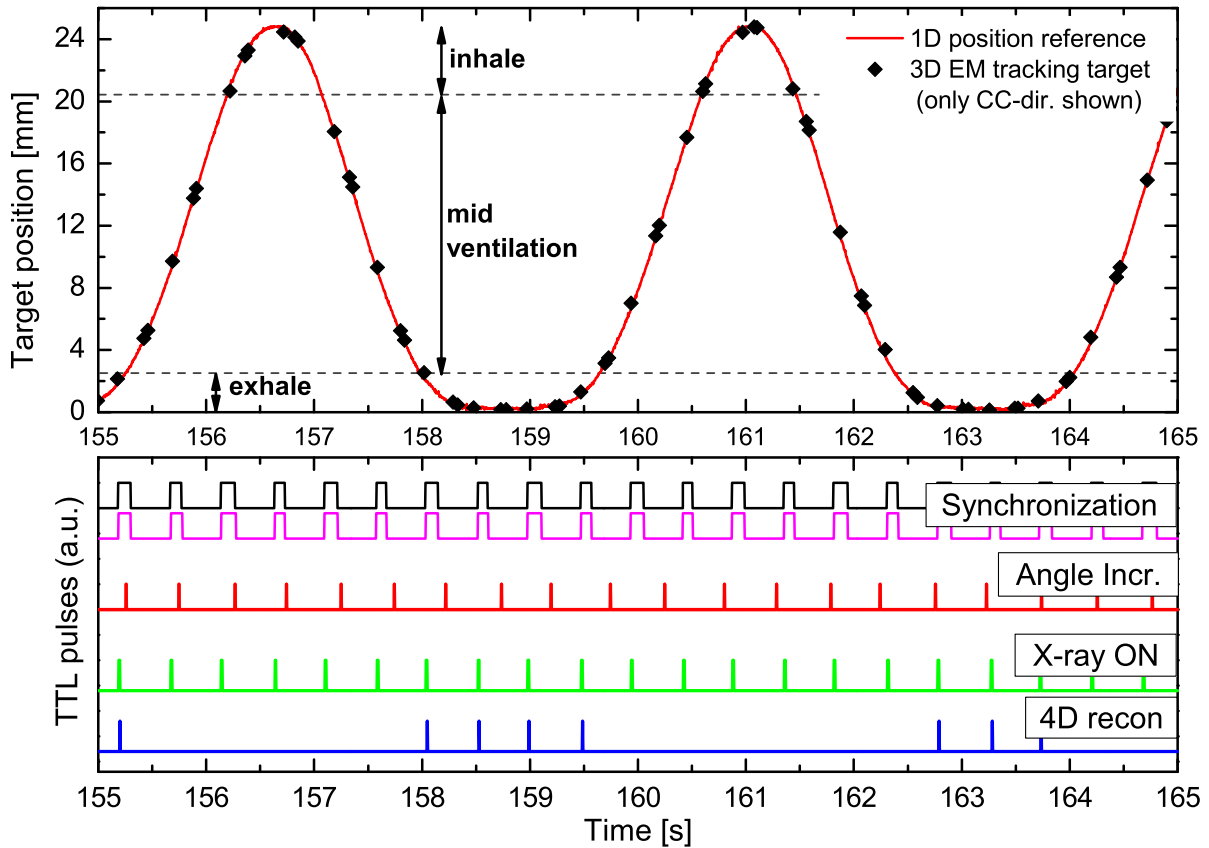
Figure 4.3: *The CC-coordinate of the 3D EM tracking target as determined by the Calypso system and by the reference measurement are shown in the upper panel. The signals used for synchronizing the kV CBCT system with the Calypso System are shown in the lower panel.*

appears free of lag compared to the reference measurement. Some amount of lag (delay along the time axis) in EM tracking would be expected due to the finite amount of time that will pass from the moment of transponder localization to the end of target computation by the Calypso System. However, the time-stamps of the EM tracking data were internally assigned so as to compensate the lag of the Calypso System. This is beneficial for the present purposes of 4D CBCT generation where the data is processed offline. For real-time applications such as DMLC control, system lag is a critical characteristic that needs to be measured. In that case, if the Calypso System reported the time when target computation finished (without lag compensation), the synchronization with external signals developed in this work could be a helpful tool to measure the lag of the Calypso System.

4.3.2 Image reconstruction

The outcome of CBCT image reconstruction will be reviewed; first, for the case of a static phantom and, secondly, for the case of the breathing phantom. Image quality will be assessed from a proof-of-principle perspective. A complete assessment of the image quality must be performed when the kV CBCT capabilities of the ARTISTE Linac are technologically mature and when EM transponders can be implanted in the lungs of patients. Possible improvements to the CBCT method will be discussed in Section 6.2.

4.3.2.1 Static thorax phantom—3D reconstruction

Prior to discussing the 4D CBCT images, the highest image quality attainable using the prototypical CBCT scanner available at DKFZ will be assessed. Because image quality will somewhat depend on the object imaged, the same thorax phantom was used for this evaluation. The phantom was static in order to avoid motion artifacts.

Figure 4.4 shows images obtained using the prototype kV CBCT Scanner of the ARTISTE Linac. The images are displayed at a range of 700 Hounsfield units. The anatomy of the phantom is clearly recognizable. The two simulated tissue types (lung tissue and water-equivalent other tissue) are depicted with sharp transitions and the transponders are easily detected in the sagittal slice in Figure 4.4b. The image quality is sufficient for con-

(a) Transversal slice #1   (b) Sagittal slice   (c) Transversal slice #2
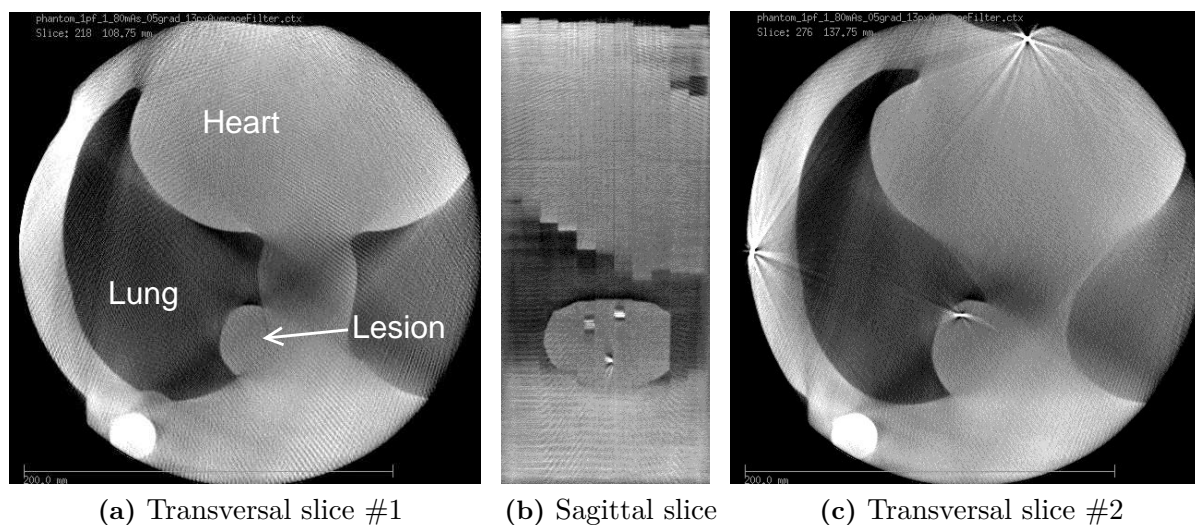
Figure 4.4: *Slices from a 3D CBCT dataset of the static thorax phantom (cf. Figure 2.10) intended to illustrate the image quality attainable from the CBCT system. Dark areas represent lung tissue; light gray areas represent water-equivalent tissues (rib cage, heart, tumor, mediastinum). White areas represent metals and associated image artifacts (particularly in the transversal slice #2 in (c)).*

fident organ delineation. However, a number of image artifacts are apparent as well. For

example, so called cupping artifacts manifest themselves as decreasing image intensities towards the center of the transversal slices in Figure 4.4. Cupping artifacts are caused by beam hardening and depth-dependent scatter-primary-ratios and are thus an inherent issue in cone-beam imaging where large scatter-primary ratios (commonly, values of 2–10) are involved [23]. Another image artifact is the streaking around and between high-density objects, also a well characterized phenomenon in CT imaging [71]. This artifact is most obvious in Figure 4.4c, where a slice intersecting a transponder and two BBs embedded at the phantom's surface was chosen for display. A less obvious manifestation of this artifact is a fan of higher image intensity entering the transversal slices in Figure 4.4 from the lower left corner. This is a streaking artifact caused by the metal rails (outside of the FOV towards the bottom of the images) of the thorax phantom. Additionally, some finer structured streaking is visible across the transversal image slices, which can be attributed to the wires in the Calypso magnetic array positioned above the thorax phantom (outside of the FOV). Corrections for these artifacts are necessary if dose calculations were to be performed on the CBCT data and thus such corrections are an area of active research [for example 72, 73]. Corrections were disregarded in the present work as the focus was on the introduction of a new motion-correlation method. In summary, the images in Figure 4.4 give an impression of the basic image quality attainable with the current prototype CBCT system. This image quality is expected to improve if advanced artifacts corrections were implemented and objects without metallic components (which is the case in most patients) were imaged.

4.3.2.2 Breathing thorax phantom—4D reconstruction

Figure 4.5 is a practical representation of the complete projection data available to 4D CBCT reconstruction. The diagram to the left arranges the projections in the plane spanned by the time and the target position. For this purpose, the $\cos^4$-type target motion has been mapped to a per cent scale with 0% representing the full exhale position; 100% the maximum inhale position. This representation allows a quick assessment of the spatio-temporal distribution of the projection data and is particularly convenient if only 1D target motion is concerned (as measured from the thorax phantom). Three-dimensional target motion would require a different graphical representation or a simplification (projection) to a 1D component of the motion. The histogram representation of the projection data displayed in the right diagram of Figure 4.5 illustrates one of the trade-offs involved in 4D CBCT imaging. The bins of the histogram match the three-part classification of the breathing motion indicated in Figure 4.3. The specific trade-off consists of the conflicting goals of maximizing the number of projections used in CBCT reconstruction and minimizing motion artifacts. Both goals aim at improving image qual-
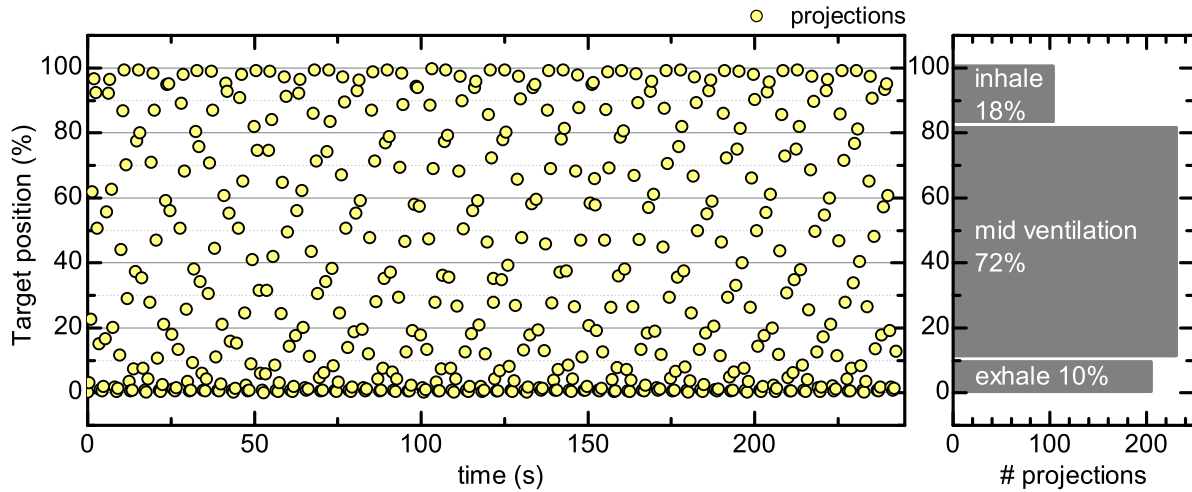
Figure 4.5: *Projections for CBCT reconstruction arranged in the plane of time and target position (left diagram). Histogram of the projections (right diagram) based on the bins indicated in Figure 4.3. 540 radiographs of the thorax phantom were acquired in a 240° gantry rotation. The thorax phantom performed 13 cycles of regular* $\cos^4$*-type breathing motion. (Graphical representation adapted from [65])*

ity[1]. Maximizing the number of projections means broadening the bins of the histogram in Figure 4.5 which, in turn, will lead to increased motion artifacts because projections from a wider range of target positions are combined. This trade-off can be overcome by the acquisition of a large number of projections—typically 700 to 1000 per dataset—such that enough projections per bin are available. In respiratory-correlated CBCT, breathing cycles are usually subdivided into 6–10 bins with approximately 100–200 projections per bin. The present hardware was limited in the number of projections that could be acquired such that the consequences of the trade-off can be understood from the arbitrary three-bin approach suggested in Figure 4.5: (i) the inhale bin is of acceptable width (18%) but contains only ~100 projections; (ii) the mid ventilation bin contains a suitable number of projections (~220) but is too wide to reduce motion artifacts; (iii) the exhale bin—owing to the $\cos^4$-type motion—is a good compromise in terms of narrow bin width and number of projections. In order to prove the concept of motion-correlation based on EM target localization, it may suffice to consider only the most advantageous case: CBCT reconstruction of the exhale phase.

Figure 4.6 shows the region around the simulated lung lesion in both a transversal and a sagittal slice of the CBCT data set, with each view taken once from a motion-

---

[1]The angular arrangement (coverage, spacing) of the projections is another important parameter of image quality. For example, image quality will be at a maximum if some N projections are evenly spaced across 360°. If the same N projections are arranged in angular clusters, image quality will be worse [68].

uncorrelated reconstruction (all frames) and once from a reconstruction of the projections in the exhale bin. The pulse sequence at the bottom of Figure 4.3 (*4D recon*) shows when some of the exhale projections were acquired. The images in Figure 4.6 exhibit metal

(a) all projections   **(b)** 10% exhale   **(c)** all projections   **(d)** 10% exhale
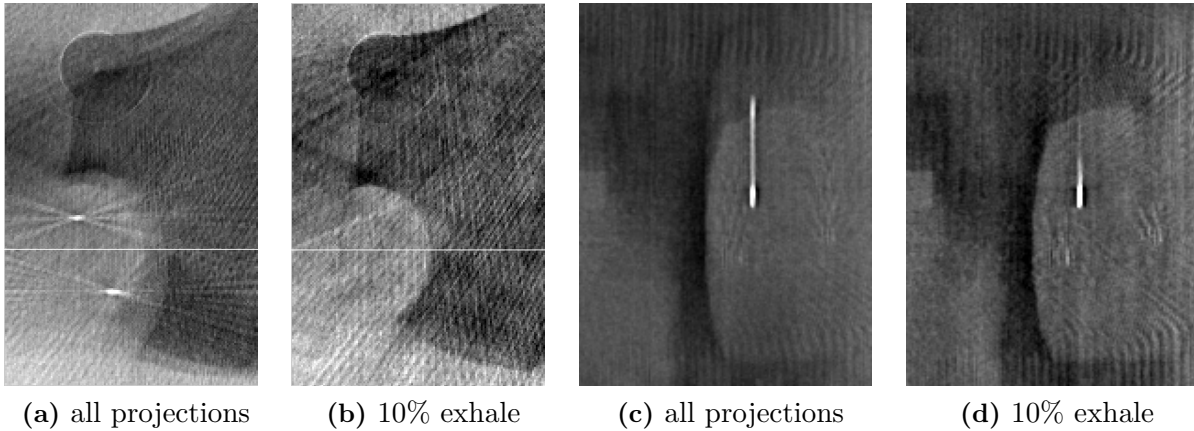
Figure 4.6: *Corresponding transversal and sagittal slices of a CBCT dataset showing the simulated lesion in the breathing thorax phantom. Motion artifacts apparent in (a) and (c) [un-sharp tissue transitions in (a) and (c), two spurious Beacon transponders (bright spots) in (a), smeared out bright trace of a Beacon transponder in (c)], have vanished in (b) and (d) due to motion-correlated image reconstruction. The white lines in (a) and (b) are drawn for orientation (see text for details).*

streaking artifacts that, as explained in Section 4.3.2.1, are mostly caused by features of the phantom (metal screws and support rails, steel BBs on the phantom surface). In addition, Figures 4.6b and 4.6d appear noisier than Figures 4.6a and 4.6c, which is due to the reduced number of projections used in the reconstruction. The effect can be assessed by the following first order estimation. The imaging dose used for a CBCT dataset scales linearly with the number of projections. In turn, the CNR increases as the square root of the dose [43, 74]. Hence, the following relation should hold true

$$\frac{\text{CNR}_{\text{exhale}}}{\text{CNR}_{\text{all proj}}} \approx \sqrt{\frac{P_{\text{exhale}}}{P_{\text{all proj}}}} = 0.62, \tag{4.1}$$

where P denotes the number of projections. This relation can be shown to hold true based on CNR values determined in Figures 4.6a and 4.6b, indicating that CNR degradation is due to the relative increase of x-ray quantum noise in the 4D (exhale) CBCT data set. Calculation of the CNR was performed as follows

$$\text{CNR} = \frac{|\langle S_1 \rangle - \langle S_2 \rangle|}{\sigma}, \tag{4.2}$$

where $\langle S_1 \rangle$ is the average signal of the tumor insert, $\langle S_2 \rangle$ is the average signal in the

lung region and σ is the average standard deviation of the signal (i. e. noise) in the entire region of interest, e. g. the image of Figure 4.6a.

The main difference in the appearance of the motion-correlated versus the motion-uncorrelated images in Figure 4.6 is the correction of motion artifacts. While in Figure 4.6a motion artifacts manifest themselves as smeared out or ghosted tissue transitions and as spurious Beacon transponders (bright spots), these artifacts are eliminated by the motion-correlated reconstruction of the data set. The most obvious motion artifact in Figure 4.6c is the smeared out bright trace of a Beacon transponder whose appearance in Figure 4.6d is mostly restricted to its true position in the exhale phase. Figure 4.7
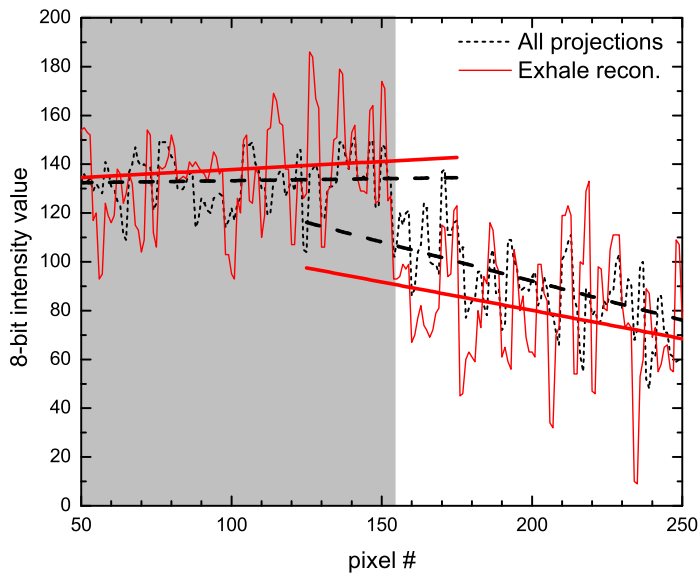
Figure 4.7: *Intensity profiles through the sections of the CBCT slices shown in Figures 4.6a (black dashed lines) and 4.6b (red solid lines) at the positions indicated by the white lines in these images. The transition from the shaded to the white area in the diagram indicates the position of the transition from tumor to lung tissue in the CBCT slices. Straight lines are trendlines through the data before and after the tissue transition.*

illustrates the clearer definition of the tissue transitions in the form intensity profiles. The contrast (intensity difference between corresponding trendlines at the position of the tissue transition) is larger in the case of the exhale-only reconstruction. However, at the same time the noise in the signal increases causing the CNR degradation measured above.

4.4 Summary

A method for the generation of motion-correlated CBCT datasets based on EM target tracking was presented. The developments of the present work that enabled this CBCT imaging application are, first, concurrent x-ray imaging and EM target tracking and, secondly, signal synchronization (i. e. correlation of the time axes of the Calypso System and of the Linac). The image quality of the CBCT data was compromised by the metal components of the thorax phantoms and by limitations of the prototype CBCT scanner. The most relevant limitation of the CBCT scanner in terms of image quality was the

number of projections that could be acquired per acquisition (~540) due to the proto-typical acquisition hardware. An improvement of image quality can be expected with an upgraded CBCT scanner that overcomes this limitation.

The new method of motion-correlation can inherently stabilize the therapy target in CBCT datasets because the target's position is considered directly rather than using a surrogate position measurement. A stabilized target means that the images give a sharp representation of the target area without motion-related signal smearing or reconstruction artifacts [43, 64]. In the presence of irregular motion such as irregular breathing patterns or organ motion due to causes other than breathing, target stabilization can only be achieved by the incorporation of knowledge of the target's position at any given time. The proposed method provides a solution to managing arbitrary target motion in CBCT imaging.

Chapter 5

Clinical Trial

The realization of a clinical prostate trial at DKFZ using the Calypso System was a central part of this research. For the first time, the combination of the ARTISTE radiotherapy suite and the Calypso System would be demonstrated and, for the first time as well, patients outside of the USA would benefit from EM target tracking. In this chapter, the preparation, the design, the goals and the status of the clinical prostate trial at DKFZ will be presented.

To date, the published data that involves EM target tracking using the Calypso System is based on a 41-patients study conducted at five institutions in the USA in 2005–2006 [6, 31]. This database has been analyzed with respect to a number of clinical questions such as statistical analyses of intrafraction prostate motion [6, 75], quality of prostate motion prediction using imaging [76] or the dosimetric impact of different prostate motion management schemes [77, 78]. Numerous abstracts based on this database have appeared in conference proceedings.

From a clinical research perspective, the setup at DKFZ is unique in that gold-standard image data can be acquired with the patient on the treatment couch using the in-room Primatom CT-on-rails (single-slice kV helical CT scanner). Alternatively, MV CBCT image data can be acquired with the patient in treatment position. The imaging data collected during the multi-center study mentioned above is limited and mostly based on 2D stereoscopic x-ray imaging, 2D portal imaging or, in the best case, kV CBCT. Limited information content (2D imaging) or limited image quality (CBCT) render the direct comparison of imaging data with the point tracking data provided by the Calypso System a difficult task. A prostate study at DKFZ adds to this research the possibility to compare the Calypso data to frequent (potentially even daily) CT imaging data, which allows assessment of clinical questions such as prostate rotation or positional variations of the seminal vesicles and surrounding soft-tissues (e. g. rectal wall).

5.1 Study design and registration

The concept of the prostate study at DKFZ is to use the Calypso System alongside the established IMRT techniques for prostate patients. In a first stage, the impact of the Calypso System on treatment decisions would be limited to the triggering of additional control CTs during patient setup if necessary (details below). In a second stage (after initial experiences with the Calypso System have been positive), repositioning of the patient during treatment delivery based on the real-time EM prostate tracking data would be considered. Analysis of the study data should allow a comparison of image-guided with EM-guided patient setup. If the comparison yields equal or better patient positioning results using EM-guidance, CT imaging sessions could be spared in the future, saving the patient both time-on-table and non-conformal imaging-dose. To this end, a prospective feasibility study was designed in a collaborative effort involving

- the Department of Radiooncology and Radiotherapy of the University Clinic of Heidelberg: Dr. K. Herfarth (lead investigator), Dr. M. Münter,

- the Department of Urology of the University Clinic of Heidelberg: Dr. J. Pfitzen-maier,

- the Clinical Cooperation Unit of Radiotherapeutic Oncology of the DKFZ: Dr. P. Huber

- and the Division of Medical Physics in Radiation Oncology: Dr. U. Oelfke, A. Rau.

The study proposal entitled *"Online localization of the position of the prostate and possible repositioning in intensity modulated radiotherapy under image guidance (IGRT) using implanted radio-transmitters"* outlines a sequence of steps for enrolled patients that is illustrated in Figure 5.1. The study proposal was approved by the ethics committee of the Faculty of Medicine of the University of Heidelberg and was announced to and approved by the competent authority, which is the "Regierungspräsidium Tübingen". The complete study proposal was filed and published in the database of the "Deutsches Institut für Medizinische Dokumentation und Information" (DIMDI) and can be accessed via the reference number *DE/CA48/54.4-17/5552.21-1.17/0008207*. Up to 30 patients can be enrolled in the study and treated to the following endpoints (as defined in the study protocol):

- **Primary endpoint**

    - Assessment of the correlation of prostate positioning based on the Calypso System through CT imaging

Preliminary examinations: histologic examination, staging	Dept. of Radiooncology and Radiotherapy of the University Clinic of Heidelberg
Eligibility assessment: application of exclusion and inclusion criteria	Dept. of Radiooncology and Radiotherapy of the University Clinic of Heidelberg
Patient information and informed consent	Dept. of Radiooncology and Radiotherapy of the University Clinic of Heidelberg
Transponder implantation: ultrasound guided	Dept. of Urology of the University Clinic of Heidelberg
Planning CT and radiotherapy planning	DKFZ Clinical cooperation unit & Div. Medical Physics
Radiotherapy: with concurrent EM target tracking	DKFZ Clinical cooperation unit & Div. Medical Physics

Figure 5.1: *Outline of the steps required for the realization of the clinical prostate trial using the Calypso System. The institutions responsible for each step are listed in the cells to the right.*

- **Secondary endpoints**

  - Acquisition of 3D prostate motion during radiotherapy
  - Measurement of the time effort involved in using the Calypso System
  - Monitoring of transponder migration
  - Patient compatibility of the implant procedure.

5.2 Workflows

Workflows[1] were modeled for all aspects of the study that would deviate from standard operating procedures. These aspects include patient immobilization devices, acquisition and preparation of the planning CT, treatment planning, plan verification and treatment documentation, i.e. nearly all aspects of RT. Clearly, the core research questions would be answered during the patients' treatment fractions. Therefore, the workflows developed for the treatment fractions will be presented here.

Figure 5.2 shows the typical treatment loop of fractionated radiotherapy in which the patient is immobilized, then positioned and finally treated.[2] The aids and procedures used

---

[1] *Workflow* and *Process* are here used somewhat interchangeably. In theory, a workflow is a more abstract description of some procedure, while a process is the detailed formulation of it.

[2] The workflow diagrams use the Business Process Modeling Notation (`http://www.bpmn.org/`) and were produced using the free modeling software from BizAgi, Buckinghamshire, UK (`http://www.bizagi.com/`).
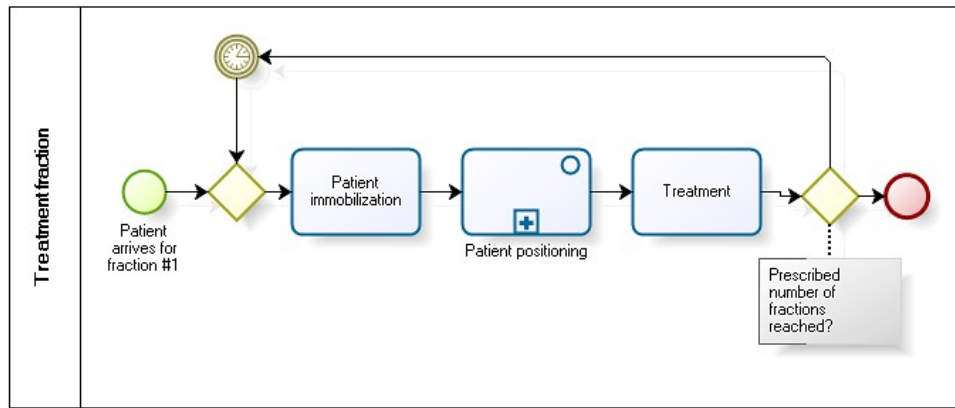
Figure 5.2: *The typical treatment loop of fractionated radiotherapy. Workflows specific to the study were defined for patient immobilization and for patient positioning. The timer (circle with clock) pauses the loop—typically for 24 hours—before it repeats.*

to accomplish each of the three steps may vary between institutions, between indications and even from patient to patient. The patient enters this loop either when he arrives to get his first or any subsequent fraction and leaves the loop upon completion of the last fraction. The process of patient positioning is most specific to the study; it is illustrated in Figure 5.3. First, the patient is positioned conventionally, i.e. aligning the treatment isocenter (marked on the patient's skin or some fixation device) to the room isocenter using the room laser system. Then, the prostate is localized using the Calypso System.
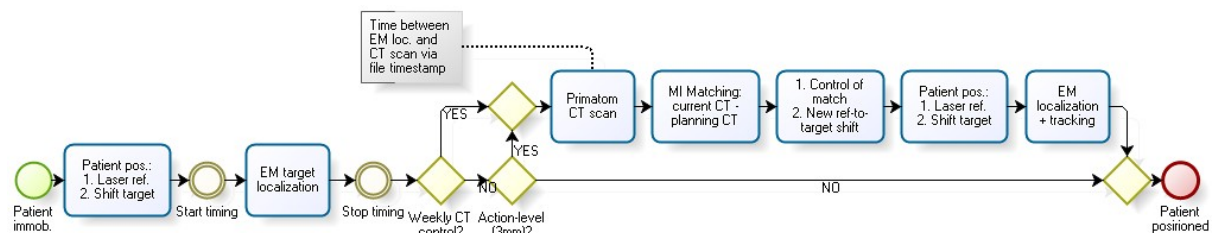
Figure 5.3: *The process of patient positioning according to the study protocol. Control CT scans are acquired if the Calypso System reports >3 mm misalignment or if a week has passed without control CT scan.*

The time needed to operate the Calypso System will be measured. After initial prostate localization, the need for a control CT scan is determined. A control CT scan is performed either if a week has passed without a CT scan or if the Calypso System reported a misalignment between treatment and room isocenter that is greater than 3 mm in any of the directions. If the latter triggers a control CT scan, the idea is to obtain an image-guided shift vector that optimally positions the patients and that, in retrospect, can be compared to the EM-guided shift.

If the CT scan is performed using the Primatom CT-on-rails, a 90° table rotation

(around the z-axis) is required to convey the patient from the treatment position to the CT imaging position. The table rotation introduces some uncertainty into the comparison of EM-based and image-based prostate localization both due to the time delay between the two measurements and due to the mechanical accelerations imposed on the patient during the table rotation. These uncertainties will have to be quantified, for example by comparing the EM localization results from before and after the CT scan. If the CT scan is a MV CBCT, the patient is imaged with the onboard imaging equipment (cf. Figure 2.5a); the patient on the table remains in treatment position.

After a control CT scan has been acquired, a corrective table shift has to be computed based on this new CT scan. This process must be performed quick, safe and well documented. The quickness is a general requirement of all image-guided procedures because the probability for intrafractional motion to occur increases with the time between image acquisition and the commencement of the actual treatment—the so called *blind gap* [79]. Again, the procedures to obtain the corrective table shift vectors differ depending on the type of control CT. If the control CT scan is a MV CBCT, image matching and shift vector calculation is seamlessly integrated with the Siemens radiotherapy workflow. If the control CT scan is a Primatom kV CT, automatic matching to planning CT data is not yet a routine process in the Siemens radiotherapy workflow. For study purposes, matching could be performed using the in-house developed Virtuos software [80]. However, for both scenarios the matching result have to be evaluated—and potentially corrected—by an oncologist and the new shift vector needs to be confirmed. Now, the new shift vector is applied, the patient's prostate is re-localized and subsequently tracked using the Calypso System und, finally, the patient would be ready for treatment. Treatment interventions such as repositioning the patient would be in accordance with the study protocol, but they will only be considered after some initial clinical experience with Calypso System has been gathered.

5.3 The clinical tabletop

The Siemens TT-M tabletop in combination with the Calypso Overlay (cf. Table 2.1) was chosen as the clinical tabletop option based on the results in Section 2.4.2.2 and due to the support granted by the manufacturer of the Calypso System. The compatibility of this tabletop option with respect to CT imaging, geometric clearance and dosimetry required evaluation.

5.3.1 Imaging

An Alderson RANDO pelvic phantom [81] was used to test the impact of the TT-M tabletop on CT image quality. Figure 5.4 shows CT images of this phantom acquired in

(a) Transversal slice #1   **(b)** Sagittal slice   **(c)** Transversal slice #2
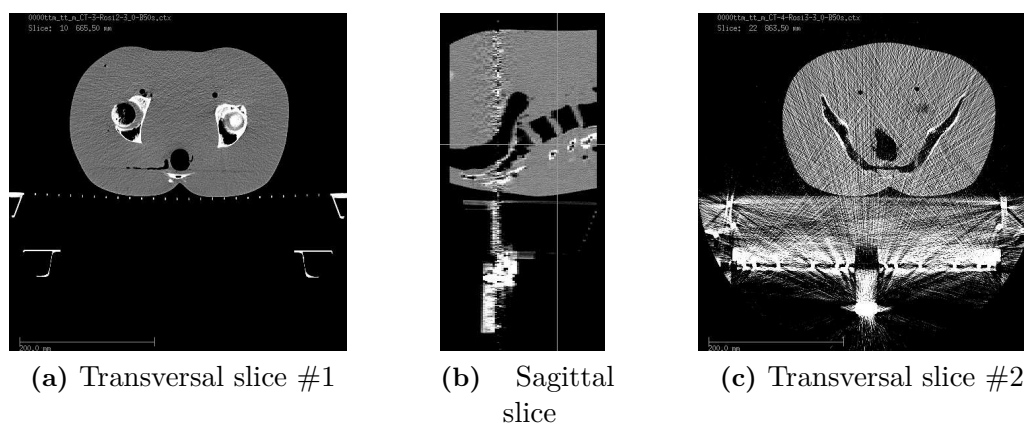
Figure 5.4: *CT imaging compatibility of the TT-M tabletop in combination with the Calypso overlay. In the prostate region of the tabletop (blue element in the image in Table 2.1), the transversal slice of a CT image in (a) of a pelvis phantom is free of artifacts. In the junction region where the headpiece connects to the baseframe of the tabletop, severe metal streaking artifacts are visible [(b) and (c)].*

two different regions of the TT-M tabletop: Figure 5.4a was acquired with the phantom placed in the prostate region of the tabletop (blue element in the image in Table 2.1); in Figures 5.4b and 5.4c the phantom was placed in the junction region where the head-piece connects to the baseframe of the tabletop. The results show that when imaging is performed in the prostate region of the tabletop, optimal image quality can be expected. However, if head&neck patients were to be treated on the same tabletop, they would have to be positioned such that the junction region of the tabletop is avoided. This region is unsuitable for both imaging and treatment. At DKFZ, the TT-M tabletop would only used for the prostate patients enrolled in the study thus ensuring compatibility of the tabletop with imaging procedures.

5.3.2 Geometric clearance

Geometric clearance of the TT-M tabletop plus overlay posed serious challenges for its usage in the IGRT workflow at DKFZ. As can be seen from the measures given in Table 2.1, a box of $53 \times 19 \, \text{cm}^2$ defines the transversal cross-section of this tabletop option, which in the $70 \, \text{cm}$ diameter bore of the CT scanner leaves little space for the patient and fixation aids. In order for the patients to still fit through the CT bore, first, the

stereotactic body frame[3] had to be removed from the workflow and, second, the patients would lay directly on the treatment table without any body cast fixation or vacuum mattress similar to the Alderson RANDO phantom in Figure 5.4. The clearance issues were similar with the Primatom CT and the onboard MV CBCT. Giving up the stereotactic patient positioning meant that a Primatom-based workflow would potentially loose patient positioning accuracy and thus be inadequate for a comparison between CT-based and EM-based patient positioning. In consequence, the MV CBCT-based workflow was found appropriate for the TT-M tabletop. In the future, the kVue tabletop (see Table 2.1) solution should be investigated further. It promises to allow a Primatom-based workflow, which would recuperate the superior image quality of kV CT compared to MV CBCT.

5.3.3 Dosimetry

The dosimetric evaluation of the TT-M tabletop option was concerned with the question whether the tabletop had to be included in the dose calculations performed during treatment planning. For instance, the TT-D tabletop (see Table 2.1) can be excluded from the dose calculations because its radiological thickness is negligible. The advantage is that the radiotherapy tabletop (TT-D, TT-M, etc.) does not need to be present in the planning CT. AT DKFZ, the planning CTs are typically acquired on a Toshiba CT scanner that uses its own low-attenuation tabletops, which are different from the Siemens radiotherapy tabletops.

The dose impact of the TT-M tabletop option was evaluated in a planning study. The CT cube with the Alderson RANDO phantom in prostate treatment position on top of the TT-M formed the basis for dose calculation. A treatment isocenter was defined in the prostate region. No further anatomy (tumor, organs at risk, etc.) was defined. A duplicate of the CT cube was created with all structures (tabletop, overlay) outside the phantom set to Hounsfield values of -1000, i.e. radiologically invisible. A seven-beams plan was calculated. Open fields (approx. $8 \times 8\,\mathrm{cm}^2$) were used. The two beams coming from underneath the table were arranged worst-case, i.e. such that they each traversed the tabletop structures along the longest possible paths. A dose of 1 Gy to the isocenter was prescribed. The dose was calculated using a superposition algorithm.

The results of the dose calculation are shown in Figure 5.5. A certain dose build-up can be observed in Figure 5.5a for the two beams that traverse the table structures before entering the patient. Naturally, this effect is absent in Figure 5.5b. This dose buildup will reduce the skin sparing effect because it shifts the dose maximum of the depth-dose curve towards the patient's skin. Quantitatively, the effect manifests as a 1%–3% dose increase at the phantoms dorsal surface apparent in Figure 5.5c as the red/purple

---

[3]To get a complete introduction to the techniques of stereotactic patient fixation, the reader may be referred to Schlegel et al. [82].

(a) Dose calc. table incl.　　**(b)** Dose calc. table excl.　　**(c)** Difference (a) minus (b)
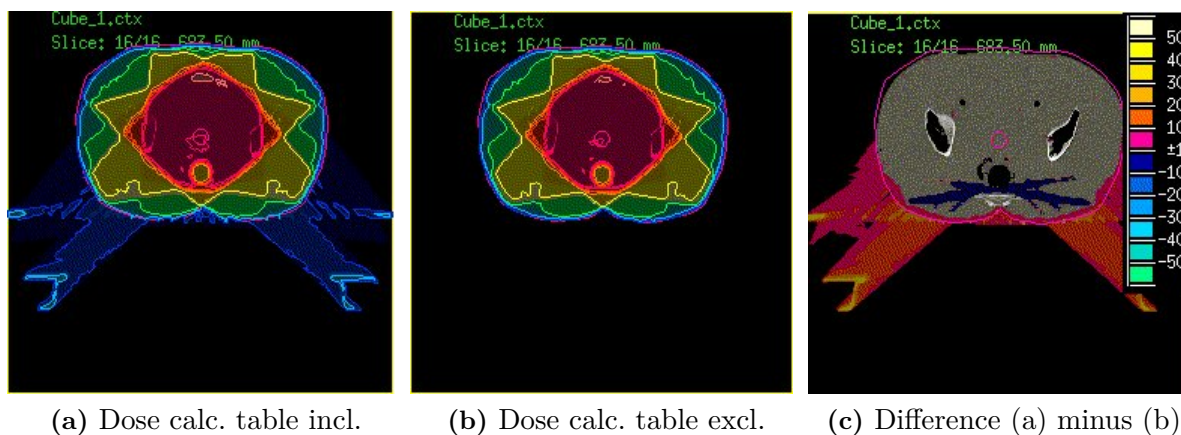
Figure 5.5: *Comparison of a dose calculation that includes the TT-M tabletop plus overlay (a) with a calculation that excludes the tabletop (b). The result, shown as the difference in dose, is shown in (c).*

colorwashed area that falls inside the pink contour. At the same time, the presence of the table structures causes 3%–5% dose reduction (blue colorwash inside the pink contour) inside the phantom, which is caused by x-ray attenuation in the blue Kevlar insert of the Calypso overlay (see Table 2.1). Finally, the change in radiological depth for the two critical beam directions was measured and it was found that the table structures increased the radiological depth by $5 \pm 0.5\,\text{mm}$. In conclusion, the dose impact of the TT-M tabletop option was found too be small but not negligible and it was decided that the tabletop should be present in the planning CTs.

In order to make the TT-M tabletop available in the planning CTs, a software was developed as part of this thesis that inserts the tabletop into the planning CT cubes. This work resulted in the two software modules `modify_ct` and `modify_ct_UNDO` illustrated in Figure 5.6. The module `modify_ct` takes the original planning CT ("yellow" files in Figure 5.6) and shifts the patient upwards somewhat to create space underneath the patient where the tabletop can fit. It then imports CT images of the TT-M tabletop and inserts the TT-M image data at an appropriate position in the planning CT. Finally, it saves the modified CT data ("red" files in Figure 5.6) and deletes the original CT data for safety reasons (so that the CTs cannot be confused). The modified CT image data contains the TT-M tabletop and can thus be used for treatment planning of patients that are enrolled in the study. If, at some later point, it is decided that the patient will be treated at another site, e.g. at the University Clinic, which most probably would use the regular TT-D tabletop, the TT-M tabletop can be removed from the planning CTs using `modify_ct_UNDO`. This operation yields the "green" files Figure 5.6. The patient would not be shifted again by `modify_ct_UNDO` so as to preserve any contours already drawn in the planning CT at that point.
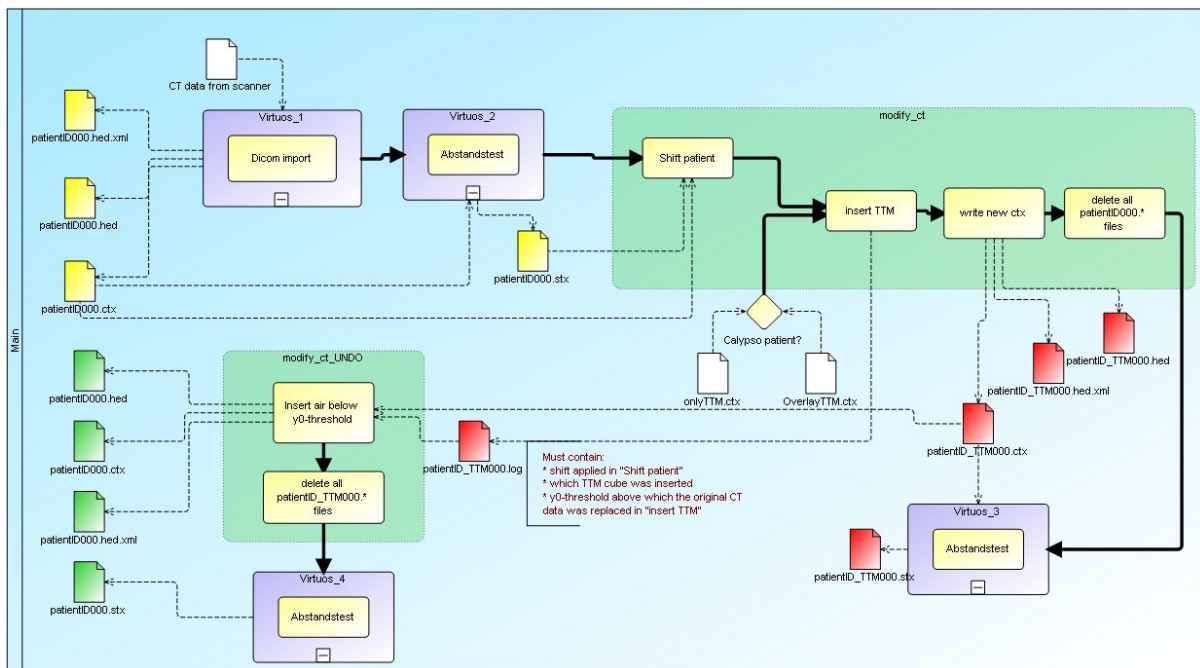
Figure 5.6: *Diagram of the process developed for the insertion of the TT-M tabletop into the planning CTs. The process makes use of the in-house Virtuos software package and of two the two software modules* `modify_ct` *and* `modify_ct_UNDO` *developed in this work. The latter module is used to reverse the changes, i. e. to remove the TT-M tabletop from the CT cubes, if necessary.*

5.4 Status report

The recruitment of patients started in Feb. 2009 under the supervision of Dr. Herfarth at the Department of Radiooncology and Radiotherapy of the University Clinic of Heidelberg. The study will start out with an MV CBCT-based workflow, i. e. the control CT scans will be acquired using the onboard MV CBCT of the ARTISTE Linac. In parallel, the prospects of the kVue tabletop (see Table 2.1) are being evaluated. If the kVue tabletop becomes available at DKFZ, it is conceivable that the workflow of the study will switch to a kV CT-based one in order to take advantage of the superior image quality of this modality.

Chapter 6

Discussion and conclusions

In this chapter, the achievements of this thesis will be discussed in the context of other works in the field, of clinical applications and of future works.

6.1 Electromagnetic tracking and x-ray imaging

The investigated aspects of the combination of EM tracking and x-ray imaging shall be discussed. These aspects include detectability of transponders in x-ray images, concurrency of imaging and EM tracking, transponder-tracking image processing and synchronization. The ARTISTE solution offers an array of imaging options whose capabilities, to date, were investigated systematically in one report by Stützel et al. [24]. At the same time, the detectability of the Calypso transponders in MV x-ray images remained an open question: Willoughby et al. [31] reported that detectability was unreliable in MV portal images. The tests performed in the course of this thesis and presented in Section 3.2.1 confirmed this finding. In contrast, detectability in MV CBCT images was surprisingly good (Rose's model values, Eqn. 3.15, of $\nu > 25$). Hence, the conclusion from the phantom experiments is that transponder detectability in MV projection images is poor while it is granted in MV CBCT images. This conclusion may be valid only for the specific set of MV x-ray imaging equipment used and it remains to be seen whether the same conclusion can be drawn when real patients are imaged.

6.1.1 Imaging with concurrent EM tracking

In recent years, x-ray imaging-based organ motion management was at the focus of research particularly since Linac-integrated, so called *onboard* imaging became a clinical reality. The general challenge then is (1) to maximize the information about organ motion, (2) to minimize imaging dose and (3) to minimize the time needed for the procedures. The promise of the combination of EM target tracking with x-ray imaging is that it offers unique opportunities for meeting these three challenges. In the following, first, the short-

comings of using each motion measurement separately (EM or imaging) will be reviewed, subsequently, the results of this thesis will be related to the work of other groups and, finally, future clinical use cases will be discussed.

EM target tracking has been applied in a clinical trial to track the prostate gland during external beam radiotherapy [6, 31]. This study revealed unprecedented insight into intrafractional motion of the prostate. One of the results was that in 15% of a total of 1157 treatment fractions, the prostate exhibited excursions of $> 5\,\mathrm{mm}$ for more than 30 seconds cumulative. The implications of such excursions for rectum, bladder or seminal vesicles were not addressed by this study; presumably because concurrent imaging was then unavailable. On the other hand, solely imaging-based studies of intrafractional prostate motion had other shortcomings such as sparse sampling (both temporal or spatial) of target localizations, time-consuming acquisitions and interpretation of images, reader-dependent target localization, unavailability of the modality during treatment, or additional dose burden to the patient.

To the best of the my knowledge, the current work resulted in one of the first peer-reviewed report—in early 2008, i. e. coincidental with Santanam et al. [44]—demonstrating concurrent EM tracking and imaging. Willoughby et al. [31], in their earlier report, still avoided concurrency in order to prevent interference effects. To date, the work—at DKFZ and by other groups—was mostly focused on the evaluation of the technical feasibility of concurrent operation and the correlation between EM- and image-based target coordinates. Some proof-of-principle applications have also been demonstrated—motion-correlated CBCT in this work or tracking of breathing motion in a canine animal model by Santanam et al. [44]. The near-future goals for the research community should be the introduction of EM target tracking with concurrent imaging in clinical workflows. A few conceivable strategies will be outlined next with a focus on two out of the three challenges involved: motion information and imaging dose.

6.1.1.1 Clinical application scenarios

It is important to realize that wherever x-ray imaging is performed with the sole intent of localizing the treatment target, EM target tracking could simply replace x-ray imaging thus eliminating any imaging dose (assuming that organ deformation and rotation are ignored). But even so, it would probably make sense to image the treatment area at some intervals in order to verify transponder position. One imaging procedures that falls into this category is the tracking of tumor motion by observation of external motion surrogates while using x-ray imaging to construct, verify and update a correlation model between motion of the external surrogate. This strategy has been investigated and established in the context of the Cyberknife and the ExacTrac radiotherapy products. Even more drastic would be the dose savings if EM target tracking was used to replace purely x-

ray-based methods of target tracking typically involving internal gold fiducials. However, here strategies shall be outlined where the combination of EM target tracking and x-ray imaging would be advantageous. From the above, it should be clear that a synergistic benefit can only be obtained if imaging serves a purpose beyond mere target localization.

More motion information – same dose The 4D CBCT acquisition demonstrated in Chapter 4 of this work is one scenario in which, using the same imaging dose, 'more' motion information could be obtained. 'More' refers to the fact that the target motion measurement is direct and 3D as opposed to an indirect and 1D measurement such as spirometry. The synergistic benefit manifests as an improved image quality. Another scenario that falls into this category is the reconstruction of the cumulative delivered dose—a prerequisite of adaptive radiotherapy [83]. To reconstruct the delivered dose it is necessary to know the target position and the state of the Linac (output fluence, MLC aperture) as functions of time. Berbeco et al. [84] propose to obtain the target position from tracking implanted gold fiducials in portals-during and to use the same portals-during for the dosimetric evaluation. Their approach fails to work for IMRT treatments because most of the times obstruction of the fiducials by the MLC leafs will prevent target motion tracking. In this case, EM target tracking provides the solution, which has already been demonstrated by Litzenberg et al. [85]. Compared to the Berbeco-method, their approach makes use of 'more' motion information at no extra dose cost (ignoring ~1% of backscattered radiation from the deployed MV FPI). However, they completely waived portals-during imaging and instead performed a Monte-Carlo based dose calculation and obtained the MLC apertures from Linac log files. Potentially, their approach may still benefit from concurrent portals-during imaging as it provides an independent means of monitoring MLC leaves position, transponder position, Linac dose output and perhaps even contours of a high-contrast tumor masses. A list of potential additional benefits from portals-during imaging can be found in [86].

More motion information – less dose A clinical concept of this category is *on-demand imaging* for IGRT. Assumed ingredients of this concept would be EM target tracking, used for initial patient setup and for tracking of intrafractional target motion, and onboard kV CBCT, used as the imaging modality of choice. A number of strategies to define demand are conceivable. For example, demand could be defined as a remaining rotation of the prostate following patient setup of $> 10°$ about any of the three room axes (the Calypso System can, in principle, be used to compute rotation). Djemil et al. [87] analyzed 1527 fractions and found that this situation occurred in ~12% of the fractions. Compared to a common IGRT scheme with daily pre-treatment CBCTs [88], 88% of imaging dose could be spared while initial target

positioning would still be guaranteed and image data would be available to assess the relevant anatomy (seminal vesicles, rectum, bladder) in the presence of prostate rotation. Another conceivable definition of imaging demand could be spatially and temporally significant excursions of the prostate, e.g. >5mm for more than 30s. Kupelian et al. [6] states that such events occur in 15% of the fractions[1]. It means that 85% of the imaging dose could be spared compared to a daily CBCT scheme[2]. Clearly, in order to capture the image of the excursed prostate, the treatment would have to be paused for an image acquisition. If concurrent EM tracking and imaging was available, the treatment interruption can be managed in an efficient workflow, i.e. radiotherapists need not enter the treatment room. Apart from workflow reasons, CBCT imaging benefits from the intra-imaging motion-detection capability of concurrent EM target tracking—feasibility demonstrated in Chapter 4. Dose sparing and workflow efficiency may be further improved if instead of acquisition of a full CBCT, only a few projections would be acquired at the times of pronounced prostate motion. It should be possible to register bony anatomy on these radiographs and thus to determine whether prostate motion was caused by motion of the entire patient or of the internal anatomy. With colorectal administration of barium-based contrast agents the rectum may even be visualized in those radiographs, thus enabling the verification of rectal wall position. In summary, these concepts aim at restricting x-ray imaging to instants of some clinical meaning rather than pre-determined imaging schemes based on chance, ultimately. This idea in combination with the methods developed for concurrency of EM tracking and imaging would (i) result in more relevant image data, (ii) save non-conformal imaging dose to the patient and reduce overall treatment duration (by virtue of performing fewer imaging sessions).

6.1.1.2 Future works

Future works can be envisioned in the technical and in the clinical field. Technically, the combination of EM target tracking with helical fan-beam CT imaging is intriguing, especially at DKFZ where a CT-on-rails in available in the treatment room. If feasible, patient motion during control CT acquisition and during patient transit (from the treatment position to the CT-on-rails position) can be assessed. The challenges include the blockage of the line of sight for the Calypso cameras by the CT ring gantry and interference effects due to the proximity of EM magnetic array and CT imaging components.

---

[1]Kupelian et al. [6] counted excursions that lasted longer than 30s cumulative. For the derivation of an imaging demand, excursions of >30s consecutive are more suitable. These should occur at a lower frequency than temporally cumulative excursions.

[2]The dose to a central point in the patient is approx. 1–2 cGy in kV CBCT [89] and approx. 10–20 cGy in MV CBCT [90].

Clinically, the way for x-ray imaging with concurrent EM target tracking leads from the testing of workflows using dynamic phantoms to board-approved clinical feasibility studies. A competing group at Washington University in St. Louis additionally makes use of animal studies [44, 61]. Our group at DKFZ, is in a good position to contribute to the field: a 4D programmable phantom is being acquired and onboard kV imaging has recently (Feb. 2009) been re-installed on one of the ARTISTE Linacs.

6.1.2 Transponder-tracking image processing

Automated seed localization forms the basis of most imaging-based intrafraction motion monitoring and management. Usually, gold seeds (spheres, rods or coils) are implanted in or near a tumor and an image processing algorithm is applied to fluoroscopy images of the tumor-containing anatomy in order to localize these seeds. In Chapter 3 of the present work, a transponder-tracking image processing algorithm (TTA), tailored to the localization of EM transponders, was presented. The main difference between the transponders and gold seeds is a decrease of x-ray contrast of approximately a third. Low seed contrast can lead to frequent false-positive detections—"spurious components" in Chapter 3. In order to handle low seed contrast, iterative thresholding and moments-based component analysis were implemented (cf. Figure 3.1). The TTA should be fit to adjust to a range of image qualities—as they may be encountered with real-patient images—because it provides a configurable algorithmic framework. For example, the structuring element used in the top-hat filter or the parameters used for shape description (cf. Table 3.1) can be adjusted to optimize the TTA's behavior.

The automatic localization of the transponders in x-ray images will be necessary (1) if results need to be available instantaneously or (2) if large numbers of images need to be processed. The former could be, e. g., a quick intrafractional verification of the transponder position without interrupting the treatment; the latter applies to the post-processing of the frames of a fluoroscopic sequence of breathing motion for treatment simulation. A few clinical use cases of the TTA have also been elaborated in the motivation of the method on page 37.

6.1.2.1 Future works

Future work could aim at making the TTA more robust and more universal. Currently, the TTA would get confused if small metallic objects, i e. of similar radiographic appearance as transponders, were present in the ROI. On the one hand, it should be able to avoid this situation with real patient. On the other hand, it may be desirable to stick steel BBs to the patient's skin for some procedures. The latter would create a challenging situation for the TTA. The robustness of the TTA could be improved if the triangular configura-

tion of the three transponders was considered by the TTA. In the simplest case, the TTA could perform a plausibility check to make sure the transponder locations approximately adhere to the triangular configuration expected at a given viewing angle.

Figure 6.1: *Fluoroscopic frame showing the lesion of the thorax phantom in an AP projection taken through the treatment table and through the magnetic array of the Calypso System. The wires of the magnetic array are visible. These challenge automatic transponder localization using the TTA.*
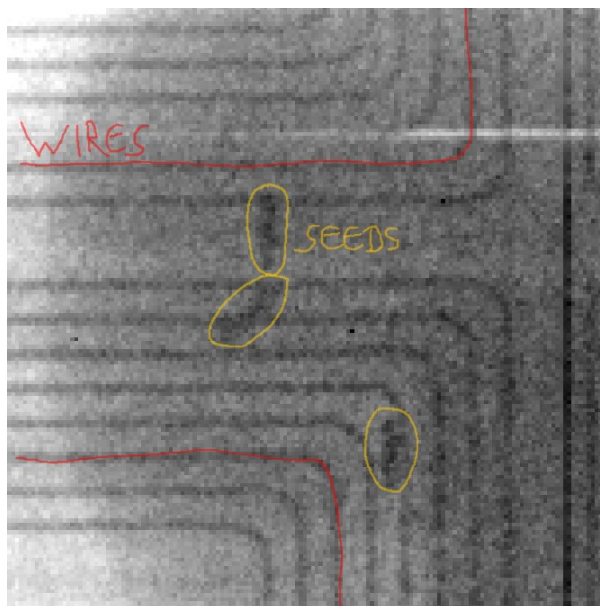
Universality of the TTA should be increased towards the handling of transponder detection through the magnetic array of the Calypso System. Figure 6.1 shows the appearance of the wires of the source coils of the magnetic array in a fluoroscopic frame. The transponders are also visible in this frame. The wires superimpose structured noise onto the x-ray image that challenges transponder localization using the TTA. Removal of the wires from the images by simple subtraction of a template image is possible, in principle, but not practical because the magnetic array would always have to be in the exact same position as in the template image. Perhaps a more involved template-subtraction approach can be successful if preceded by a cross-correlation-based registration of the template to the current frame. Finally, testing of the TTA against real-patient images remains an important component of future works.

6.1.3 Synchronization

The synchronization emerged as a topic of this thesis when the image artifacts of the sort shown in Figure 3.6 became apparent. As described previously, one study [31] also mentioned interference effects but prevented them by avoiding simultaneous systems operation while others [44], in turn, apparently were not affected by EM interference. It is possible, that changes to the image reception group of components (FPI, housing, cabling) may, in the future, overcome the need to synchronize image acquisition with EM tracking. However, the synchronization developed in this work achieved an important goal of this

thesis: combined target tracking using the Calypso System and x-ray imaging. Beyond this immediate use of synchronization, it also allowed unification of the separate time axes necessary for the 4D CBCT acquisition (Chapter 4). The unification of time axes also opens up the possibility to evaluate system latencies, necessary for implementing the adaptive treatment in which the EM target position would be used to control a DMLC in near real-time (cf. Section 2.4.4). After this thesis work and the work by Tacke [37], the vision of real-time adaptive radiotherapy can be implemented at DKFZ, as a prototype, and evaluated concerning its potential and limitations.

6.2 4D CBCT

Onboard CBCT imaging has established as one of the pillars of IGRT over the past decade. Time-correlated 4D CBCT is still an active area of research owing to both its potential and its challenges. A number of significant contributions came out of research conducted at the DKFZ: Dietrich et al. [65], Thilmann et al. [91] and Oelfke et al. [5] were among the first worldwide to demonstrate clinical feasibility. Stützel et al. [24] published a comparative study of image quality and Rau et al. [19] presented the work of Chapter 4 of this thesis.

What is the potential of the new method presented in Chapter 4? First, it improves upon existing methods and, second, it opens up new 4D CBCT applications. Existing methods were mostly concerned with the generation of respiratory-correlated CBCT. These methods used surrogate measurements of intra-imaging breathing motion such as (1) the ANZAI pressure belt [65], (2) diaphragm motion [43] and (3) the motion of a radiopaque marker attached to the patient's skin [92]. The new method in Chapter 4 is based on a motion measurement that measures target motion directly, continuously in 3D and it is independent of the image interpretation, which is in contrast to methods #2 and #3 above. The new method can be expected to represent target motion better than previous methods and to be faster—assuming a real-time data output from the Calypso System becomes available.

A possible new application is the extension of respiratory-correlated CBCT of the thorax to motion-correlated CBCT of the prostate, for example. Here, motion-correlation means that not only periodic breathing motion is considered but motion from any source such as gastro-intestinal organ motion. Létourneau et al. [93] have shown how CBCT image quality gets degraded by gastro-intestinal prostate motion occurring during image acquisition. Figure 6.2 illustrates how image quality degradation may be avoided using the CBCT method introduced in Chapter 4. Figure 6.2b sketches a CBCT acquisition of the prostate. In an angular sector of the fullscan image acquisition, EM target tracking detected a prostate excursion. The prostate returned to its stable position after the

(a) respiratory-corr. thorax CBCT **(b)** motion-corr. prostate CBCT
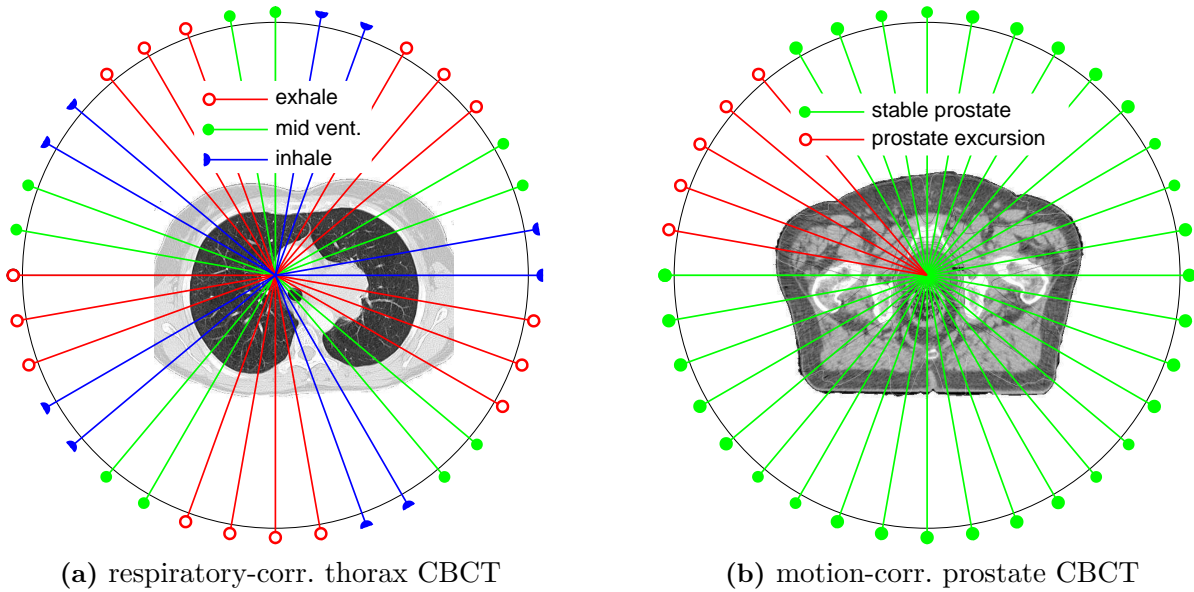
Figure 6.2: *Simplified illustration of fullscan (i. e. 360° gantry rotation) CBCT acquisitions. Projections, indicated by the colored lines, are acquired at 10° intervals. (In reality, the angular sampling would be approx. tenfold.) The conventional scheme of respiratory-correlated CBCT acquisition using three phase bins is shown in (a). A motion-correlated scheme for prostate CBCT is shown in (b): "bad frames" (marked in red with hollow circles) can be excluded from reconstruction.*

excursion. The projections captured during prostate excursion may be excluded from reconstruction thus avoiding image quality degradation due to prostate motion. The 4D CBCT method developed in this work is ideally suited for a new CBCT application such as the one illustrated in Figure 6.2b.

Future works

Future works could focus on improving the image quality attainable from the CT scanner and on exploring concepts for projection sorting based on 3D target motion measurements. It should be possible to improve image quality by incorporating a scatter correction method into the CBCT reconstruction and by acquisition of more projections once a technically mature CBCT scanner is available at DKFZ. Significant research efforts have been put into the reduction of the streaking artifacts (sometimes called *view-aliasing*) caused by the uneven, clustered angular sampling and the limited number of projections available post-sorting for reconstruction (see Figure 6.2a). These efforts included reducing gantry rotation speed or letting the gantry rotate twice: once clockwise and once counter-clockwise [68]. However, recently this research is heading towards the incorporation of motion-corrections, based on *a priori* motion models, into the reconstruction

algorithms [94, 95]. The intriguing advantage of these methods is that *all* projections can be used to reconstruct a motion-corrected 3D dataset without the need to work on projection subsets. It should be subject to future works to evaluate the potential of the CBCT method developed in this work towards motion-corrected CBCT reconstruction.
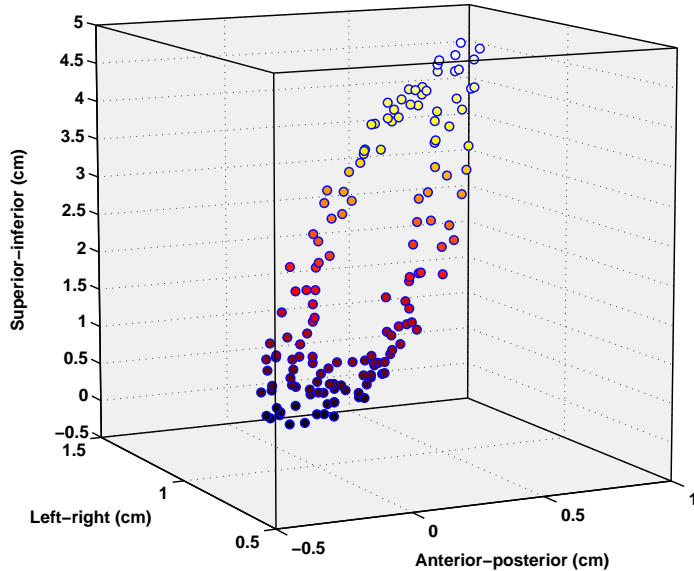
Figure 6.3: *Simulated 3D trace of a lung lesion during free breathing [30]. High-amplitude motion is visible in the superior-inferior (or cranial-caudal→CC) direction. Hysteresis occurs in the anterior-posterior direction. The datapoints are color-coded based on their superior-inferior (CC) position. A $\cos^4$-type motion was assumed in CC direction with the exhale position towards the bottom of the graph (inferiorly).*

The other interesting question is how to best sort the projections if target motion measurements are available in 3D—unlike the 1D motion measures provided by spirometry or the ANZAI pressure belt. Figure 6.3 shows the simulated trace of a lung lesion representing very high-amplitude motion according to the results of Seppenwoolde et al. [30]. In the conceptual work of Chapter 4 only the principal direction of target motion was used as the basis for projection sorting. This simplification would correspond to sorting the projections of the motion shown in Figure 6.3 based on the color codes of the data points. Obviously, other sorting strategies are conceivable. For example, during the mid ventilation phase, the target is in one of two states corresponding to exhalation and inhalation. Hence, separate exhalation and inhalation images could be reconstructed, in principle. Also, arbitrary sub-volumes could be defined and the projections falling into these sub-volumes could be used for reconstruction. Strategies for projection sorting based on 3D motion data should be investigated in the future using a programmable 4D motion phantom (soon to be available at DKFZ) and patient data resulting from the clinical prostate trial that is underway.

6.3 Clinical trial

Chapter 5 described how the first European patient study using EM transponders for intrafraction motion tracking was designed and launched. Very recently, Kindblom et al. [15] published some first experience with the Micropos EM tracking system. However, this was a feasibility study based on ten prostate patients. Prostate motion was only tracked in one extra-fractional session per patient, i. e. no systematic intrafractional prostate motion was measured. The data coming out of the DKFZ clinical trial should provide a rich resource for research towards improving radiotherapy for prostate carcinoma patients. Planning studies can be performed to research optimal planning strategies given the prostate motion data of the study. Schemes for adaptive radiotherapy, i. e. re-planning of a patient after some fractions—or even after each fraction—in consideration of the cumulative dose delivered up to this point, may result from this research. In addition, the motion data should provide the basis for the evaluation of the optimal use of a DMLC for prostate cancer treatment.

Chapter 7

Summary

The use of EM-based target volume tracking in modern radiotherapy was investigated. First, an array of experiments was conducted in order to gain experience of the interaction of the EM target tracking technology with the radiotherapy environment (Chapter 2). It was found that the rotation of the Linac gantry can disturb the EM-based target coordinates in a minor way (up to 0.5 mm error) and thus the effect was deemed negligible. Extensive testing of the treatment tables was performed with the result that the established tabletop at the DKFZ needed to be replaced in order to ensure accurate target localization by the EM target tracking system. In another experiment, the influence of the antenna (referred to as "magnetic array" in the text) of the EM tracking system, which is traversed by some x-ray treatment beams, on the dose distributions was evaluated. Comparisons of dose distributions obtained with the antenna in place to dose distributions with the antenna removed yielded discrepancies of less than 1%. The effect is negligible because it falls within the 3% tolerance applied at the DKFZ. Finally, the proof-of-principle of the control of a DMLC based on the real-time stream of target positions measured by the EM tracking system was demonstrated.

In Chapter 3, EM-based target tracking was integrated with onboard x-ray imaging. This integration provided a novel method for the tracking of intrafractional motion in radiotherapy. First, the detectability of the EM Beacon transponders in MV x-ray images was investigated: the transponder detectability in 2D MV x-ray projection images was very poor, but it was warranted in 3D MV CBCT image data. The latter was a prerequisite for the MV CBCT-based clinical workflow designed in Chapter 5. Severe artifacts in the x-ray images where observed caused by the EM tracking system. The artifact problem was resolved by the development of an electronic interface used to synchronize image acquisition with EM tracking. Finally, the new dual-modality method of target volume tracking could be demonstrated using a breathing thorax phantom. Submillimeter tracking accuracy could be attested to both the EM- and the image-based tracking modality when tracking physiological motion up to target velocities of 3 cm/s. For both modalities, the tracking accuracy decreased slightly (up to 0.25 mm of error)

with increasing velocities of motion.

The ability to image a moving target while concurrently tracking its 3D position using EM technology (developed in Chapter 3) was applied to enhance the generation of motion-correlated 4D CBCT data in Chapter 4. With this enhancement, it becomes possible to counter not only the detrimental effects of respiratory motion on image quality but also motion from sources other than breathing, e. g. intestinal motion or spontaneous whole-patient motion. Chapter 5 finally reported on the design and the launch of a clinical prostate trial at the DKFZ using the EM technology. Study workflows were developed and a new patient treatment tabletop was introduced into the clinic.

This thesis has introduced EM-based target volume tracking to the radiotherapy environment at the DKFZ and it has identified and implemented methods of EM-based target volume tracking in combination with Linac-integrated x-ray imaging that augment the possibilities of IGRT.

Bibliography

[1] Marcel van Herk. Errors and margins in radiotherapy. *Semin Radiat Oncol*, 14(1): 52–64, Jan 2004.

[2] Daniel Létourneau, John W Wong, Mark Oldham, Misbah Gulam, Lindsay Watt, David A Jaffray, Jeffrey H Siewerdsen, and Alvaro A Martinez. Cone-beam-CT guided radiation therapy: Technical implementation. *Radiother Oncol*, 75(3):279–286, Jun 2005.

[3] David A Jaffray. Emergent technologies for 3-dimensional image-guided radiation delivery. *Semin Radiat Oncol*, 15(3):208–216, Jul 2005.

[4] Lei Xing, Brian Thorndyke, Eduard Schreibmann, Yong Yang, Tian-Fang Li, Gwe-Ya Kim, Gary Luxton, and Albert Koong. Overview of image-guided radiation therapy. *Med Dosim*, 31(2):91–112, 2006.

[5] Uwe Oelfke, Thomas Tücking, Simeon Nill, Annete Seeber, Bernd Hesse, Peter Huber, and Christoph Thilmann. Linac-integrated kV-cone beam CT: technical features and first applications. *Med Dosim*, 31(1):62–70, 2006.

[6] Patrick Kupelian, Twyla Willoughby, Arul Mahadevan, Toufik Djemil, Geoffrey Weinstein, Shirish Jani, Charles Enke, Timothy Solberg, Nicholas Flores, David Liu, David Beyer, and Lisa Levine. Multi-institutional clinical experience with the Calypso System in localization and continuous, real-time monitoring of the prostate gland during external radiotherapy. *Int J Radiat Oncol Biol Phys*, 67(4):1088–1098, Dec 2007.

[7] Hiroki Shirato, Keishiro Suzuki, Gregory C Sharp, Katsuhisa Fujita, Rikiya Onimaru, Masaharu Fujino, Norio Kato, Yasuhiro Osaka, Rumiko Kinoshita, Hiroshi Taguchi, Shunsuke Onodera, and Kazuo Miyasaka. Speed and amplitude of lung tumor motion precisely detected in four-dimensional setup and in real-time tumor-tracking radiotherapy. *Int J Radiat Oncol Biol Phys*, 64(4):1229–1236, Mar 2006.

[8] Trine Juhler Nøttrup, Stine Sofia Korreman, Anders Navrsted Pedersen, Lasse Rye Aarup, Håkan Nyström, Mikael Olsen, and Lena Specht. Intra- and interfraction

breathing variations during curative radiotherapy for lung cancer. *Radiother Oncol*, 84(1):40–48, Jul 2007.

[9] George T Y Chen, Jong H Kung, and Kevin P Beaudette. Artifacts in computed tomography scanning of moving objects. *Semin Radiat Oncol*, 14(1):19–26, Jan 2004.

[10] Thomas Bortfeld, Steve B Jiang, and Eike Rietzel. Effects of motion on the total dose distribution. *Semin Radiat Oncol*, 14(1):41–51, Jan 2004.

[11] J. G. Li and L. Xing. Inverse planning incorporating organ motion. *Med Phys*, 27 (7):1573–1578, Jul 2000.

[12] Paul Keall. 4-Dimensional computed tomography imaging and treatment planning. *Semin. Radiat. Oncol.*, 14(1):81–90, Jan 2004.

[13] J. Unkelbach and U. Oelfke. Incorporating organ movements in inverse planning: assessing dose uncertainties by Bayesian inference. *Phys Med Biol*, 50(1):121–139, Jan 2005.

[14] P. G. Seiler, H. Blattmann, S. Kirsch, R. K. Muench, and C. Schilling. A novel tracking technique for the continuous precise measurement of tumour positions in conformal radiotherapy. *Phys Med Biol*, 45(9):N103–N110, Sep 2000.

[15] Jon Kindblom, Ann-Marie Ekelund-Olvenmark, Hanna Syren, Roman Iustin, Karin Braide, Ingela Frank-Lissbrant, and Bo Lennernäs. High precision transponder localization using a novel electromagnetic positioning system in patients with localized prostate cancer. *Radiother Oncol*, in press, Oct 2008.

[16] Andreas W Rau and Uwe Oelfke. Ein schneller Algorithmus zur Lokalisation von Beacons in fluoroskopischen Videosequenzen. In L. Bogner and B. Dobler, editors, *Tagungsband der 37. Jahrestagung der Deutschen Gesellschaft für Medizinische Physik e.V.*, pages 289–291, September 2006.

[17] A. W. Rau, S. Nill, and U. Oelfke. Simultaneous, synchronized tumor tracking with electromagnetic transponders and kV x-ray imaging. In J. Overgaard, editor, *Radiotherapy and Oncology*, volume 84 of *9th Biennial ESTRO Meeting on physics and radiation technology for clinical radiotherapy*, pages S61–S62. Elsevier Science, September 2007. Supplement 1.

[18] Andreas W. Rau, Simeon Nill, and Uwe Oelfke. Guided IMRT of lung tumors: monitoring breathing patterns with imaging and electromagnetic transponders during radiation therapy. In Jean-Piere Bissonnette, editor, *Proceedings of the XVTH*

INTERNATIONAL CONFERENCE ON THE USE OF COMPUTERS IN RADIATION THERAPY, volume 2, pages 170–174, June 2007.

[19] A. W. Rau, S. Nill, R. S. Eidens, and U. Oelfke. Synchronized tumour tracking with electromagnetic transponders and kv x-ray imaging: evaluation based on a thorax phantom. *Phys Med Biol*, 53(14):3789–3805, Jul 2008.

[20] James M Balter, J. Nelson Wright, Laurence J Newell, Barry Friemel, Steven Dimmer, Yuki Cheng, John Wong, Edward Vertatschitsch, and Timothy P Mate. Accuracy of a wireless localization system for radiotherapy. *Int J Radiat Oncol Biol Phys*, 61(3):933–937, Mar 2005.

[21] Martin B Tacke, Simeon Nill, Peter Häring, and Uwe Oelfke. 6 MV dosimetric characterization of the 160 MLC, the new siemens multileaf collimator. *Med Phys*, 35(5):1634–1642, May 2008.

[22] Olivier Morin, Amy Gillis, Josephine Chen, Michèle Aubin, M. Kara Bucci, Mack Roach, and Jean Pouliot. Megavoltage cone-beam CT: system description and clinical applications. *Med Dosim*, 31(1):51–61, 2006.

[23] Thomas Tücking. *Development and Realization of the IGRT Inline Concept.* PhD thesis, Ruperto-Carola University of Heidelberg, Jan 2007.

[24] Julia Stützel, Uwe Oelfke, and Simeon Nill. A quantitative image quality comparison of four different image guided radiotherapy devices. *Radiat Oncol*, 86:20–24, 2008.

[25] L. A. Feldkamp, L. C. Davis, and J. W. Kress. Practical cone-beam algortihm. *J. Opt. Soc. Am. A-Opt. Image Sci. Vis.*, 1(6):612–619, 1984.

[26] David A Jaffray, Jeffrey H Siewerdsen, John W Wong, and Alvaro A Martinez. Flat-panel cone-beam computed tomography for image-guided radiation therapy. *Int J Radiat Oncol Biol Phys*, 53(5):1337–1349, Aug 2002.

[27] Horst W Hamacher. Uni Kaiserslautern, Fachbereich Mathematik, AG Optimierung. `http://optimierung.mathematik.uni-kl.de/research/index.html`, 2009.

[28] W. Schlegel, O. Pastyr, T. Bortfeld, G. Becker, L. Schad, G. Gademann, and W. J. Lorenz. Computer systems and mechanical tools for stereotactically guided conformation therapy with linear accelerators. *Int J Radiat Oncol Biol Phys*, 24(4): 781–787, 1992.

[29] Lars Dietrich. *Berücksichtigung von inter- und intrafraktionellen Organbewegungen in der adaptiven Strahlentherapie.* PhD thesis, University of Heidelberg, 2005.

[30] Yvette Seppenwoolde, Hiroki Shirato, Kei Kitamura, Shinichi Shimizu, Marcel van Herk, Joos V Lebesque, and Kazuo Miyasaka. Precise and real-time measurement of 3D tumor motion in lung due to breathing and heartbeat, measured during radiotherapy. *Int J Radiat Oncol Biol Phys*, 53(4):822–834, Jul 2002.

[31] Twyla R Willoughby, Patrick A Kupelian, Jean Pouliot, Katsuto Shinohara, Michelle Aubin, Mack Roach, Lisa L Skrumeda, James M Balter, Dale W Litzenberg, Scott W Hadley, John T Wei, and Howard M Sandler. Target localization and real-time tracking using the Calypso 4D Localization System in patients with localized prostate cancer. *Int J Radiat Oncol Biol Phys*, 65(2):528–534, Jun 2006.

[32] H. Shirato, S. Shimizu, T. Kunieda, K. Kitamura, M. van Herk, K. Kagei, T. Nishioka, S. Hashimoto, K. Fujita, H. Aoyama, K. Tsuchiya, K. Kudo, and K. Miyasaka. Physical aspects of a real-time tumor-tracking system for gated radiotherapy. *Int J Radiat Oncol Biol Phys*, 48(4):1187–1195, Nov 2000.

[33] Lars Dietrich, Thomas Tücking, Simeon Nill, and Uwe Oelfke. Compensation for respiratory motion by gated radiotherapy: an experimental study. *Phys Med Biol*, 50(10):2405–2414, May 2005.

[34] D. McQuaid and S. Webb. IMRT delivery to a moving target by dynamic MLC tracking: delivery for targets moving in two dimensions in the beam's eye view. *Phys Med Biol*, 51(19):4819–4839, Oct 2006.

[35] Martin Tacke, Simeon Nill, and Uwe Oelfke. Real-time tracking of tumor motions and deformations along the leaf travel direction with the aid of a synchronized dynamic MLC leaf sequencer. *Phys Med Biol*, 52(22):N505–N512, Nov 2007.

[36] Amit Sawant, Raghu Venkat, Vikram Srivastava, David Carlson, Sergey Povzner, Herb Cattell, and Paul Keall. Management of three-dimensional intrafraction motion through real-time DMLC tracking. *Med Phys*, 35(5):2050–2061, May 2008.

[37] Martin Tacke. *Adaptation of High-Precision Radiotherapy to Moving Target Volumes in Real-Time Using Dynamic Multileaf Collimators*. PhD thesis, University of Heidelberg, 2009.

[38] Jan J W Lagendijk, Bas W Raaymakers, Alexander J E Raaijmakers, Johan Overweg, Kevin J Brown, Ellen M Kerkhof, Richard W van der Put, Björn Hårdemark, Marco van Vulpen, and Uulke A van der Heide. MRI/linac integration. *Radiother Oncol*, 86(1):25–29, Jan 2008.

[39] Emma J Harris, Helen A McNair, and Phillip M Evans. Feasibility of fully automated detection of fiducial markers implanted into the prostate using electronic portal imaging: a comparison of methods. *Int. J. Radiat. Oncol. Biol. Phys.*, 66(4):1263–1270, Nov 2006.

[40] G. Lechsel and R. Bendl. Fast interactive segmentation of organs at risk with active contours. *Radiotherapy and Oncology*, 76(Supplement 2):S131–S131, 2005.

[41] A. Yezzi, L. Zöllei, and T. Kapur. A variational framework for integrating segmentation and registration through active contours. *Med Image Anal*, 7(2):171–185, Jun 2003.

[42] Silke Ulrich, Simeon Nill, and Uwe Oelfke. Development of an optimization concept for arc-modulated cone beam therapy. *Phys Med Biol*, 52(14):4099–4119, Jul 2007.

[43] Jan-Jakob Sonke, Lambert Zijp, Peter Remeijer, and Marcel van Herk. Respiratory correlated cone beam CT. *Med Phys*, 32(4):1176–1186, Apr 2005.

[44] Lakshmi Santanam, Kathleen Malinowski, James Hubenshmidt, Steve Dimmer, Martin L Mayse, Jeffrey Bradley, Amir Chaudhari, Kirsten Lechleiter, Sree Krishna Murty Goddu, Jacqueline Esthappan, Sasa Mutic, Daniel A Low, and Parag Parikh. Fiducial-based translational localization accuracy of electromagnetic tracking system and on-board kilovoltage imaging system. *Int J Radiat Oncol Biol Phys*, 70(3):892–899, Mar 2008.

[45] A. Nederveen, J. Lagendijk, and P. Hofman. Detection of fiducial gold markers for automatic on-line megavoltage position verification using a marker extraction kernel (MEK). *Int J Radiat Oncol Biol Phys*, 47(5):1435–1442, Jul 2000.

[46] D. Tubic, A. Zaccarin, J. Pouliot, and L. Beaulieu. Automated seed detection and three-dimensional reconstruction. I. Seed localization from fluoroscopic images or radiographs. *Med Phys*, 28(11):2265–2271, Nov 2001.

[47] S. Aubin, L. Beaulieu, S. Pouliot, J. Pouliot, R. Roy, L. M. Girouard, N. Martel-Brisson, E. Vigneault, and J. Laverdière. Robustness and precision of an automatic marker detection algorithm for online prostate daily targeting using a standard V-EPID. *Med Phys*, 30(7):1825–1832, Jul 2003.

[48] Annette Seeber. Development and validation of a cone-beam computed tomography reconstruction for adaptive radiation therapy of extracranial regions. Diploma thesis, Universität Karlsruhe, July 2005.

[49] Matthias Ebert. *Non-ideal projection data in X-ray computed tomography.* PhD thesis, University of Mannheim, 2001.

[50] Manfred Kopp and Werner Purgathofer. Efficient 3x3 median filter computations. *Machine Graphics & Vision*, 4(1/2):79–82, 1995.

[51] Rafael C. Gonzalez and Richard E. Woods. *Digital Image Processing (2nd Edition).* Prentice Hall, January 2002.

[52] Marcel van Herk. A fast algorithm for local minimum and maximum filters on rectangular and octagonal kernels. *Pattern Recogn Lett*, 13(7):517–521, July 1992.

[53] William K. Pratt. *Digital Image Processing: PIKS Inside, 3rd Edition.* Wiley-Interscience, July 2001.

[54] Dan S. Bloomberg. Leptonica—a pedagogically-oriented open source site containing software that is broadly useful for image processing and image analysis applications. `http://www.leptonica.com/`, 2009.

[55] Richard J Prokop and Anthony P Reeves. A survey of moment-based techniques for unoccluded object representation and recognition. *CVGIP: Graphical Models and Image Processing*, 54(5):438–460, 1992.

[56] Luren Yang and Fritz Albregtsen. Fast and exact computation of Cartesian geometric moments using discrete Green's theorem. *Pattern Recogn*, 29(7):1061–1073, 1996.

[57] John A. Rowlands and John Yorkston. *Handbook of Medical Imaging*, volume 1 of *Physics and Psychophysics*, chapter 4, pages 223–328. SPIE Press, Bellingham, WA, 2000.

[58] Albert Rose. The sensitivity performance of the human eye on an absolute scale. *Journal of the Optical Society of America (1917-1983)*, 38:196–+, feb 1948. Provided by the SAO/NASA Astrophysics Data System.

[59] A. E. Burgess. The Rose model, revisited. *J Opt Soc Am A Opt Image Sci Vis*, 16 (3):633–646, Mar 1999.

[60] Hiroki Shirato, Toshiyuki Harada, Tooru Harabayashi, Kazutoshi Hida, Hideho Endo, Kei Kitamura, Rikiya Onimaru, Koichi Yamazaki, Nobuaki Kurauchi, Tadashi Shimizu, Nobuo Shinohara, Michiaki Matsushita, Hirotoshi Dosaka-Akita, and Kazuo Miyasaka. Feasibility of insertion/implantation of 2.0-mm-diameter gold internal fiducial markers for precise setup and real-time tumor tracking in radiotherapy. *Int J Radiat Oncol Biol Phys*, 56(1):240–247, May 2003.

[61] Martin L Mayse, Parag J Parikh, Kristen M Lechleiter, Steven Dimmer, Mia Park, Amir Chaudhari, Michael Talcott, Daniel A Low, and Jeffrey D Bradley. Bronchoscopic implantation of a novel wireless electromagnetic transponder in the canine lung: a feasibility study. *Int J Radiat Oncol Biol Phys*, 72(1):93–98, Sep 2008.

[62] Thomas S. Huang, George J. Yang, and Gregory Y. Tang. A fast two-dimensional median filtering algorithm. *IEEE Transactions on Acoustics, Speech and Signal processing*, assp-27:13–18, 1979.

[63] Martin J Murphy, Richard Eidens, Edward Vertatschitsch, and J. Nelson Wright. The effect of transponder motion on the accuracy of the calypso electromagnetic localization system. *Int J Radiat Oncol Biol Phys*, 72(1):295–299, Sep 2008.

[64] S. S. Vedam, P. J. Keall, V. R. Kini, H. Mostafavi, H. P. Shukla, and R. Mohan. Acquiring a four-dimensional computed tomography dataset using an external respiratory signal. *Phys Med Biol*, 48(1):45–62, Jan 2003.

[65] Lars Dietrich, Siri Jetter, Thomas Tücking, Simeon Nill, and Uwe Oelfke. Linac-integrated 4D cone beam CT: first experimental results. *Phys Med Biol*, 51(11): 2939–2952, Jun 2006.

[66] Jun Lu, Thomas M Guerrero, Peter Munro, Andrew Jeung, Pai-Chun M Chi, Peter Balter, X. Ronald Zhu, Radhe Mohan, and Tinsu Pan. Four-dimensional cone beam ct with adaptive gantry rotation and adaptive data sampling. *Med Phys*, 34(9): 3520–3529, Sep 2007.

[67] Daniel A Low, Michelle Nystrom, Eugene Kalinin, Parag Parikh, James F Dempsey, Jeffrey D Bradley, Sasa Mutic, Sasha H Wahab, Tareque Islam, Gary Christensen, David G Politte, and Bruce R Whiting. A method for the reconstruction of four-dimensional synchronized CT scans acquired during free breathing. *Med Phys*, 30 (6):1254–1263, Jun 2003.

[68] Tianfang Li and Lei Xing. Optimizing 4D cone-beam CT acquisition protocol for external beam radiotherapy. *Int. J. Radiat. Oncol. Biol. Phys.*, 67(4):1211–1219, Mar 2007.

[69] Yelin Suh, Sonja Dieterich, Byungchul Cho, and Paul J Keall. An analysis of thoracic and abdominal tumour motion for stereotactic body radiotherapy patients. *Phys Med Biol*, 53(13):3623–3640, Jul 2008.

[70] Wei Lu, Parag J Parikh, James P Hubenschmidt, Jeffrey D Bradley, and Daniel A Low. A comparison between amplitude sorting and phase-angle sorting using external respiratory measurement for 4D CT. *Med Phys*, 33(8):2964–2974, Aug 2006.

[71] J. H. Siewerdsen and D. A. Jaffray. Cone-beam computed tomography with a flat-panel imager: magnitude and effects of x-ray scatter. *Med Phys*, 28(2):220–231, Feb 2001.

[72] J. H. Siewerdsen, M. J. Daly, B. Bakhtiar, D. J. Moseley, S. Richard, H. Keller, and D. A. Jaffray. A simple, direct method for x-ray scatter estimation and correction in digital radiography and cone-beam CT. *Med Phys*, 33(1):187–197, Jan 2006.

[73] Yongbin Zhang, Lifei Zhang, X. Ronald Zhu, Andrew K Lee, Mark Chambers, and Lei Dong. Reducing metal artifacts in cone-beam CT images by preprocessing projection data. *Int J Radiat Oncol Biol Phys*, 67(3):924–932, Mar 2007.

[74] B. A. Groh, J. H. Siewerdsen, D. G. Drake, J. W. Wong, and D. A. Jaffray. A performance comparison of flat-panel imager-based MV and kV cone-beam CT. *Med Phys*, 29(6):967–975, Jun 2002.

[75] Katja M Langen, Twyla R Willoughby, Sanford L Meeks, Anand Santhanam, Alexis Cunningham, Lisa Levine, and Patrick A Kupelian. Observations on real-time prostate gland motion using electromagnetic tracking. *Int J Radiat Oncol Biol Phys*, 71(4):1084–1090, Jul 2008.

[76] Camille Noel, Parag J Parikh, Meghana Roy, Patrick Kupelian, Arul Mahadevan, Geoffrey Weinstein, Charles Enke, Nicholas Flores, David Beyer, and Lisa Levine. Prediction of intrafraction prostate motion: Accuracy of pre- and post-treatment imaging and intermittent imaging. *Int. J. Radiat. Oncol. Biol. Phys.*, Aug 2008. in press.

[77] Dale W Litzenberg, James M Balter, Scott W Hadley, Howard M Sandler, Twyla R Willoughby, Patrick A Kupelian, and Lisa Levine. Influence of intrafraction motion on margins for prostate radiotherapy. *Int J Radiat Oncol Biol Phys*, 65(2):548–553, Jun 2006.

[78] Haisen S Li, Indrin J Chetty, Charles A Enke, Ryan D Foster, Twyla R Willoughby, Patrick A Kupellian, and Timothy D Solberg. Dosimetric consequences of intrafraction prostate motion. *Int J Radiat Oncol Biol Phys*, 71(3):801–812, Jul 2008.

[79] Michel J Ghilezan, David A Jaffray, Jeffrey H Siewerdsen, Marcel van Herk, Anil Shetty, Michael B Sharpe, Syed Zafar Jafri, Frank A Vicini, Richard C Matter, Donald S Brabbins, and Alvaro A Martinez. Prostate gland motion assessed with cine-magnetic resonance imaging (cine-MRI). *Int J Radiat Oncol Biol Phys*, 62(2):406–417, Jun 2005.

[80] R. Bendl et al. VIRTUOS – A program for VIRTUal radiOtherapy Simulation and verification. In *Proceedings of the XITH INTERNATIONAL CONFERENCE ON THE USE OF COMPUTERS IN RADIATION THERAPY*, 1994.

[81] P. C. Shrimpton, B. F. Wall, and E. S. Fisher. The tissue-equivalence of the alderson rando anthropomorphic phantom for x-rays of diagnostic qualities. *Phys Med Biol*, 26(1):133–139, Jan 1981.

[82] Wolfgang Schlegel, Andreas Mahr, et al. 3D Conformal Radiation Therapy—A multimedia introduction to methods and techniques. DVD—ISBN: 978-3-540-71550-4, 2007. 2nd revised and enhanced edition.

[83] S. Webb and T. Bortfeld. A new way of adapting IMRT delivery fraction-by-fraction to cater for variable intrafraction motion. *Phys Med Biol*, 53(18):5177–5191, Sep 2008.

[84] Ross I Berbeco, Fred Hacker, Chris Zatwarnicki, Sang-June Park, Dan Ionascu, Desmond O'Farrell, and Harvey J Mamon. A novel method for estimating SBRT delivered dose with beam's-eye-view images. *Med Phys*, 35(7):3225–3231, Jul 2008.

[85] Dale W Litzenberg, Scott W Hadley, Neelam Tyagi, James M Balter, Randall K Ten Haken, and Indrin J Chetty. Synchronized dynamic dose reconstruction. *Med Phys*, 34(1):91–102, Jan 2007.

[86] Wouter van Elmpt, Leah McDermott, Sebastiaan Nijsten, Markus Wendling, Philippe Lambin, and Ben Mijnheer. A literature review of electronic portal imaging for radiotherapy dosimetry. *Radiother Oncol*, 88(3):289–309, Sep 2008.

[87] T. Djemil, A. Mahadevan, P. Kupelian, T. Willoughby, C. Enke, T. Solberg, G. Weinstein, S. Jani, N. Flores, and D. Liu. Prostate rotation measured by electromagnetic tracking system: A multi-center analysis. In *Proceedings of the 48th Annual ASTRO Meeting*, 2006.

[88] Qiuwen Wu, Giovanni Ivaldi, Jian Liang, David Lockman, Di Yan, and Alvaro Martinez. Geometric and dosimetric evaluations of an online image-guidance strategy for 3D-CRT of prostate cancer. *Int J Radiat Oncol Biol Phys*, 64(5):1596–1609, Apr 2006.

[89] Mohammad K Islam, Thomas G Purdie, Bernhard D Norrlinger, Hamideh Alasti, Douglas J Moseley, Michael B Sharpe, Jeffrey H Siewerdsen, and David A Jaffray. Patient dose from kilovoltage cone beam computed tomography imaging in radiation therapy. *Med Phys*, 33(6):1573–1582, Jun 2006.

[90] Olivier Morin, Amy Gillis, Martina Descovich, Josephine Chen, Michèle Aubin, Jean-François Aubry, Hong Chen, Alexander R Gottschalk, Ping Xia, and Jean Pouliot. Patient dose considerations for routine megavoltage cone-beam CT imaging. *Med Phys*, 34(5):1819–1827, May 2007.

[91] Christoph Thilmann, Simeon Nill, Thomas Tücking, Angelika Höss, Bernd Hesse, Lars Dietrich, Rolf Bendl, Bernhard Rhein, Peter Häring, Christian Thieke, Uwe Oelfke, Juergen Debus, and Peter Huber. Correction of patient positioning errors based on in-line cone beam cts: clinical implementation and first experiences. *Radiat Oncol*, 1:16, 2006.

[92] Tianfang Li, Lei Xing, Peter Munro, Christopher McGuinness, Ming Chao, Yong Yang, Bill Loo, and Albert Koong. Four-dimensional cone-beam computed tomography using an on-board imager. *Med Phys*, 33(10):3825–3833, Oct 2006.

[93] Daniel Létourneau, Alvaro A Martinez, David Lockman, Di Yan, Carlos Vargas, Giovanni Ivaldi, and John Wong. Assessment of residual error for online cone-beam CT-guided treatment of prostate cancer patients. *Int J Radiat Oncol Biol Phys*, 62 (4):1239–1246, Jul 2005.

[94] T. Li, E. Schreibmann, Y. Yang, and L. Xing. Motion correction for improved target localization with on-board cone-beam computed tomography. *Phys Med Biol*, 51(2): 253–267, Jan 2006.

[95] Simon Rit, Jochem Wolthaus, Marcel van Herk, and Jan-Jakob Sonke. On-the-fly motion-compensated cone-beam CT using an a priori motion model. *Med Image Comput Comput Assist Interv Int Conf Med Image Comput Comput Assist Interv*, 11(Pt 1):729–736, 2008.

List of Figures

List of Tables

Acknowledgments